Observing dust grain growth and sedimentation in circumstellar discs

Interpretations and predictions of their observable quantities in a multi-wavelength approach

Dissertation
zur Erlangung des Doktorgrades
der Mathematisch-Naturwissenschaftliche Fakultät
der Christian-Albrechts Universität zu Kiel

vorgelegt von
Jürgen Sauter
Kiel, 2011

Referent : Prof. Dr. S. Wolf

Koreferent: Prof. Dr. C. Dullemond

Tag der mündlichen Prüfung : 7. Juli 2011

Zum Druck genehmigt: 7. Juli 2011

gez. Prof. Dr. L. Kipp, Dekan

To my growing family

Abstract

In the present thesis, the observational effects of dust grain growth and sedimentation in circumstellar discs are investigated.

The growth of dust grains from some nanometres in diameter as found in the interstellar medium towards planetesimal bodies some meters in diameter is an important step in the formation of planets. However, this process is currently not entirely understood. Especially, in the literature several ‘barriers’ are discussed that apparently prohibit an effective growth of dust grains. Hence, it is of particular interest to compare theories and observational data in this respect. State-of-the-art radiative transfer techniques allow one to derive observable quantities from theoretical models that allow this comparison.

In this thesis, generic tracers of dust grain growth in spatially high resolution multi-wavelength images are identified for the first time. Further, a possibility to detect a dust trapping mechanism for dust grains by local pressure maxima using the new interferometer, ALMA, is established.

By fitting parametric models to new observations of the disc in the Bok globule CB 26, unexpected features of the system are revealed, such as a large inner void and the possibility to interpret the data without the need for grain growth. In the same way, new observations and their interpretation of IRAS 04302+2247 provide evidence for the first time for radial dependent settling of dust grains in images.

Moreover, in this thesis the applicability of the T Tauri disc paradigm to the high-mass disc candidate IRAS 18151-1208 is demonstrated.

Zusammenfassung

In der vorliegenden Dissertation werden die beobachtbaren Effekte von Staubkornwachstum und -sedimentation in zirkumstellaren Scheiben untersucht.

Das Wachstum von Staubpartikeln in der Größe von einigen Nanometen, wie sie im interstellaren Medium zu finden sind, hin zu Planetesimalen mit einigen Metern Durchmesser ist ein wichtiger Prozess im Zuge der Entstehung von Planeten. Allerdings ist dieses Wachstum gegenwärtig nicht vollständig verstanden. Insbesondere werden in der Fachliteratur einige Schranken diskutiert, die ein effektives Wachstum von Staubkörnern zu verhindern scheinen. Daher ist es von besonderer Bedeutung, Theorien und Beobachtungsdaten in diesem Zusammenhang miteinander zu vergleichen. Strahlungstransportmethoden auf dem aktuellen Stand der Technik gestatten es, aus theoretischen Modellen Beobachtungsgrößen abzuleiten, die einen solchen Vergleich erlauben.

In dieser Arbeit werden zum ersten Mal generische Indikatoren des Staubkornwachstums in räumlich hochaufgelösten Bildern mehrerer Wellenlängen identifziert. Zudem wird eine Möglichkeit aufgezeigt, die es gestattet, mit Hilfe des neuen Interferometers ALMA die Spuren von durch lokale Gasdruckmaxima eingefangenen Staubkörnern zu erkennen.

Durch Bestimmung der Parameter geeigneter Modelle anhand neuer Beobachtungsdaten der Scheibe im Bok-Globulus CB 26 werden neue unerwartete Eigenschaften des Systems, wie ein großer, zentraler staubfreier Bereich und die Möglichkeit, die Beobachtungsdaten ohne die Annahme von Staubkornwachstum zu interpretieren, enthüllt. Ebenso erlauben neue Beobachtungen und deren Deutung von IRAS 04302+2247 zum ersten Mal einen Hinweis in Bildern auf radiusabhängige Sedimentation von Staubkörnern.

Darüberhinaus wird die Anwendbarkeit des Scheibenkonzeptes von T Tauri Sternen auf IRAS 18151-1208, einem massereichen Protostar, gezeigt.

Contents

1. Introduction

> Μετὰ ταῦτα δή, εἶπον, ἀπείκασον τοιούτῳ πάθει τὴν ἡμετέραν φύσιν παιδείας τε πέρι καὶ ἀπαιδευσίας. ἰδὲ γὰρ ἀνθρώπους οἷον ἐν καταγείῳ οἰκήσει σπηλαιώδει, ἀναπεπταμένην πρὸς τοφῶς τὴν εἴσοδον ἐχούσῃ μακρὰν παρὰ πᾶν τὸ σπήλαιον, ἐν ταύτῃ ἐκ παίδων ὄντας ἐν δεσμοῖς καὶ τὰ σκέλη καὶ τοὺς αὐχένας, ὥστε μένειν τε αὐτοὺς εἴς τε τὸ πρόσθεν μόνον ὁρᾶν, κύκλῳ δὲ τὰς κεφαλὰς ὑπὸ τοῦ δεσμοῦ ἀδυνάτους περιάγειν.[1]
>
> (*Platon,* Πολιτεία)

The questions concerning the origin of our very own existence might very well be as old as the ability of humans to pose questions in general. Attempts to answer these deep questions are provided by various enterprises of mankind such as religion, philosophy and also science. While the reasoning of the first two is confined to faith and exchange of (clever) arguments, it is the latter that gains its tremendous success by observing the physical nature as it surrounds us. Theories built on these observations are required to yield predictive power and these predictions are in turn subject to comparison with the physical world.

One might argue that in this fashion rather the question *How?* is answered instead of the question *Why?*. The success of science is driven by its ability to connect subjects previously considered disjoint and to describe them by a common set of terms. In a plenitude of cases this property provides an answer to the first question and renders the necessity to pose the second one moot.

Therefore, the question about our origin eventually leads to the question of the origin of our home, the planet Earth we dwell upon. No other planet is known that harbours life, and until the end of the last decade of the second millennium extra-solar planets in general had not been observed. Any understanding developed up until then on how planets come into existence rested solely on the observed properties of our own solar system.

Five of the solar planets have been observed and studied since several thousand years. Their motion eventually gave rise to the powerful Newtonian Mechanics and

---

[1] A translation of all Chapter headings is given in the appendix B

also provided one impressive confirmation of General Relativity. The non-classical planets have all been discovered in the modern age by virtue of careful application of celestial mechanics. However, as the existence of extrasolar planets became evident, it was also clear that these newly discovered planetary systems differ greatly from the solar system. Previously, it was deemed necessary that small and rocky planets, such as Earth, should be found close to the host star while gaseous planets have been expected at larger radii. Nonetheless, among the first discovered extra-solar planets were 'hot Jupiters': gaseous orbs at small distances to their star. Consequently, the established understanding of the formation of planetary systems needed serious revision. A fully consistent theory is still lacking.

Circumstellar discs are understood to be the nursery of planets, providing both material and dynamic environment for their birth. The most accepted evolutionary theory for planets in discs is the so-called "core-accretion gas-capture" scenario, featuring a build-up of planet cores first and gas-infall on sufficiently massive cores later (Adams *et al.*, 1987; Lissauer, 1993; Klahr & Brandner, 2006; Williams & Cieza, 2011). In the evolution of T Tauri stars, circumstellar discs are the natural precursor of a planetary system. Key issues in the process of planetary core formation are dust grain growth and settling, which start the formation process of planetesimals (e.g. Youdin & Shu, 2002).

A characteristic that is sometimes used to single out astronomy from other disciplines of physics is its inability to conduct 'hands-on' experiments. One cannot set up a protoplanetary disc in the laboratory and study its fate (much less galaxies or clusters thereof). In two particular senses this has changed, however. Today's experiments are carried out to study the coagulation, bouncing and fragmentation properties of dust grains that are expected to form planetesimals. And even more so, numerical experiments relying on considerable computing power have become state of the art. Sundry models respecting different assumptions and mechanisms thus can be examined.

Different evolution models provide different outcomes. These results need to be tested and compared with what is actually observed in the universe. And new observations need to be interpreted in the light of current concepts to evaluate these. It is the intention of this thesis to contribute its (however small) part to this quest. State-of-the-art numerical codes and computers have been used to interpret new data *observing dust grain growth and sedimentation in circumstellar discs* and to identify and provide *interpretations and predictions of their observable quantities in a multi-wavelength approach* for further enlightenment.

This thesis is organised as follows: In the following Chapter, the basic concepts of circumstellar discs will be introduced. This includes the notion of the disc itself and its description, a discussion of the dust in the disc, a summary of observation techniques, and an introduction into the radiative transfer techniques fundamentally used in this work. The Chapter closes with a summary of the aims of this thesis. The subsequent Chapters are each dedicated to the application of radiative transfer calculations to specific models of circumstellar discs and the interpretation of the respective results. In Chapter 3, the interpretation of existing observational data of the circumstellar disc in the Bok globule CB 26 will be the main focus, and in Chapter 4 it will be the high mass candidate IRAS 18151-1208. Chapter 5 features the prediction of observable effects of dust grain growth in future observations in general, while Chapter 6 does this for one specific model. Finally, Chapter 7 presents a reinterpretation of older existing models in light of new observations.

2. Basic considerations

> Φῶς δὲ αὐτοῖς πυρὸς ἄνωθεν καὶ πόρρωθεν καόμενον
> ὄπισθεν αὐτῶν, μεταξὺ δὲ τοῦ πυρὸς καὶ τῶν δεσμωτῶν
> ἐπάνω ὁδόν, παρ᾽ ἣν ἰδὲ τειχίον παρῳκοδομημένον, ὥσπερ
> τοῖς θαυματοποιοῖς πρὸ τῶν ἀνθρώπων πρόκειται τὰ
> παραφράγματα, ὑπὲρ ὧν τὰ θαύματα δεικνύασιν.
> ὁρῶ, ἔφη.
>
> *(Platon,* Πολιτεία*)*

In this Chapter, the basic physical ideas of the field are presented. The concepts and models discussed here form the very base of the subsequent Chapters. Model parameters such as the dust mineralogy, the central star, grain sizes and many more are referred to throughout this thesis.

2.1. Protoplanetary discs: Setting the stage

Circumstellar discs form in the stellar genesis by conservation of angular momentum from a parent interstellar molecular cloud that collapses due to instability from its own gravity. The central object of such discs is, in the low mass case, a so-called T Tauri star or, if more mass is involved, a Herbig Ae star. In the theory of stellar evolution, these stars are the respective progenitors of main-sequence stars. Throughout this thesis, an “average” T Tauri star as given by the survey of Gullbring *et al.* (1998) is employed. This star has a radius of $R_* = 2\,\mathrm{R}_\odot$ and an effective surface temperature of $T_{\mathrm{eff}} = 4000\,\mathrm{K}$. Assuming the star to be a black body radiator, this yields a luminosity of $L_* = 0.92\mathrm{L}_\odot$.

Weizsäcker (1948) shed the first light on the nature of astrophysical accretion discs in general. It has been shown that molecular viscosity in such discs alone is not able to provide enough radial transport of angular momentum in order to allow matter to be accreted by the central object, in contradiction to observation. Consequently, it has been theorised that some sort of turbulence is the major source of viscosity in astrophysical discs. The precise nature of this viscosity is still a matter of debate. A parametrised ansatz has been put forward by Shakura & Sunyaev (1973) that equates the local viscosity $\tilde{\nu}$ to the local sound speed c_s and the local disc pressure scale height h by a free parameter $\alpha_\nu < 1$:

$$\tilde{\nu} = \alpha_\nu c_\mathrm{s} h. \tag{2.1}$$

Although this work considered the theory of accretion discs around black holes in binary systems, the results haven proven to be useful to explain a much wider range of discs, including circumstellar discs around T Tauri stars (Lynden-Bell & Pringle, 1974; Shu, 1991; Beckwith *et al.*, 1996). In a more recent paper by Duschl *et al.* (2000), a more general concept, β-viscosity, is proposed and applied to protoplanetary discs. This scheme is based on hydrodynamically driven turbulence, and the viscosity is proportional to the distance from the central object and to the azimuthal velocity. Another source of viscosity might be provided by the magnetorotational instability that relies on the interplay between the differential orbital velocity and the coupling to the disc magnetic field of radially neighbouring charged particles and fluid elements. This mechanism has first been investigated by Balbus & Hawley (1991).

The evolution time scale of circumstellar discs is typically in the order of 10^6 yr and after $\sim 10^7$ yr the gaseous part of the disc has dispersed (Strom *et al.*, 1989; Haisch *et al.*, 2001). After this time, the gas has been mostly removed from the disc by accretion to the central star, lost to the environment due to stellar winds, or blown out of the system by jets and molecular outflows. In this later stage, called 'debris disc', the dust (especially the small dust grains) is then subject to removal by the Poynting-Robertson effect and radiation pressure. However, the disc is not free of small grains. This is due to collision of larger dust grains thereby replenishing the population of small grains in a 'second generation' (Backman & Paresce, 1993). The transition stage between the circumstellar disc phase and the debris disc phase is called the transitional disc and is of particular interest as these systems might already harbour planets and still show major features of the original circumstellar disc.

In this thesis, the density distribution of the disc is described using a parametrised ansatz. This strategy has already been successfully used to describe the appearance of various edge-on discs, such as the Butterfly-Star IRAS 04302+2247 (Wolf *et al.*, 2003), HK Tau (Stapelfeldt *et al.*, 1998), HV Tau (Stapelfeldt *et al.*, 2003), and IM Lupi (Pinte *et al.*, 2008). This ansatz can be written as

$$\rho_\mathrm{disc}(\vec{r}) = \rho_0 \left(\frac{R_{100}}{r_\mathrm{cyl}}\right)^\alpha \exp\left(-\frac{1}{2}\left[\frac{z}{h}\right]^2\right) \tag{2.2}$$

where z is the usual cylindrical coordinate with $z = 0$ corresponding to the disc mid-plane and r_cyl is the radial distance from this z–axis. The parameter ρ_0 is determined by integrating Equation 2.2 and equating the result to the dust mass of the entire disc. R_{100} is a normalising constant, throughout this thesis $R_{100} = 100\,\mathrm{AU}$, and h, the vertical scale height, is a function of r_cyl

$$h(r_\mathrm{cyl}) = h_0 \left(\frac{r_\mathrm{cyl}}{R_{100}}\right)^\beta . \tag{2.3}$$

The quantities α, β, and h_0 in Equation (2.3) are geometrical parameters. The literature holds different, although similar, values for β, e.g. $\beta = {}^9\!/_8$ (Kenyon & Hartmann, 1987), $\beta = {}^5\!/_4$ (D'Alessio *et al.*, 1999a), and $\beta = {}^{58}\!/_{45}$ (Chiang & Goldreich, 1997), each considering different degrees of disc flaring. The viscous accretion theory by Shakura & Sunyaev (1973) expresses α in terms of β:

$$\alpha = 3(\beta - {}^1\!/_2). \tag{2.4}$$

Within this thesis, β is treated as a free parameter in order to investigate different degrees of disc flaring. Integrating Equation (2.2) along the z axis yields the surface density

$$\Sigma(\vec{r}) = \Sigma_0 \left(\frac{R_{100}}{r_\mathrm{cyl}}\right)^{p_\Sigma} . \tag{2.5}$$

Comparison with Equation (2.2) yields the following relation between the exponent of the surface density power law and the geometrical parameters of the ansatz

$$p_\Sigma = -\beta + \alpha. \tag{2.6}$$

2.2. Dust: Building blocks of planets

Let us turn now to the constituents of the disc and their physics. Although the vast majority of mass resides in molecular H_2 gas, it is the dust (mostly silicates) that provides the building blocks for planets (or their cores, respectively) (Williams & Cieza, 2011).

Dust grains in the interstellar medium (ISM) that form the parent molecular cloud can be described by a grain size distribution with a maximum grain size of $a_\mathrm{max} = 250\,\mathrm{nm}$ (Mathis *et al.*, 1977). It has been shown by Kemper *et al.* (2004) that amorphous grains, which account for more than 98% of the dust in the ISM, are smaller than 100 nm after contradicting findings by Witt *et al.* (2001) and Draine & Tan (2003) from X-ray scattering observations. Molecular clouds are the densest regions of the ISM.

Growth of dust grains starts already in the molecular cloud as observed by e.g. Wilking *et al.* (1980) and modelled by Ossenkopf (1993) and Weidenschilling & Ruzmaikina (1994). Ormel *et al.* (2009) showed that little coagulation can be expected if the cloud lifetime is limited by the typical free fall timescale on the order of magnitude of $\sim 10^5\,\mathrm{yr}$ as the timescale of coagulation is of the order $\sim 10^7\,\mathrm{yr}$. In contrast due to the higher densities, the dust grain coagulation timescale in discs is $\sim 10^4$ yr (Dullemond & Dominik, 2005).

Evidence for grain growth in T Tauri stars is plentiful and provided for example by spectroscopy at mid-infrared wavelengths (e.g. Przygodda *et al.*, 2003; Kessler-Silacci *et al.*, 2007). Also, low values for the spectral index of the emissivity in the millimetre regime tracing the densest disc regions close to the midplane, β_{mm}, indicates grain growth (Beckwith & Sargent, 1991)(see also Section 2.3.2).

In the evolutionary picture of circumstellar discs, dust grains grow from sub-micrometre sizes to millimetre-sizes via coagulation. This hit-and-stick process depends on numerous properties of the dust grains such as their morphology and their relative velocities for example. Observational evidence for grain growth has been found, for instance, for the circumstellar discs IM Lupi (Pinte *et al.*, 2008), GG Tau (Duchêne *et al.*, 2004; Pinte *et al.*, 2007), HH 30 (Watson & Stapelfeldt, 2004), IRAS 04302+2247 (Wolf *et al.*, 2003), and VV Serpens (Alonso-Albi *et al.*, 2008).

A considerable amount of work has been done to understand the physics of dust grain coagulation and settling, including extensive numerical simulations on the topic, as well as dust coagulation studies in laboratories. A comprehensive treatment can be found in a series of papers by Blum *et al.* (2006); Langkowski *et al.* (2008); Weidling *et al.* (2009); Güttler *et al.* (2009).

According to Cuzzi *et al.* (1993), dust grains smaller than ~ 1 cm in circumstellar discs can be described within the Epstein regime as the mean free path length of a dust grain is much larger than its diameter. Then the coupling of the dust grains to the gas disc can be described by the function of the dust grains cross-section. The drag force of the gas F_{d} on a particle of mass m_{P} can be expressed as

$$F_{\mathrm{d}} = m_{\mathrm{P}} \frac{\rho_{\mathrm{gas}}}{\rho_{\mathrm{dust}}} \frac{c_{\mathrm{s}}}{a} v_{\mathrm{rel}}, \tag{2.7}$$

where ρ_{gas} denotes the gas density, ρ_{dust} the material density of the dust, c_{s} the local sound speed, a the dust grain radius, and v_{rel} the relative velocity between gas and dust. Hence, small dust grains couple much better to their gas environment than large grains do. Circumstellar discs are understood to be pressure-stabilised against the gravity of the star perpendicular to the disc midplane. As a consequence, larger grains experience a much stronger gravitational force along this direction than smaller grains. When a dust grain has reached a certain size, its coupling to the gas will weaken and allow it to settle closer to the midplane. Effectively, this leads to a mass-transfer from upper disc regions towards the midplane D'Alessio *et al.* (2006). Dullemond & Dominik (2004) showed that as the disc is depleted in its upper layers, implications to the disc's thermal structure and optical depth profile are inevitable. An in-depth treatment of the dust layer in a circumstellar disc up to the onset of hydrodynamical stability can be found in Garaud & Lin (2004). They argue that for a more complete analysis of the situation besides settling, turbulent motion of the gas needs to be considered as well.

Due to the turbulent motion of the gas in deeper disc layers dust grains effectively settle at maximum to their respective sedimentation height. Compared with a disc life time of $\sim 10^6$yr (Sicilia-Aguilar *et al.*, 2009), sedimentation is a rather quick process, especially in the upper disc layers. Dust settling depletes these layers in some 10^3yr to 10^4yr (Dullemond & Dominik, 2004). The physical effect that controls the time scale for the observables to change is grain growth: As soon as a grain has grown to larger sizes, it will settle almost immediately.

However, the road from dust grains to planetesimals is not as clear as might have been suggested by the considerations thus far. As Weidenschilling & Cuzzi (1993) showed, particle fragmentation will dominate the evolution of dust grains when they reach a size of typically 1m. At this size the dust 'pebbles' are still too small to enable gravitational growth to larger sizes. This effectively stops the growth of dust and prohibits the creation of planet cores in the current theoretical understanding. This effect has become known as the 'meter-size-barrier'.

Research in the last years has shown that the situation is actually worse than that: Further barriers prohibiting dust grain growth have been shown to exist. Very recently, the existence of a "frozen zone" has been shown by Okuzumi *et al.* (2011a,b), where the nonzero electric charge of dust grains inhibits grain growth. This electrostatic barrier limits dust aggregate masses to $\approx 10^{-7}$g at 1 AU.

Brauer *et al.* (2007) showed that also radial drift into the star is a problem for meter-sized pebbles at 1AU distance from the star such that any larger body on its route to become massive enough to grow via gravitation is swallowed by the star. At 50AU, this barrier is shifted towards even smaller particles of a few $^1/_{10}$m in size. An analysis of the radial drift of dust grains can further be found in Brauer *et al.* (2008a) and Birnstiel *et al.* (2010a). A possible way around this radial drift barrier and its observational consequences will be the focus of Chapter 6. Another barrier has been introduced by Zsom *et al.* (2010), called the bouncing barrier. This barrier is important for dust grains of some mm to cm in size and prohibits dust grain growth as mere bouncing appears to be the typical outcome of particle collisions instead of growth or fragmentation. The precise outcome of a particle collision however is quite dependent on the material properties such as porosity, particle shape, and collision velocity. Further complications arise if coating of dust grains and/or organic material is also taken into account (Dominik & Tielens, 1997; Wada *et al.*, 2007, 2008).

2.2.1. Dust grain properties

For the purpose of this work, the dust grains are assumed to be homogeneous spheres. Real dust grains, of course, are expected to feature a much more complex and fractal structure. As discussed by Voshchinnikov (2002), chemical composition, size and shape of dust grains cannot be determined separately in astronomical observations, but only as a combination. Therefore, in the scope of this work, the models are limited to the less complex but also less ambiguous approach of spherical, non-aligned and non-orientated dust grains.

For the chemical composition of the dust grains a model is employed that incorporates both silicate and graphite material. Applying the cosmic abundance ratio from silicate to graphite of $1 \times 10^{-27}\,\mathrm{cm^3 H^{-1}} : 1.69 \times 10^{-27}\,\mathrm{cm^3 H^{-1}}$, a relative abundances of 62.5% for astronomical silicate and 37.5% graphite is derived. Further, an average grain matter density of $\rho_{\mathrm{grain}} = 2.5\,\mathrm{g\,cm^{-3}}$ is adopted.

For the grain size distribution a power law of the form

$$n(a) \sim a^{-3.5} \quad \text{with} \quad a_{\min} < a < a_{\max} \tag{2.8}$$

is assumed. Here, a is the dust grain radius and $n(a)$ the number of dust grains with a specific radius. For $a_{\min} = 5\,\mathrm{nm}$ and $a_{\max} = 250\,\mathrm{nm}$ this distribution becomes the commonly known 'MRN' distribution of the interstellar medium by Mathis *et al.* (1977). In order to investigate grain growth in this work, the maximum grain size $a_{\max}$ will be used as a parameter. The minimum grain size is not subject to change as small grains are understood to be replenished by collisions of larger grains.

2.2.2. Optics of dust

All information that can be obtained from circumstellar discs is delivered in the form of electromagnetic radiation, e.g. light. In order to understand what can be learned about circumstellar discs one therefore has to examine in which way the radiation on its way to the observer interacts with the matter in the disc.

In the scope of this thesis, all discs are considered to be passive, that is they are not the primary source of radiation. One thereby neglects accretion and turbulent processes within the disc as another possible intrinsic energy source. The only primary source of energy is hence the central T Tauri star, which is assumed to be a black body radiator.

The propagation of light of frequency ν through matter can be described by the radiative transfer equation

$$\begin{aligned} \frac{1}{c}\partial_t I_\nu(\vec{n},\vec{r}) + \nabla_{\vec{r}} I_\nu(\vec{n},\vec{r}) = &- \rho(\vec{r})\,\left[\kappa_\nu^{\mathrm{abs}}(\vec{r}) + \kappa_\nu^{\mathrm{sct}}(\vec{r})\right] I_\nu(\vec{n},\vec{r}) \\ &+ \rho(\vec{r})\, j_\nu \\ &+ \rho(\vec{r})\,\kappa_\nu^{\mathrm{sct}} \int \mathrm{d}\Omega'\; \phi^{\mathrm{sct}}(\vec{n},\vec{n'})\; I_\nu(\vec{n'},\vec{r}), \end{aligned} \tag{2.9}$$

where c is the speed of light in vacuum. This is an integro-differential equation for the specific intensity I_ν at a position $\vec{r}$ in the direction $\vec{n}$. $\kappa_\nu^{\mathrm{abs}}$ and $\kappa_\nu^{\mathrm{sct}}$ are material parameters that describe the absorption and scattering behaviour of the material and ρ is the material density, respectively. The angular dependence of the scattering is described by ϕ^{sct}. The timescale of radiative transfer is much smaller than of any other physical process considered in this thesis. In this sense, I_ν can be considered static and the first term on the left hand side evaluates to zero. The emissivity due to thermal emission of the material is given by the term j_ν. The systems considered in this thesis are understood to be in thermal equilibrium and hence j_ν can be expressed by $j_\nu = \kappa_\nu B_\nu(T)$. $B_\nu(T)$ is the specific radiative intensity of a black body of temperature T:

$$B_\nu(T) = \frac{4\pi\hbar\nu^3}{c^2} \frac{1}{\mathrm{e}^{\frac{2\pi\hbar\nu}{k_\mathrm{B}T}} - 1}, \tag{2.10}$$

where $\hbar$ is the reduced Planck's constant, ν the radiation frequency, and k_B Boltzmann's constant. A rigorous derivation of Equation (2.9) can be found in Padmanabhan (2000). Equation (2.9) in essence simply combines all the possible fates of a light ray along its way through the disc: that is absorption by a dust grain (and consequently conversion of radiation energy into thermal energy of the grain), scattering by a grain of light out of the ray and also into it, and contributions to the radiation of thermally emitting dust. The techniques used to solve this equation are described in section 2.4. The focus in the remainder of this section will be the optical properties of the disc material that enters Equation (2.9) via the material constants $\kappa_\nu^{\mathrm{abs,sct}}$.

An important notion in the interaction between matter and radiation is the optical depth τ_ν or τ_λ. It is defined at a point s by integration of the absorption and scattering coefficients along the beam:

$$\tau_\nu(s) = \int_0^s \mathrm{d}x \; \rho(\vec{x}) \; \left[\kappa_\nu^{\mathrm{abs}}(\vec{x}) + \kappa_\nu^{\mathrm{sct}}(\vec{x})\right]. \tag{2.11}$$

It is a common agreement that $\tau_\lambda \approx 1$ is viewed as a borderline: Objects with an optical depth $\tau_\lambda \ll 1$ are considered transparent while objects with $\tau_\lambda \gg 1$ are understood to be opaque. If emission is ignored, then the intensity I_x of a light ray at a point x is given by the initial intensity I_0 via

$$\frac{I_x}{I_0} = \mathrm{e}^{-\tau_\lambda(x)}. \tag{2.12}$$

The observed radiation of circumstellar discs has two major origins. On the one hand, at short wavelengths $\lambda \lesssim 5\,\mu$m scattered stellar light dominates (see Section 5.2). Typically, circumstellar discs are massive enough such that at least in their midplane the optical depth is very high and it rapidly diminishes towards higher disc layers. Especially in these transition regions, multiple scattering will occur. On the other hand, at larger wavelengths, thermal re-emission of dust grains is the major contributor. Thermal re-emission is due to absorption of stellar light by dust grains, which heats them up, and can be described by black body radiator as well. Of course, there is no sharp transition between these two regimes, as short-wavelength radiation of hot dust grains is also subject to (multiple) scattering.

It is possible to limit radiative transfer calculations through the dust and neglect line emission and absorption by the gas. This is justified as the dust is the dominant coolant of the disc. Hence, thermal equilibrium obtained in radiative transfer calculations based on dust only will provide a reliable description of the disc's thermal structure. This assumption is based on the work of Kamp & Dullemond (2004), who showed that dust and gas temperature in a circumstellar disk around a T Tauri star are well coupled in the regions which are sufficiently dense to be traced with current and near-future (sub)millimetre observatories. Therefore, it is the dust whose density structure is described by Equations (2.2) and (2.3) for the purpose of this thesis. Yet, the gas is the dominant matter fraction of the disc with respect to mass. The standard value for mass relation of dust and gas is

$$\frac{m_{\mathrm{gas}}}{m_{\mathrm{dust}}} = 100 \tag{2.13}$$

which is in agreement with the findings by Glauser *et al.* (2008).

If the dust grains are assumed to be homogeneous spheres, then absorption and scattering can be described by Mie theory (Mie, 1908). In order to do so, equilibrium solutions to the Maxwell Equations are obtained by respecting proper boundary conditions and the smooth transition of the electromagnetic field from the vacuum to the grain interior at the grain's surface. Bohren & Huffman (1998) describe how the absorption, extinction and scattering cross sections C_{abs}, C_{ext}, and C_{sct} can be calculated from the material's complex refractive indices (or, equivalently, its dielectric constants) and from the size parameter $\tilde{x}$

$$\tilde{x} = 2\pi\frac{a}{\lambda}, \tag{2.14}$$

which is determined by the particle radius a and the wavelength λ of the electromagnetic field. The cross sections translate into dimensionless efficiency factors

$$Q_{(\mathrm{abs,ext,sct})} = \frac{C_{(\mathrm{abs,ext,sct})}}{\pi a^2} \tag{2.15}$$

by normalisation to the cross section area of the interacting grain, where a is the grain's radius. If the dust grain is embedded in a non absorbing material (i.e. vacuum), then the following relation holds:

$$Q_{\mathrm{abs}} = Q_{\mathrm{ext}} - Q_{\mathrm{sct}}. \tag{2.16}$$

For the optical data, the complex refractive indices of "smoothed astronomical silicate" and graphite are used as published by Weingartner & Draine (2001). Since the longest wavelength considered in this work is 2.7 mm, the refractive indices are extrapolated to that wavelength. This is readily done since for this wavelength regime both the real and the imaginary part of the refractive index show asymptotic behaviour. For graphite the common "$\frac{1}{3}$ − $\frac{2}{3}$" approximation is used. That means, if Q_{ext} is the extinction efficiency factor, then

$$Q_{\mathrm{ext,graph}} = \frac{1}{3}Q_{\mathrm{ext}}(\epsilon_{\|}) + \frac{2}{3}Q_{\mathrm{ext}}(\epsilon_{\perp}), \tag{2.17}$$

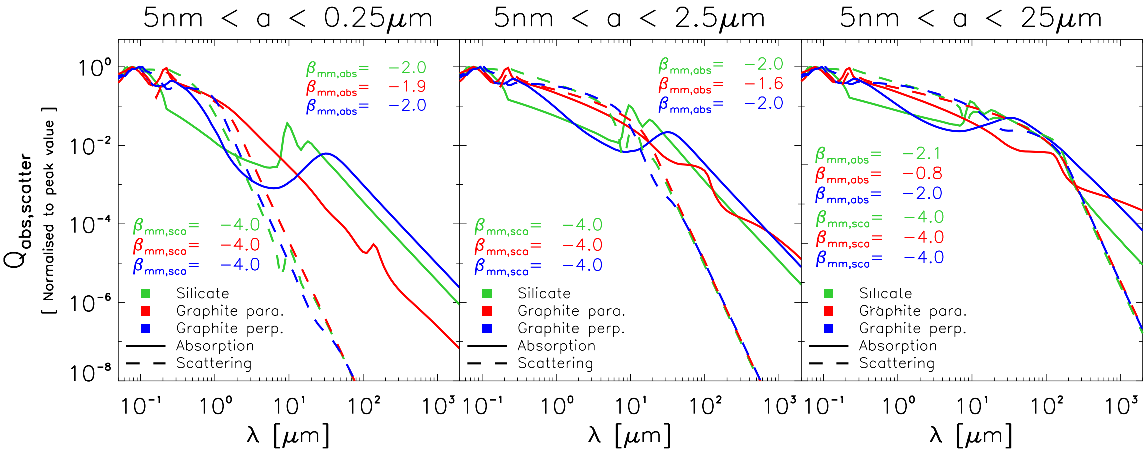

Figure 2.1.: Influence of the upper grain size on the scattering and absorption features of a dust grain species. The grain size distribution scales as $n(a) \sim a^{-3.5}$ in all three set-ups.

where $\epsilon_{||}$ and $\epsilon_{\perp}$ are the graphite dielectric tensor's components for the electric field parallel and orthogonal to the crystallographic axis, respectively. As has been shown by Draine & Malhotra (1993), this graphite model is sufficient for extinction curve modelling. The inclusion of graphite has implications not only for micrometre wavelengths for μm-sized grains but also for millimetre wavelengths. Figure 2.1 illustrates this effect. The results of Chapter 3 will show implications of this in the interpretation of observational data.

The reason why dust grain growth affects observable quantities can be seen by comparing the luminosity of grains with different radii. For a given material, an easy way to do this is to compare the total luminosity of two grain populations with the same total mass at the same temperature but with different grain radii. The total luminosity L_{tot} of a grain population with a single grain radius a is proportional to the number of grains n and the luminosity of a single grain L:

$$L_{\text{tot}_\lambda} \sim n\, L_\lambda. \tag{2.18}$$

The luminosity of a single grain is related to its radius a, its material-dependent absorption efficiency Q_{abs} and the black body luminosity $B_\lambda(T)$ of a given temperature T by

$$L_\lambda \sim a^2\, Q_{\text{abs}}\, B_\lambda(T). \tag{2.19}$$

If the luminosity of different grain sizes with the same total dust mass m_{dust} at the same temperature T are compared, m_{dust} and $B_\lambda(T)$ cancel. With the density ρ_{grain} of one grain and the relation between volume and radius for spherical grains $m_{\text{grain}} = \frac{4}{3}\,\pi\, a^3\, \rho_{\text{grain}}$ one obtains the following relation for the total luminosity of a

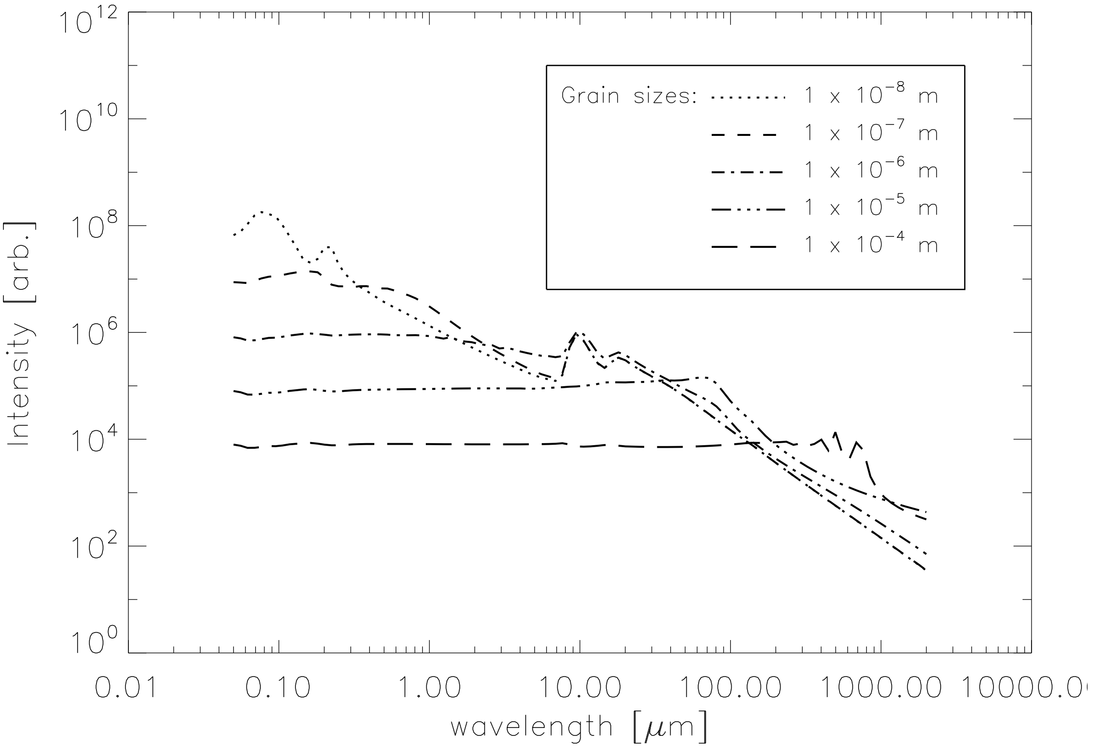

Figure 2.2.: Spectral luminosity of different grain populations. Each grain population features grains of a fixed size ranging from 10^{-8}m to 10^{-4}m. All populations have the same total mass, resulting in fewer grains for populations with larger grain radii.

dust population:

$$L_{\mathrm{tot}_\lambda} \sim \frac{Q_{\mathrm{abs}}}{a}. \tag{2.20}$$

Figure 2.2 shows this result for different grain radii spanning the range from $a = 10^{-8}$m up to $a = 10^{-4}$m and a mixture of graphite and silicate grains according to cosmic abundances. Each grain population has the same total mass, resulting in fewer emitting particles in the case of populations with larger grains. As the grains grow, their peak luminosity shifts to larger wavelengths accordingly illustrating the strong wavelength dependence of the optical properties of the disc. Similar observations apply to the scattering properties of dust grains as well, since for a given material, in Mie-theory (Mie, 1908) the scattering efficiency Q_{scatt} is only a function of the size parameter $\tilde{x}$:

$$Q_{\mathrm{scatt}} = Q_{\mathrm{scatt}}(\tilde{x}). \tag{2.21}$$

For grains in the general setting of a circumstellar disc, this estimate of grain luminosity is simplistic as two points have been neglected. First, the temperature of a dust grain depends on its absorption efficiency $Q_{\rm abs}$ at the illuminating stellar emission wavelengths. Secondly, the luminosity of dust grains as an observable is degenerate with respect to dust grain size and mass.

In addition to the changing optical properties of the dust grains due to their size, grain sedimentation results in the modification of the disc density structure. As a consequence, the spatial structure of the optical depth τ_λ changes, yielding different temperature profiles in the disc and re-emission features of the disc as a function of its evolving state. The altered optical depth structure also has implications for the morphology of scattered light images (see Section 5.2.1 and Figure 5.4).

2.3. Observation: Looking yonder

2.3.1. Means of observation

In order to advance the knowledge of circumstellar discs one ought to understand and interpret the possible observational data. These data set come generally in two different classes. Spectroscopic or photometric flux measurements over a certain wavelength range or at a certain wavelength can be grouped in the first class. These observations carry no direct information about the spatial distribution of the flux[1]. Information about the spatial distribution are provided by the second class: images and interferometric observations. In turn, this kind of data provides no wavelength dependent information. Although this classification is not purely artificial or historical but also strongly induced by the technical difference of instruments of the two classes, in recent years instruments combining both kinds of observations have been successfully put into operation (e.g. the VLT/SINFONI instrument (Eisenhauer *et al.*, 2003)).

A comprehensive introduction into interferometry can be found in the paper by Haniff (2007). Interferometric observations and images are dual in the sense that while images probe the spatial intensity distribution $I(x, y)$ of the source, interferometric observations measure its Fourier counterpart $\hat{I}(u, v)$:

$$\hat{I}(u,v) = \iint\limits_{\mathbb{R}^2} \mathrm{d}x\,\mathrm{d}y\; I(x,y)\; \mathrm{e}^{-2\pi i(ux+vy)}. \tag{2.22}$$

For each point $\vec{U}$ in the (u, v)-plane one pair of antennae, providing one baseline $\vec{X}$ according to $\vec{U}(u, v) = \vec{X}/\lambda$ is needed. Consequently, large arrays of antennae are needed to achieve good representation of the spatial flux distribution. Nevertheless, very good spatial resolution can be achieved by choosing large baselines. For the

---

[1] However, spectral energy distributions allow to conclude about the spacial structure of the observed object by means of modelling.

currently under construction ALMA (Atacama Large Millimeter Array) observatory with 50 antennae, at the largest baseline of 16km, a spatial resolution of $0.005''$ at an observing wavelength of $\lambda = 345\,\mu$m is achieved (see also Figure A.1). However, only a complete sampling of the (u, v)-plane would allow a unique inversion of Equation (2.22). Due to the limited number of receivers each image reconstruction from interferometric observations necessarily involves uncertainties/artifacts.

Direct imaging techniques, that is the 'traditional telescope', face challenges of their own. Neglecting influences of the turbulent atmosphere, their resolution is diffraction limited. This means that a point source is smeared out and imaged as the so-called point spread function (PSF). The image of a point source, say a star, produced by a perfectly circular telescope is an Airy-disc. The minimal angular distance φ of two objects in the sky that can be resolved at the observing wavelength λ by such a telescope of diameter d is

$$\varphi \approx 1.22\,\frac{\lambda}{d}. \tag{2.23}$$

This assures that the maximum of the intensity diffraction pattern of the first object comes to rest in the first minimum of the second object. If two point sources are thought to be increasingly close to each other, their PSFs will progressively overlap and it will become difficult to distinguish between the two sources. The precise PSF of an observing instrument depends not only, though mainly, on its diameter but also on the shape of the mirror, the mounting and shape of secondary mirrors, and other instrument aspects. The factor 1.22 in Equation (2.23) actually refers to a circular aperture. For instance, in the case of the Hubble Space Telescope, the tool `TinyTim`[2] computes the respective PSF of the instrument at a given time and set-up.

In order to compare synthetic model images with real observations, the effect of the PSF has to be taken into account. This is done by convolving the model image's flux distribution with the appropriate PSF

$$\tilde{I}(x,y) = I(x,y) \otimes \mathrm{PSF}(x,y) = \iint\limits_{\mathbb{R}^2} \mathrm{d}x'\,\mathrm{d}y'\,I(x-x', y-y')\,\mathrm{PSF}(x',y') \tag{2.24}$$

Typically, model structures smaller than the PSF's full width at half its maximum (FWHM) are smeared out. As a consequence, larger and larger telescopes are being built in order to increase the spatial resolution. It is possible to assign an 'effective PSF' (see Figure 3.2) to interferometric observations that account for the discussed shortcomings of the incomplete sampling of the uv-plane and the maximum baseline $\vec{X}$ used. Throughout this thesis, the convolution of images with the appropriate PSF places severe constraints on the observability of model features.

As the next generation of telescopes and interferometers with high spatial resolution will commence in the not so distant future, it is vital to investigate whether

---

[2] `http://www.stsci.edu/hst/observatory/focus/TinyTim`

Band name	I	J	H	K	L	M	N	Q
Central wavelength $[\mu\mathrm{m}]$	1.00	1.25	1.65	2.20	3.45	4.70	10	20

Table 2.1.: Astronomical bands in the infrared.

Instrument	Wavelength regime $[\mu\mathrm{m}]$	Max. angular resolution [mas]
Herschel Space Observatory	55 – 672	4‘000
Giant Magellan Telescope (GMT)	0.32 – 25	3.2 – 250
Thirty Meter Telescope (TMT)	0.32 – 28	2.7 – 235
European Extremely Large Telescope (E-ELT)	0.32 – 24	1.9 – 144
Atacama Large Millimeter Array (ALMA)	350 – 10‘000	5
Magdalena Ridge Observatory (MRO)	0.6 – 2.4	0.3
Very Large Telescope Interferometer (VLTI)		
VLTI Spectro-Imager (VSI)	1.2 – 2.2	1.1
Multi Aperture Mid-Infrared Spectroscopic Experiment (MATISSE)	2.7 – 13	2
Keck Interferometer (KI)	10	5

Table 2.2.: Overview of future instruments, their observing wavelength and maximum spatial resolution.

and how grain growth and settling can be constrained by spatially highly resolved images of circumstellar discs. Table 2.2 gives an overview about future and only very recently existing instruments.

A severe limitation for all ground-based instruments is the transparency of the Earth's atmosphere. For wavelengths between $0.8\,\mu\mathrm{m} \lesssim \lambda \lesssim 2\mathrm{cm}$, only certain atmospheric windows exist. Especially for observations in the infrared, it is common to specify the observing wavelength by the name of the observing band. Each of these bands is associated with one of the atmospheric windows. Table 2.1 lists name of these bands and their central wavelength.

2.3.2. Observational appearance of circumstellar discs

The first hint towards the existence of circumstellar discs came by the deviations from the black body law observed at near-infrared (NIR) wavelengths in the spectral energy distribution (SED) of young stellar objects (YSO) (Adams *et al.*, 1987; Kenyon *et al.*, 1993, e.g.). The observed excess has its origin in the thermal re-emission of dust grains.

Equation (2.19) shows that the luminosity is proportional to the material features (Q_{abs}) and to the black body spectrum $B_\lambda(T)$. Due to the temperatures encountered in the context of circumstellar discs, for wavelengths $\lambda \gg 100\,\mu\mathrm{m}$ Equation (2.10) can be approximated by the Rayleigh-Jeans law

$$B_\nu = 2k_\mathrm{B}T\frac{\nu^2}{c^2}, \tag{2.25}$$

which exhibits a power-law dependence of the flux on the observing frequency/wavelength. If the disc is optically thin in the millimetre wavelength regieme, that is if $\tau_\nu \ll 1$, then it is possible to infer on grain sizes present in the disc by the millimetre slope of the SED. The frequency dependence at large wavelengths of Q_abs is a fixed power-law $Q_\mathrm{abs} \sim \nu^\beta_\mathrm{mm} \sim \lambda^{-\beta_\mathrm{mm}}$ with some exponent β_mm. This exponent β_mm in turn depends on the ratio between the grain size and the observing wavelength ${}^{\lambda}\!/_{a}$. For very small grains, $\lambda \gg a$, the exponent is approximately $\beta_\mathrm{mm} \approx 2$, while for grains much larger then the observing wavelength, $\lambda \ll a$, $\beta_\mathrm{mm} = 0$. Grain sizes comparable to the wavelength assure a smooth transition of β_mm. The total slope of the SED in the millimetre regime is $S_\lambda \sim \lambda^{-\beta_\mathrm{mm}}\lambda^{-2}$, where the 2 originates from Equation (2.25). Sometimes, this total slope is called $\alpha_\mathrm{mm} = 2 + \beta_\mathrm{mm}$ to include the slope due to the Rayleigh-Jeans law.

Lada & Wilking (1984) introduced a classification scheme for classical T Tauri stars (CTTS) based on the fluxes at wavelengths of 2.2 μm – 10 μm. Generally, the spectral energy distribution (SED) of more evolved and settled discs displays a smaller excess at longer wavelengths from the NIR to millimetre wavelengths (Dullemond & Dominik, 2005) (cf. also Figure 5.2). Cohen & Witteborn (1985) showed that silicate emission features at 10 μm are common in T Tauri stars and Meeus *et al.* (2009) showed that the strength and shape of the 10 μm feature in T Tauri stars are related to grain growth. D'Alessio *et al.* (2006) states essential effects of grain growth and dust sedimentation on the SED distribution of the disc that can be summarised as follows:

- More settled discs feature a smaller far-infrared (FIR) excess.
- More settled discs yield lower midplane temperatures and consequently less flux in the millimetre regime.
- Discs seen edge-on lack flux at intermediate wavelengths as a result of high optical depth at short wavelengths. A higher degree of sedimentation yields less extinction of the stellar light.

However, when fitting SEDs to observations, disc parameters are often degenerate (e.g. Thamm *et al.*, 1994; Boss & Yorke, 1996; Schegerer *et al.*, 2009). Further, the SED is a spatially integrated observable of a disc at many wavelengths. Hence, the SED can constrain them only very weakly as demonstrated by Robitaille *et al.* (2007).

The appearance of circumstellar discs in images quite depends on the inclination under which the disc is seen and, especially in the case of discs seen edge-on, on the observing wavelength. While at small wavelengths ($\sim$ μm) the disc midplane is

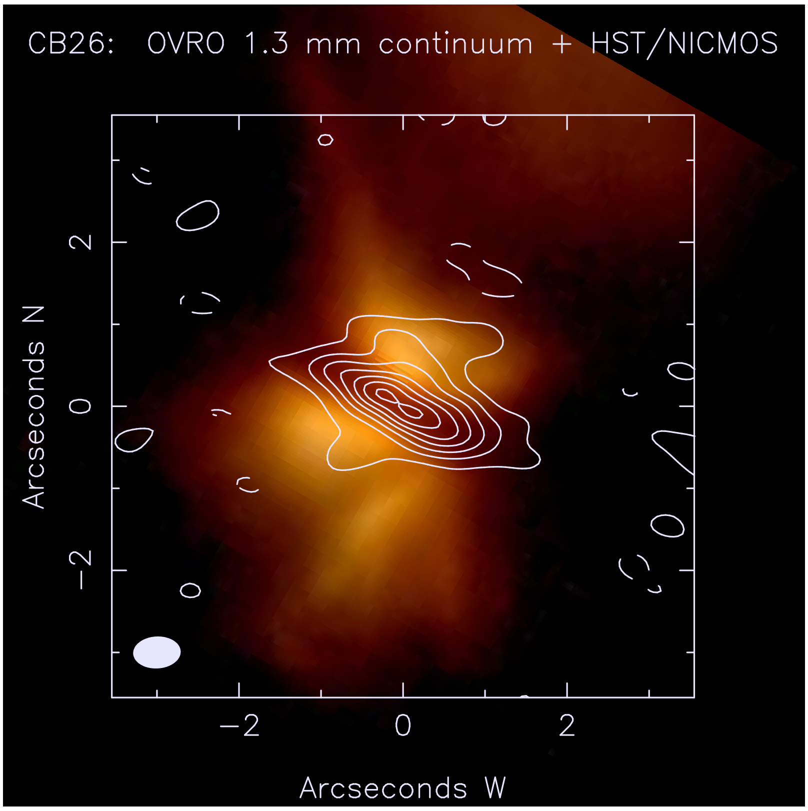

Figure 2.3.: Overlay of the OVRO 1.3 mm continuum map and the HST NICMOS images. The NICMOS colour image is a 3-colour composite of F205W, F160W, and F110W (in the RGB colour planes, respectively), shown in log stretch. The contour levels are linear, with the lowest contour at about the 2.5 σ-level, the others at the 6, 10, 14, 22, and 25 σ-level, respectively.

opaque to the stellar light and hence only upper (and lower) disc layers can be seen by scattered stellar light. At millimetre wavelengths, the midplane is the only visible constituent of the disc, seen as a glowing elongated structure. Figure 2.3 gives an impression of the edge-on seen disc CB 26, which will be the focus of Chapter 3.

While millimetre observations are sensitive only to radiation being emitted from dust in the densest region within the disc, NIR images are dominated by scattered stellar light from dust in the circumstellar envelope and the upper, optically thin disc layers. These observations trace different physical processes (scattering/re-emission) in different regions of the circumstellar environment, but they are both strongly related to the dust properties in the system. Watson *et al.* (2007) discuss the interpretation of images of multi-wavelength observations in detail. For example, the disc mass and the dust opacity cannot be disentangled as only their product is observable.

The effects of dust settling on images of protoplanetary discs in the optical wavelength range are discussed by Dullemond & Dominik (2004). McCabe *et al.* (2003) report the first resolved image of an edge-on disc in the N band and demonstrate that at this wavelength the extent of the scattered light nebula is very sensitive to the grain size distribution. Experience from modelling individual discs have shown that multi-wavelength, spatially resolving images are needed to allow constraint of the disc density structure and dust grain properties (Wolf *et al.*, 2003; Pinte *et al.*, 2008; Sauter *et al.*, 2009; Duchêne *et al.*, 2010).

2.4. Radiative transfer

To connect models of circumstellar discs and observations, radiative transfer calculations are needed. The fundamental tool used in this thesis to perform these computations is the program `MC3D` (Wolf *et al.*, 1999; Wolf, 2003b). It does not solve Equation (2.9) directly but is based on the Monte-Carlo method.

In this concept, the spectral energy distribution of the primary light source, the star, is split up in a number of photon packages according to their wavelength's spectral contribution. The path of these photon packages is then followed. Absorption and scattering are in a stochastic manner regarded according to material properties. Typical numbers of photon packages range from 10^3 to 10^7, depending on the required resolution and quality of images. `MC3D` makes use of the temperature correction technique as described by Bjorkman & Wood (2001) and solves the continuum radiative transfer problem self-consistently. The optical properties of the dust grains (scattering, extinction and absorption cross sections, scattering phase function) and their interaction with the radiation field is calculated using Mie theory. Multiple and anisotropic scattering is considered. Further the absorption concept as introduced by Lucy (1999), and the enforced scattering scheme as proposed by Cashwell & Everett (1959) are being used.

In order to derive a spatially resolved dust temperature distribution, the model space has to be subdivided into volume elements inside which a constant temperature is assumed. Both the symmetry of the density distribution and the density gradient distribution have to be taken into account. In this thesis, a spherical model space is being used, centred on the illuminating star and an equidistant subdivision of the model space in the θ-direction, whilst a logarithmic radial scale is chosen in order to resolve the temperature gradient at the very dense inner region of the disc. The required spatial resolution at the disc inner radius rim of the models ranges from 10^{-4} AU up to 10^{-1} AU, and every grid cell outwards is 1% larger than its next inner neighbour.

The radiative transfer for all models in this thesis is simulated at 101 different wavelengths, logarithmically distributed in the wavelength range $[\lambda_{\min}, \lambda_{\max}] = [50\,\mathrm{nm}, 2.7\,\mathrm{mm}]$. To model the different grain sizes and chemical populations, one has to consider an arbitrary number of separate dust grain sizes within a given interval $[a_{\min} : a_{\max}]$. The observables derived from radiative transfer considering each grain species separately are close to the observables resulting from radiative transfer (RT) simulations based on weighted mean dust grain parameters of the dust grain ensemble (Wolf, 2003a). Thus, weighted mean values for the efficiency factors, cross sections, albedo, and scattering matrix elements are used. For each dust grain ensemble, 1000 logarithmically equidistantly distributed grain sizes within the interval $[a_{\min} : a_{\max}]$ have been taken into account for each chemical component in the averaging process.

2.5. Some remarks on methodology

To investigate the effects of dust grain growth and sedimentation on observable quantities and to derive constraints from and for observational quantities, four steps are needed: First, a model of a circumstellar disc has to be set up that includes the effects of dust settling and coagulation. Secondly, for all model parameters it has to be determined whether they shall be set to some typical value or if they should be allowed to vary within a certain range. In the third step, radiative transfer simulations for every model have to be performed. As a concluding fourth step, the results of the radiative transfer simulations have to be investigated for possible valid tracers of planetesimal evolution.

The procedure is essentially the same when vice versa observational data is interpreted, except that search in the fourth step is replaced by comparison of simulated data and observational data and the whole procedure is to be repeated until this comparison yields an acceptable agreement, the so-called best-fit model. The sets of observational data in this thesis include a wide range of multi-wavelength spatially resolved observations as well as (substantial) parts of the respective systems' SED. Hence, it is not straightforward to answer the question what is meant by the "best-fit model".

For each comparison between model and observation an individual χ_i^2 is obtained. For instance, for the SED it is

$$\chi^2_{\mathrm{SED}} = \sum_{\lambda} \frac{\left(f_{\lambda,\mathrm{model}} - f_{\lambda,\mathrm{observation}}\right)^2}{\Delta f_{\lambda,\mathrm{observation}}}. \tag{2.26}$$

Here, $\Delta f_{\lambda,\mathrm{observation}}$ is the error that is associated with each point $f_{\lambda,\mathrm{observation}}$ in the observational SED while $f_{\lambda,\mathrm{model}}$ is the respective value from the model. Usually, a reduced χ^2 is introduced to account for the number of measurements N and the number of parameters N_{p} to be fitted: $\tilde{\chi}^2 = \frac{\chi^2}{N-N_{\mathrm{p}}}$. A model fitting all data is expected to have a $\tilde{\chi}^2 \simeq 1$.

The same method in principle applies to comparisons between models and images as well. In particular, the method can be applied to cuts through the brightness distributions to compare data and model. For instance, for a horizontal cut through an image:

$$\chi^2_{\mathrm{cut}} = \sum_{x=-r_{\mathrm{out}}}^{+r_{\mathrm{out}}} \frac{(f_{x,\mathrm{model}} - f_{x,\mathrm{observation}})^2}{\Delta f_{x,\mathrm{observation}}}, \tag{2.27}$$

where f_x is now the respective flux at the spatial location x.

Advancing on that line of thought, one can construct an overall $\tilde{\chi}^2$ for the complete data set and the whole model in question. The total $\tilde{\chi}^2$ is then the sum

$$\tilde{\chi}^2_{\mathrm{total}} = \frac{1}{n_{\tilde{\chi}^2}} \left(\tilde{\chi}^2_{\mathrm{SED}} + \sum_{\mathrm{images}} \tilde{\chi}^2_i \right). \tag{2.28}$$

If there are, say, two images involved then $n_{\tilde{\chi}^2} = 3$.

But there is a caveat for the $\tilde{\chi}^2$ of images that needs attention. The issue arises from the interdependency of the pixels flux value. In all images in this thesis, the FWHM of the PSF larger is than one pixel. This means that the value of each pixel is not independent from its neighbouring pixels or pixels further apart. The value that χ^2_{cut} assumes for a model with no systematic errors is hence not the number of measurements, but the number of pixels involved. In order to employ a proper χ^2-test, one requires each measurement to be independent.

This thesis employs a rebinning of pixels whenever an image and a model are to be compared in the sense of Equation (2.27). The size of the binning is given by the FWHM of the respective PSF. The flux values of pixels along a cut through an image are averaged over the size of FWHM. This choice of the FWHM introduces a certain degree of arbitrariness. Firstly, because the binning of pixels needs besides the number of pixels (given by the FWHM) an offset where to start. And secondly, pixels farther apart than the size of the FWHM are also interdependent by some degree. Eventually, for all images one obtains a value for $\tilde{\chi}^2$ that is not easily interpreted. And it is hence not so easy to judge the quality of the best-fit model by just looking at the actual $\tilde{\chi}^2$ value.

Further, for images only certain features are required to be reproduced by the model since the image most likely will contain fluctuations that are not necessarily part of the observed system. Or the image might contain asymmetries of some higher order that cannot in principle be reproduced by a symmetric model. The use of a more detailed model in these cases tends not to account for that but will introduce unresolvable parameter degeneracies. These degeneracies also adds to the problem of how to interpret the $\tilde{\chi}^2$ as this means deviations from the images are allowed, especially in the outer regions of the envelope far above and below the midplane.

The next question is then how to give an estimate of the errors of the parameter values of a best-fit model for a given observation. Since the computation of any $\tilde{\chi}^2$ involves a substantial element of arbitrariness as outlined above, the estimation of errors is also affected. Based on $\tilde{\chi}^2_{\mathrm{total}}$ from Equation(2.28), modeling errors are given as the range where the model parameters can be altered without changing $\tilde{\chi}^2_{\mathrm{total}}$ more than 10%. Allowing for a larger variation of $\tilde{\chi}^2_{\mathrm{total}}$ than 10% gives generally worse results.

2.6. Aims of this work

As mentioned in the introduction, it is the aim of this thesis to offer new insights in the consequences of dust grain growth and settling for current and future observations. This is achieved in several consecutive steps. The first two Chapters (3 & 4) are dedicated to showing the capabilities of interpretation of state-of-the-art data. Thereby possibilities and limits towards identification of observational tracers for the onset of planet formation are shown. The following two Chapters (5 & 6) are dedicated to the investigation of observational tracers available with future instruments. The remaining Chapter (7) demonstrates, that even a single piece of new observational data can clearly change the interpretation of the evolutionary state of the dust towards planetesimals.

In more detail, the topics of the individual Chapters are as follows: Chapter 3 closely examines the disc in Bok Globule CB 26, a disc around a low-mass T Tauri star. Questions answered in this Chapter are:

1. To which extent is it possible to constrain geometrical disc parameters such as inner and outer radii?
2. To which extent is grain growth necessary to explain observations?
3. How detailed can the interpretation of observational data in a wide span of wavelengths be?

In Chapter 4, the wide applicability of the disc model based on Equation (2.2) is shown. While the role of discs for low mass T Tauri stars is well studied, their role for high-mass stars is not well defined. By interpreting observational data of IRAS 18151-1208 it is shown that the existence of discs might also be established in this regime. Thereby the route towards studying planet formation in massive star systems similar to the low-mass case is opened.

Chapter 5 investigates how dust grain growth and sedimentation induced changes of the disc structure can be observed using spatially high resolving instruments. These investigations will provide ideal means to verify current dust-coagulation models as well as to allow one to constrain the level of turbulence within circumstellar discs. This proceeding provides a first approach in addressing the need for a general investigation of the effects of dust grain growth and sedimentation on images from the near-infrared to the millimetre-regime. Generic indicators are identified that allow the classification of observations and point out directions of interest are worth a more detailed approach in subsequent studies. Addressed key questions are:

1. What are the general effects of the grain growth induced mass relocation on images of a disc seen at different inclinations and at different observing wavelengths?
2. Which tracers of dust grain growth and sedimentation are provided by edge-on millimetre images in general?
3. What can be learned by combining mid-infrared images at various inclinations?
4. How can grain growth and sedimentation be constrained by near-infrared images?

In Chapter 6 the observational consequences of dust trapping will be investigated. As hinted in Section 2.2 a trapping of dust particles in local pressure maxima might be one possibility to overcome the radial drift barrier. Consequently, it is vital to identify tracers of these trapped particles in order to see if this mechanism is indeed (one of) nature's ways to handle the formation of planetesimals.

Finally, in Chapter 7 new observations of the so-called 'Butterfly star' will be presented. These observations add further insight into this fascinating object and might very well be the first observational evidence of radial dependent dust grain settling.

3. The disc in the Bok globule CB 26

Ὅρα τοίνυν παρὰ τοῦτο τὸ τειχίον φέροντας ἀνθρώπους
σκεύη τε παντοδαπὰ ὑπερέχοντα τοῦ τειχίου καὶ
ἀνδριάντας καὶ ἄλλα ζῷα λίθινά τε καὶ ξύλινα καὶ παντοῖα
εἰργασμένα, οἷον εἰκὸς τοὺς μὲν φθεγγομένους, τοὺς δὲ
σιγῶντας τῶν παραφερόντων.
ἄτοπον, ἔφη, λέγεις εἰκόνα καιδεσμώτας ἀτόπους.

(Platon, Πολιτεία*)*

In this Chapter, new images of the circumstellar disc in the Bok globule CB 26 are presented that span over more than 3 orders of magnitude in wavelength. Also, the unresolved SED of the object is given. Based on these, a model is developed that is capable of explaining all these observations in a self consistent manner. This model offers several constrains on disc parameters such as the inner radius and the maximum grain size in the system. The content of this chapter has been published in *Astronomy & Astrophysics* (Sauter *et al.*, 2009).

3.1. Overview

CB26 is a small cometary-shaped Bok globule located about 10° north of the Taurus/Auriga dark cloud at a distance of 140pc (Launhardt & Sargent, 2001). An IRAS point source (IRAS 04559+5200) at its southwest rim suggests an embedded Class I young stellar object (YSO) (Stecklum *et al.*, 2004) source. Launhardt & Henning (1997) found an unresolved 1.3mm continuum source associated with the IRAS source.

Interferometric observations by Launhardt & Sargent (2001) showed that the major fraction of thermal dust emission at millimetre wavelengths has its origin in a young circumstellar disc with a diameter of about 400AU and a mass of about $0.1\,\mathrm{M}_\odot$. This disc is seen almost edge-on, so the central star is not visible directly. However, the spectral energy distribution suggests a Class I YSO with $L \geq 0.5\,\mathrm{L}_\odot$ (Stecklum *et al.*, 2004). From the ^{13}CO line emission and the Keplerian rotation curve, Launhardt

& Sargent (2001) derive a central stellar mass of $m_* = 0.5 \pm 0.1\,\mathrm{M}_\odot$. Furthermore, Launhardt *et al.* (2008) detected a jet-like molecular outflow emanating perpendicular to the plane of the disc. This outflow seems to be co-rotating with the disc.

The model is based on spatially resolved images of CB 26 in the millimetre regime from the Sub-millimetre Array (SMA) and the Owens Valley Radio Observatory (OVRO), high resolution images in the I,J,H, and K bands (see also Table 2.1) obtained with the the Near Infrared Camera and Multi-Object Spectrometer (NICMOS) and the Advanced Camera for Surveys (ACS) instruments on the Hubble Space Telescope (HST). The photometric data for the spectral energy distribution (SED) upon the model is based are provided by the Multiband Imaging Photometer for Spitzer (MIPS) and the Infrared Array Camera (IRAC) aboard the Spitzer Space Telescope (SST) and millimetre photometry. A spectrum of the object is obtained with the Infra-Red Spectrograph (IRS) aboard the SST.

The model consists of two parts. First, an optically thick dust disc which accounts for the dark lane seen in images obtained with the HST of the object and the significantly elongated intensity profiles in the mm range. The second component is an optically thin envelope that reproduces the near-infrared scattered light nebulosity. Thus, it is possible not only to model observations on the common basis of one set of parameters, but also to investigate whether the dust properties are different in the disc and the envelope. This has been suggested by investigations of dust evolution in circumstellar discs where dust grain growth alters the dust grain properties in the circumstellar disc quite considerably whilst it is of less importance in the low-density envelope.

3.2. Observations

In this section, the set of observational data that includes not only the SED from $0.9\,\mu$m to 2.7 mm, but also resolved images in the near-infrared and millimetre regimes, will be briefly discussed.

3.2.1. The central star

The central star of the system is not observed directly for the following two reasons:

1. In the far infrared and at longer wavelengths, where the disc becomes less opaque with increasing wavelength, the contribution to the spectral energy distribution from the dust is orders of magnitude larger than that coming from the star.

2. In the optical, near, and mid-infrared bands, the disc becomes opaque, and the star is shielded from direct view.

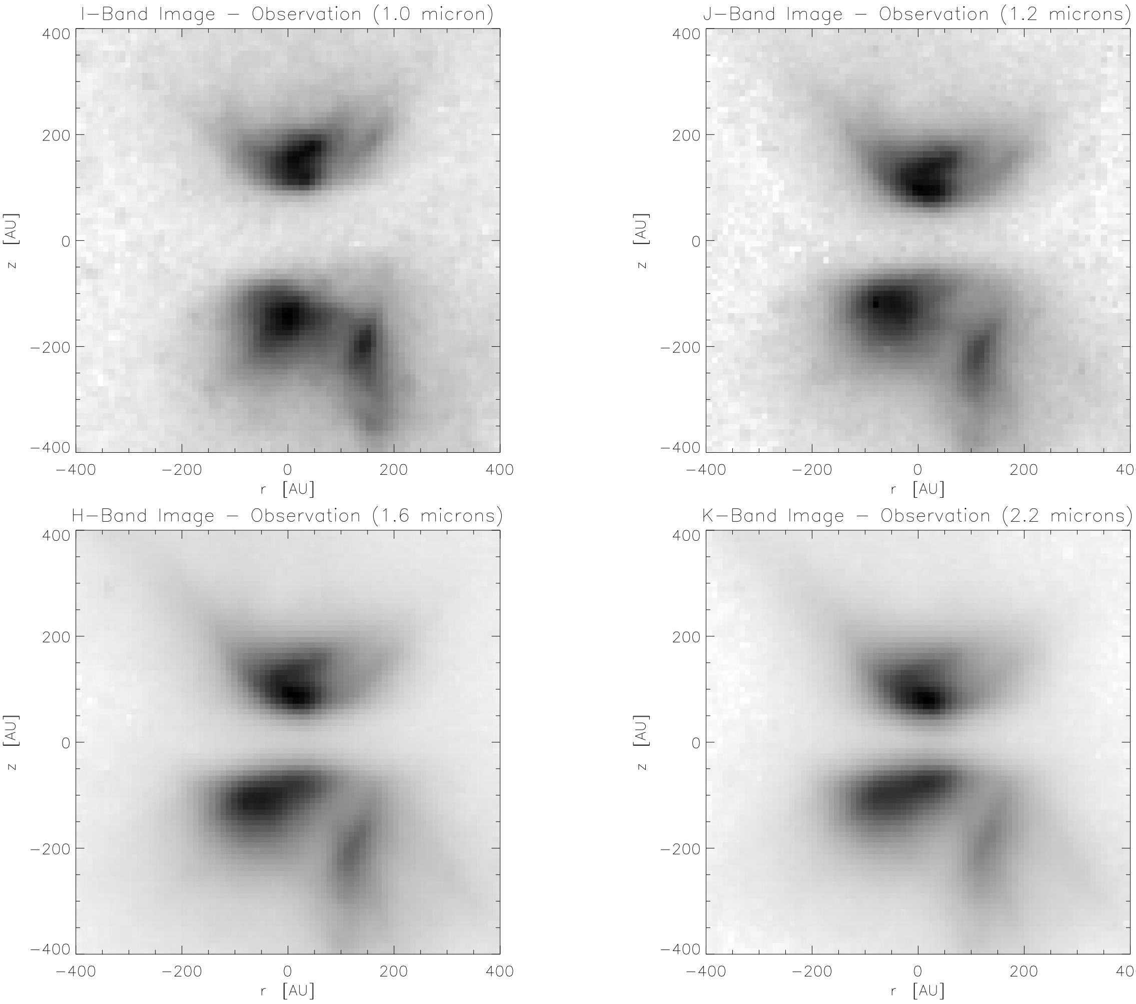

Figure 3.1.: Inverse HST images obtained with ACS and NICMOS in the I, J, H and K band. The colour scale is $\sim S^{\frac{2}{5}}$ All four images have been rotated by $-30°$ in order to align the major axis of the dark lane with the horizontal axis. For the image scale a distance to the object of 140pc is assumed ($100\,\mathrm{AU} = 0.7''$). The image orientation is PA 330° up, and PA 60° to the left.

Hence, in all observational data, the disc is the dominant contributor to the observed fluxes (either via scattering of stellar light or via thermal re-emission).

3.2.2. Near-Infrared Imaging

Near-Infrared images were taken with instruments aboard the Hubble Space Telescope. The NICMOS and ACS data were taken by the GEODE[1] team.

CB 26 was observed with the Advanced Camera for Surveys Wide Field Channel on 2005 September 09. Two 1250sec exposures were made in the F814W filter ($\lambda = 0.80\,\mu$m, $\Delta\lambda = 0.15\,\mu$m). CB 26 was also observed using NICMOS on 2005 September 15 with the F110W ($\lambda = 1.12\,\mu$m, $\Delta\lambda = 0.16\,\mu$m), F160W ($\lambda = 1.60\,\mu$m, $\Delta\lambda = 0.12\,\mu$m) and F205W ($\lambda = 2.06\,\mu$m, $\Delta\lambda = 0.18\,\mu$m) filters on the NIC2 array.

The images from the HST in I, J, H, and K bands are shown in Figure 3.1. All four images have been rotated in order to align the major axis of the dark lane with the horizontal axis. The emission seen on these images is scattered light from the central star. A dark shadowy linear feature that intersects the bipolar structure is present in all images. The dependence of its width on the wavelength is clearly visible. Since one expects the circumstellar disc to be optically thick at these wavelengths, the dark lane is interpreted as the disc's shadow in the encompassing envelope structure. The bipolar nebula also shows a complex morphology far above and especially below the disc.

3.2.3. Millimetre and Sub-millimetre measurements

Observations at 1.1 mm with the Sub-Millimetre Array (SMA) (Ho *et al.*, 2004) were made in December 2006, in two configurations providing baselines in the range 12–62kλ. The observations together with the molecular line data are described in more detail in Launhardt *et al.* (2009). CB 26 was also observed with the Owens Valley Radio Observatory (OVRO) between January 2000 and December 2001. Four configurations of the six 10.4m antennas provided baselines in the range 6–180kλ at 2.7mm (110GHz) and 12–400kλ at 1.3mm (232GHz). Effective synthesised beam sizes of all interferometric millimetre continuum images used here are summarised in Table 3.1.

The interferometric millimetre continuum images at 1.1mm, 1.3mm, and 2.7mm, together with the dirty beam images (see also Table 3.1), are shown in Figure 3.2. For the ease of modelling, these images have been rotated 30° in order to align the major axis of the elongated structure with the horizontal axis. While the source is unresolved vertically in all images, it is well-resolved along its horizontal axis, especially in the highest-resolution image at 1.3mm. The 1.3mm image also recovers some extended emission from the envelope that might be related to a disc wind Launhardt & Sargent (2001). For all images shown, radio and NIR, North is the same direction.

Figure 2.3 shows an overlay of a NIR colour-composite image and the 1.3 mm dust continuum emission. The spatial co-location of the millimetre dust emission and the

---

[1] Group for Edge-On Disc Exploration

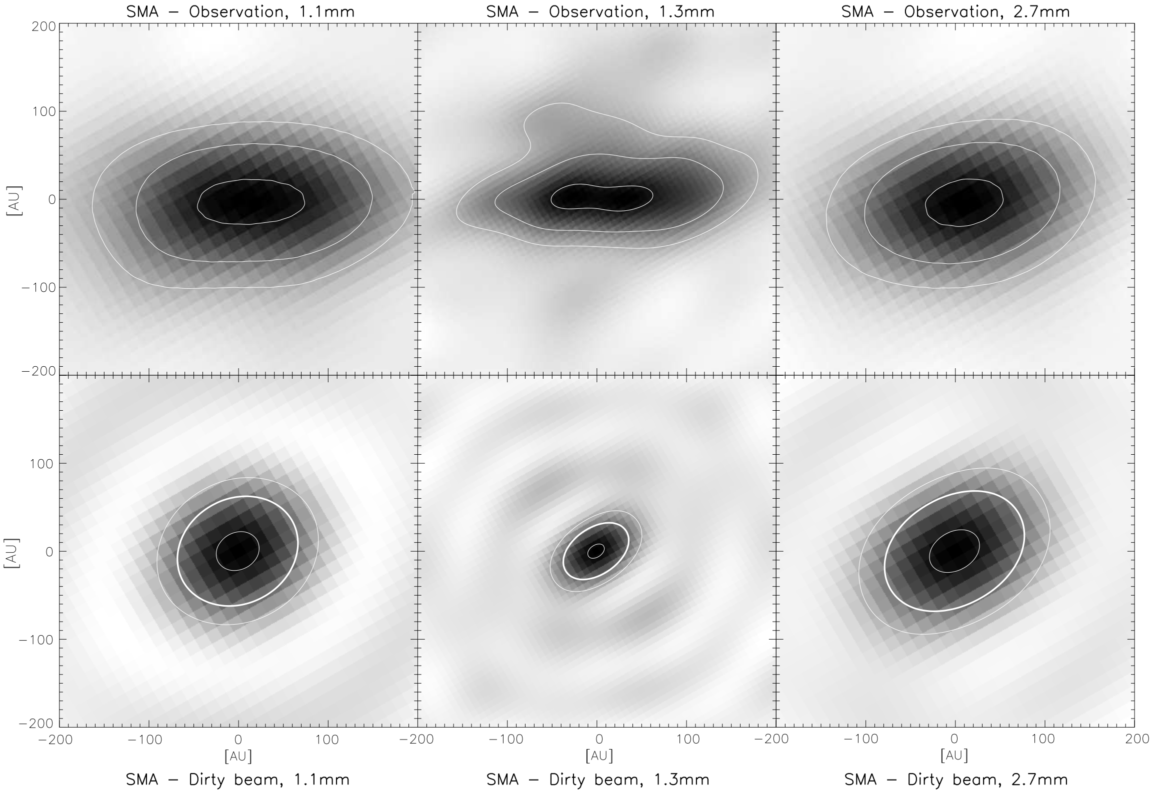

Figure 3.2.: Inverse, reconstructed images from millimetre interferometric observations (*upper row*) and corresponding dirty beam images (*lower row*), linear colour scale. All images have been rotated by −30° in order to align the major axis of the brightness distribution with the horizontal axis. For the image scale a distance to the object of 140pc is assumed ($100\,\mathrm{AU} = 0.7''$). The contour lines are drawn at (from inside out) 90%, 50%, and 25% of the image maximum flux value. In the dirty beam images, the 50% contour, marking the FWHM of the Gaussian clean beam, is marked bold.

dark lane in the scattered light images confirms the hypothesis of an edge-on optically thick disc as explanation for the observed features. However, the HST pointing is only good to about 1 arcsec. Due to the high extinction in the cloud core and the small NICMOS field of view, there are no reference stars in the image that could be used to correct for this pointing uncertainty.

Table 3.1.: Overview of the beam sizes in the millimetre-images of CB 26

Instrument	λ[mm]	PSF (FWHM) [″]	Orientation
SMA	1.1	1.00×0.84	$-59.3°$
OVRO	1.3	0.61×0.36	$-53.8°$
OVRO	2.7	1.21×0.87	$-58.3°$

3.2.4. Spectral energy distribution

The results of photometric measurements are presented in Table 3.2 and Figure3.3. The spectrum was obtained from the IRS compliments the photometric points as seen in Figure 3.3.

Submillimetre observations of CB 26 at 350 μm were obtained with the Submillimeter High Angular Resolution Camera II (SHARC-II) at the Caltech Submillimeter Observatory (CSO) on 2007 October 21. A flux density at 350 μm for CB 26 of 2.8 ± 0.6 Jy was measured. As is evident in this Figure, the 350 μm SHARC-II flux density is lower than expected based on comparison to the complete SED. This issue will be explored in more detail by M. Dunham et al. (2011, in preparation), but preliminary results suggest that flux densities measured from this particular observing mode may underestimate the true flux density by up to a factor of 2, even for relatively compact objects.

3.3. The model and its parameter space

3.3.1. The model

The model to interpret the presented observational data is a parametric disc as introduced in Section 2.1 and defined by equations 2.2 and 2.3. A sketch showing all components of the model is shown in Figure 3.4.

The employment of the disc is readily called for by the data. As it turns out, a further component in addition to the disc is needed. In order to reproduce the pattern of scattered light seen in the I, J, H, and K observations, an envelope-like dust distribution is added to the model. While the envelope has a high enough density to produce scattered light, it is orders of magnitude lower than the density of the circumstellar disc which is optically thick enough to obscure the central star completely as the HST optical and NIR data show. Further evidence for the low density in the envelope are the millimetre images where the envelope cannot be seen.

For the model of the envelope structure the idea of Ulrich (1976) is followed. These comprise a rotating envelope resulting from infalling matter similar to Whitney *et al.*

$\lambda[\mu\text{m}]$	Flux [mJy]	Aperture [″]	Instrument	Reference
0.90	0.062 ± 0.019	24	CAHA 3.5m	(1)
1.25	2.2 ± 0.2	12	CAHA 3.5m	(1)
1.65	8.2 ± 0.8	12	CAHA 3.5m	(1)
2.20	17.1 ± 1.7	12	CAHA 3.5m	(1)
3.6	18.3 ± 0.8	12	Spitzer IRAC1	(2)
4.5	17.0 ± 0.8	12	Spitzer IRAC2	(2)
5.8	12.5 ± 0.7	12	Spitzer IRAC3	(2)
8.0	6.8 ± 0.5	12	Spitzer IRAC4	(2)
24	160.6 ± 5.2	30	Spitzer MIPS1	(2)
60	4880 ± 390.4	75	IRAS PSC	(2)
70	5555 ± 52	120	Spitzer MIPS2	(2)
100	11100 ± 1110	125	IRAS PSC	(2)
160	10731 ± 69.49	24	Spitzer MIPS3	(2)
350	2650 ± 850	20	CSO	(2)
450	6700 ± 1300	54	SCUBA	(3)
850	600 ± 120	54	SCUBA	(3)
1110	225 ± 45	10	SMA	(3)
1270	240 ± 20	54	IRAM 30m	(3)
1300	190 ± 30	10	OVRO	(4)
2700	20 ± 2	10	OVRO	(4)

Table 3.2.: Photometric data points for CB 26. References: (1) Stecklum *et al.* (2004); (2) Sauter *et al.* (2009); (3) Launhardt *et al.* (2009); (4) Launhardt & Sargent (2001)

(2003); Eisner *et al.* (2005):

$$\rho_{\text{env}} = \frac{\dot{M}}{8\pi\sqrt{Gm_* r^3}} \left(1 + \frac{\mu}{\mu_0}\right)^{-\frac{1}{2}} \left(\frac{1}{2}\frac{\mu}{\mu_0} + \frac{r_{\text{cf}}}{r}\mu_0^2\right)^{-1} . \tag{3.1}$$

Here $\dot{M}$ is the dust infall rate, m_* the stellar mass, r_{cf} the centrifugal radius and $\mu = \cos\theta$. The initial infall path of dust particles is given by μ_0 as $r \to \infty$. As this is the only occurrence of $\dot{M}$ and m_*, the factor $\dot{M}(8\pi\sqrt{Gm_* r^3})^{-1}$ in Equation 3.1 is merely a coupling constant that scales the mass of the envelope just as ρ_0 does in Equation 2.2. Hence, $\dot{M}(8\pi\sqrt{Gm_* r^3})^{-1} = \tilde{\rho}$ are used as a fitting parameter. To avoid introducing a constant like $\tilde{\rho}$ with no direct physical interpretation into the discussion later on, in this work m_* and $\dot{M}$ are referred to separately.

At a given spatial point the larger density distribution, disc or envelope, is always used:

$$\rho(\vec{r}) = \begin{cases} \rho_{\text{disc}}(\vec{r}) & : \quad \rho_{\text{disc}}(\vec{r}) \geq \rho_{\text{env}}(\vec{r}) \\ \rho_{\text{env}}(\vec{r}) & : \quad \rho_{\text{disc}}(\vec{r}) < \rho_{\text{env}}(\vec{r}) \end{cases} . \tag{3.2}$$

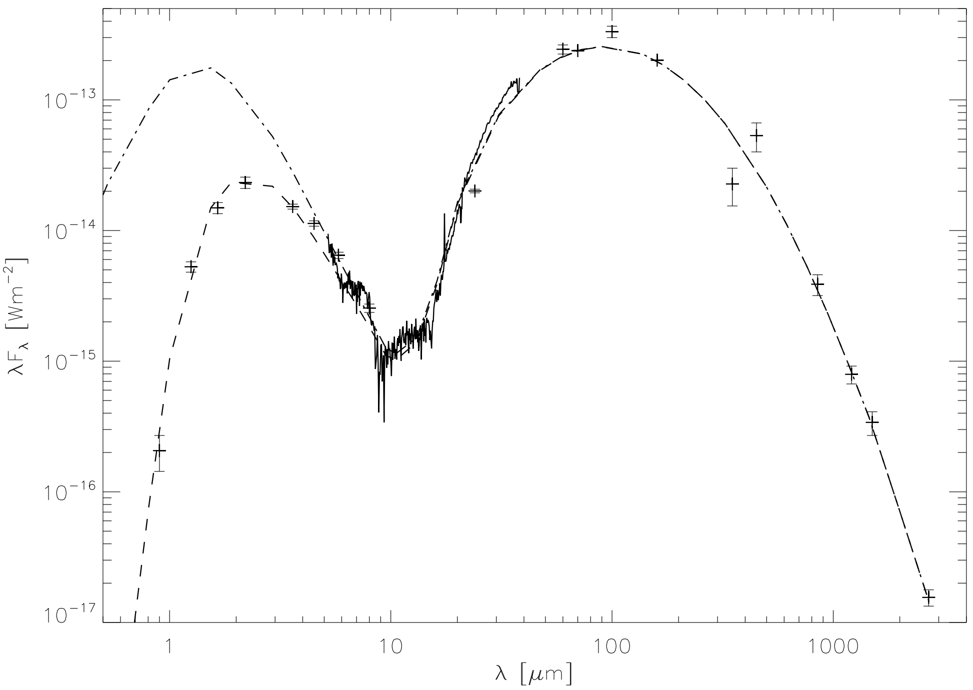

Figure 3.3.: Spectral energy distribution. Data with error-bars from Table 3.2. The IRS spectrum is the solid line. The dashed-dotted line corresponds to the best-fit model. The dashed line is the best-fit model with the dust screen.

In this manner, the disc is embedded into the envelope and a continous transition from the disc to the envelope is guaranteed. For the radius of the complete model space twice the outer radius of the disc is taken. The dust building up the density distribution in disc and envelope has the properties as described in Section 2.2.

The central star is the only primary source of energy in the setup. Its radiation heats the dust which then in turn itself re-emits at longer wavelengths. In this sense the disc in the model is passive and accretion or turbulent processes are neglected within the disc as a possible other primary energy source. Yet, the model involves a parameter with the dimensionality of an "accretion rate": $\dot{M}$ in Equation (3.1) as part of the description of the envelope structure. However, this quantity is really an infall rate within the envelope and may not necessarily describe mass accretion onto the star itself. But it is in general the latter mass flow that, as e.g. in FU Orionis like objects, accounts for significant contributions to the system's luminosity. For a T Tauri like system as CB 26, accretion is neglected as a major source of energy. For CB 26, $\dot{M}$ turns out to be rather small, around $\sim 10^{-8}\,\mathrm{M}_\odot\,\mathrm{yr}^{-1}$. This is small compared to FU Orionis objects but average for T Tauri Stars and strongly supports

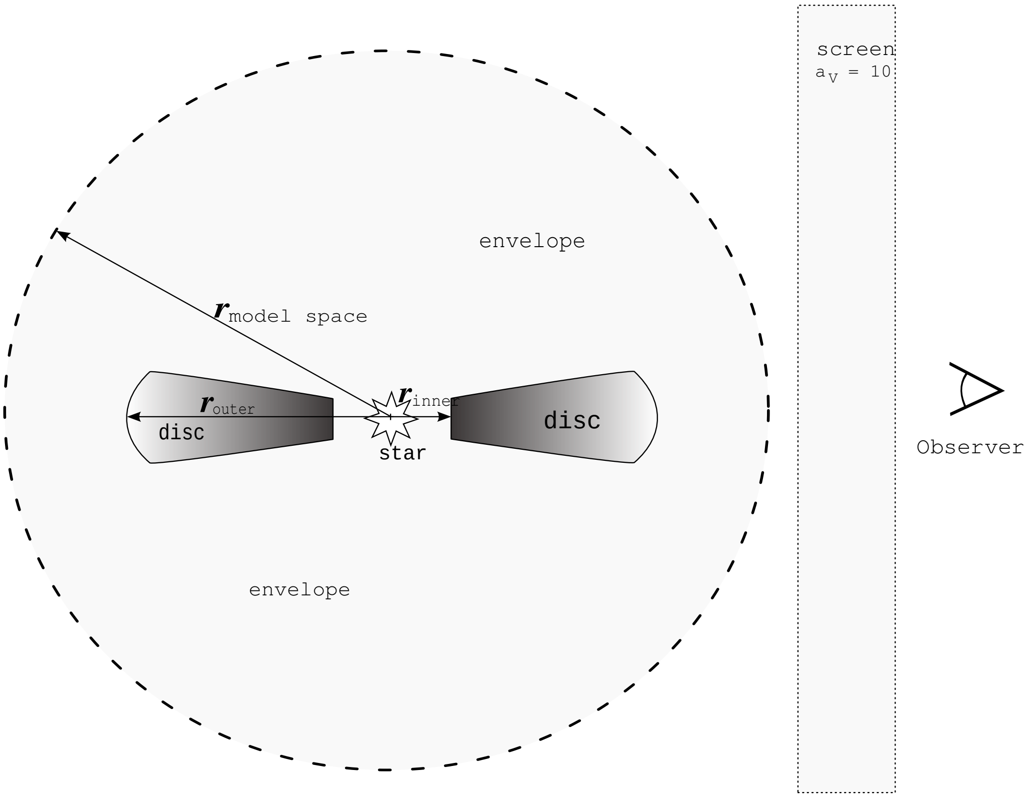

Figure 3.4.: Sketch showing all components of the model and their spatial arrangement. All sizes are not to scale.

the passive ansatz. As the central star is not directly visible, stellar parameters (i.e., temperature and luminosity) have to be assessed and the parameters of the 'typical T Tauri star' as introduced in Section 2.1 are used. Its parameters are kept fixed in the parameter study to avoid degeneracies between parameters of the model. Except for the total flux, this choice has no impact on the near-infrared images.

3.3.2. Constraints from observations

Given the broad variety of available observational data, there are primary features that the model ought to reproduce. This also determines the criteria for the best-fit model. The case is simple for the spectral energy distribution, where the goal of the modelling is to fit all the data points. The issue is a little different for images and the discussion of the reason is the is subject of Section 2.5.

The morphology of the millimetre images has its origin in the dust that is heated by the star and re-emits light at those wavelengths. Although the images at 1.1 mm, 1.3 mm and 2.7 mm are rather simply structured they impose two major features that constrain the model. These are

1. The peak flux and
2. The spatial brightness distribution.

Since in all three images the beam size is larger or comparable to the vertical extent of the disc, one cannot constrain the flux distribution on the z–axis, perpendicular to the disc midplane. Any feature there is smoothed out by the beam. Therefore, the modelling focuses on reproducing the flux distribution along the midplane of the disc.

The four images in the near-infrared show more structures and details than the millimetre images. In addition to the disc, which appears as a dark lane in the near-infrared, there is also a complex, wavelength-dependent morphology of the surrounding envelope. Considering that the circumstellar disc CB 26 is located at the edge of a Bok globule, one realises that the environment of the disc can account for the majority of the substructure seen on these images; yet the Bok Globule itself is not part of the model. Hence, the modelling is restricted to the following two points:

1. The dependence of the width of the dark dust lane on wavelength and
2. The relative peak height of the brightness distribution above and below the dust lane.

Also, no emphasis is put on the vertical width of the upper and lower lobe nor on the exact morphology.

3.3.3. Quality of the fit

For each comparison between model and observation on the aforesaid points, an individual χ_i^2 is computed. The total χ^2 of one model is then just the sum over all the individual χ^2s:

$$\chi^2_{\mathrm{total}} = \frac{1}{n}\left(\chi^2_{\mathrm{SED}} + \sum_{\mathrm{mm-maps}} \chi_i^2 + \sum_{\mathrm{NIR-maps}} \chi_j^2\right) \tag{3.3}$$

Here, $n = 8$ as there are one χ^2 from the SED, three from the millimetre images, and four from the scattered light images.

Based on χ^2_{total} from Equation (3.3), the modelling errors are given as the range where the the parameter values can be altered without changing χ^2_{total} more than 10%, which has proven to reflect quite well the adjustability of the model. Allowing for a larger variation of χ^2_{total} than 10% gives generally worse results.

3.3.4. Parameter space study

Based on the model laid out in the previous sections, there are ten adjustable parameters to reproduce the characteristics as described in the previous section. If not stated otherwise, their range is chosen similar to the modelling of other comparable objects (Wolf *et al.*, 2003). First, the range of an individual parameter is sampled in four coarse steps. Then the two best values are selected, and the same procedure is applied to the next parameter. Secondly, the results are taken as an indicator how to refine the stepping in a smaller range. This process is iterated to reach final results.

In detail, the parameters and their respective ranges are:

1. The exponents α and β which describe the radial density profile of the disc (see Equation (2.2 and 2.3 for details). From D'Alessio *et al.* (1999b), the flaring parameter $\beta = 1.25$ is chosen and a corresponding value for $\alpha = 2.25$ is obtained (cf. Equation (2.4)). Beyond those values in steps of 0.1 and 0.2 are chosen, respectively.

2. The scale height h_0 of the disc at 100 AU. Considered vales are $h_0 = 5\,\mathrm{AU}$, 10 AU, 15 AU, 20 AU, and 25 AU.

3. The density Equation (3.1) of the envelope, gives centrifugal radius r_{cf} and the coupling constant $\tilde{\rho}$ which is a function of the mass accretion rate $\dot{M}$ and the mass of the central star m_*. For the centrifugal radius, values in the range $100\,\mathrm{AU} \leq r_{\mathrm{cf}} \leq 800\,\mathrm{AU}$ are probed. As for $\tilde{\rho}$, vales for the accretion rate are chosen from the interval $\dot{M} \in [10^{-5}\,\mathrm{M}_\odot\mathrm{yr}^{-1}; 10^{-10}\,\mathrm{M}_\odot\mathrm{yr}^{-1}]$. $\tilde{\rho}$ is then computed under the consideration of the stellar mass by Launhardt *et al.* (2008). In this paper a dynamical mass of $m_* = 0.5 \pm 0.1\,\mathrm{M}_\odot$ is derived.

4. The inner and outer disc radius. The inner radius was initially set to 0.1 AU, which is approximately the dust sublimation radius. However, no good agreement especially with the 1.3 mm image was obtained unless larger values of $\sim 45\,\mathrm{AU}$ were allowed. For the outer radius r_{out}, a value of 200 AU has been chosen, but also configurations with 150 AU and 250 AU were tested. r_{out} is mainly determined by the size of the elongated structure in the millimetre images. Hughes *et al.* (2008) argues that the millimetre continuum may not be as good as CO line emission to trace the disc extent. However, in the case of CB 26, the extent of the dark lane is also consistent with the outer radius obtained.

5. The disc mass. Seven different disc dust masses in the range from $1.0 \times 10^{-5}\,\mathrm{M}_\odot$ up to $4.5 \times 10^{-3}\,\mathrm{M}_\odot$ are considered.

6. The system is seen almost edge-on. Consequently, the range for θ in the parameter space is restricted to values between 60° and 90° with a step size of 1° between 80° and 90°.

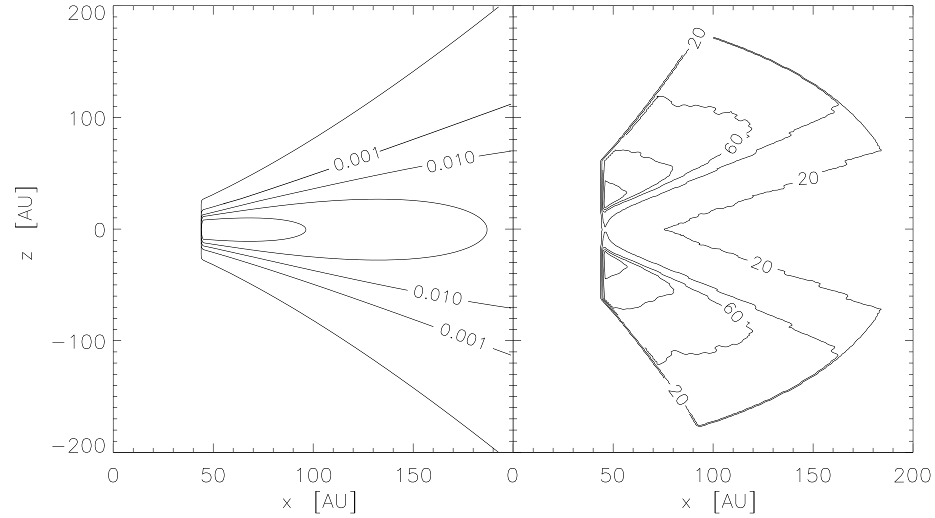

Figure 3.5.: *Left plot:* Contours of dust density distribution on a plane perpendicular to the midplane normalised to the peak density of $0.34 \times 10^{-8}\,\mathrm{g\,cm^{-3}}$. The contour levels are at 10^{-7}, 10^{-3},10^{-2}, 5×10^{-2}, and 2×10^{-1}.
Right plot: Contours of the temperature distribution on the same plane as above. Contour levels are at 20K, 40K, 60K, 70K, and 80K. The maximum temperature is 90K.

7. The maximum grain size $a_{\max}$. Grain growth is a major issue for protoplanetary discs as it is the first step towards the formation of planets from the dust in the interstellar medium. The maximum grain size considered is $a_{\max} = 1\,\mathrm{mm}$.

Table 3.3 summarises these ten adjustable parameters of the model and their ranges.

3.4. Results

The values of the parameters of the best-fit model can be found in Table 3.3. The geometrical parameters α and β of the disc density structure yield with the Equation (2.6) a surface density power-law exponent of $p = -0.8$. In Figure 3.5 the density and temperature distributions of the best-fit model are shown while in Figure 3.6 radial profiles of the density and temperature distribution in the midplane and 20 AU above are plotted. It is apparent that the high density in the midplane on the inner rim provides enough opacity so that material behind it is shielded from the stellar radiation. The highest dust temperature at the inner disc rim amounts to $\approx$ 90K and is reached $\sim$ 20 AU above the midplane. However, due to the high density in the midplane, the stellar radiation does not penetrate deep into the midplane which

Parameter	Minimum value	Maximum value	Best fit value	Uncertainty
α	2.0	5.0	2.2	± 0.1
β	1.0	2.6	1.4	± 0.1
h_0[AU]	5	25	10	± 2.5
r_{in} [AU]	0.1	60	45	± 5
r_{out} [AU]	150	350	200	± 25
m_{dust} [$\mathrm{M}_\odot$]	1.0×10^{-5}	5.0×10^{-3}	3.0×10^{-3}	$\pm 0.2 \times 10^{-3}$
$\dot{M}$[$\mathrm{M}_\odot \mathrm{yr}^{-1}$]	10^{-10}	10^{-5}	10^{-8}	$\pm 0.5 \times 10^{-8}$
r_{cf}[AU]	100	800	460	± 10
a_{max} [μm]	0.25	1000	2.5	± 0.3
θ	60°	90°	85°	±5°

Table 3.3.: Overview of parameter ranges and best-fit values. For the definition of the uncertainty see section 3.2.3. The first group of parameters contains purely geometric parameters, the second group physical parameters and the last group the inclination of the disc as seen by the observer as an observational parameter.

results in a steep temperature gradient. In the less dense layers above and below the midplane of the disc, the stellar radiation also heats more distant parts of the disc resulting in a less steep temperature gradient.

An average dust temperature of $\bar{T}_{\text{dust}} = 16\,\mathrm{K}$ is obtained from the temperature distribution by weighting it with the mass distribution. This is in good agreement with Figure 3.5. High temperatures are only reached in a very narrow region at the inner disc rim and in the very low density regions of the disc and, thus, contributes little to the mass averaged dust temperature.

Since the dust grain model only uses refractive indices (cf. Section 2.2), an effective dust grain opacity can be calculated by re-arranging

$$m_{\text{dust}} = \frac{S_\nu D^2}{\kappa_\nu B_\nu(\bar{T}_{\text{dust}})}. \tag{3.4}$$

Here, κ_ν is the wavelength dependent mass absorption coefficient, S_ν is the observed flux, D the distance of the object, and $B_\nu(\bar{T}_{\text{dust}})$ is the Planck-function at a given temperature. The calculation yields for the best-fit model a dust opacity of $\kappa_{1.3\,\mathrm{mm}} = 0.26\,\mathrm{cm}^2\mathrm{g}^{-1}$. This value is very close to the ISM dust opacity given by Draine & Lee (1984, 1987). Compared to opacities for coagulated dust grains and ice-coated grains (Ossenkopf & Henning, 1994; Beckwith *et al.*, 1990), the model yields an effective dust grain opacity at the lower end of the range of commonly employed opacities.

Figure 3.3 shows the spectral energy distribution of the best-fit model in comparison with the spectral data. A good match is achieved to the observational data except for the optical wavelengths. Since the circumstellar disc is embedded in the

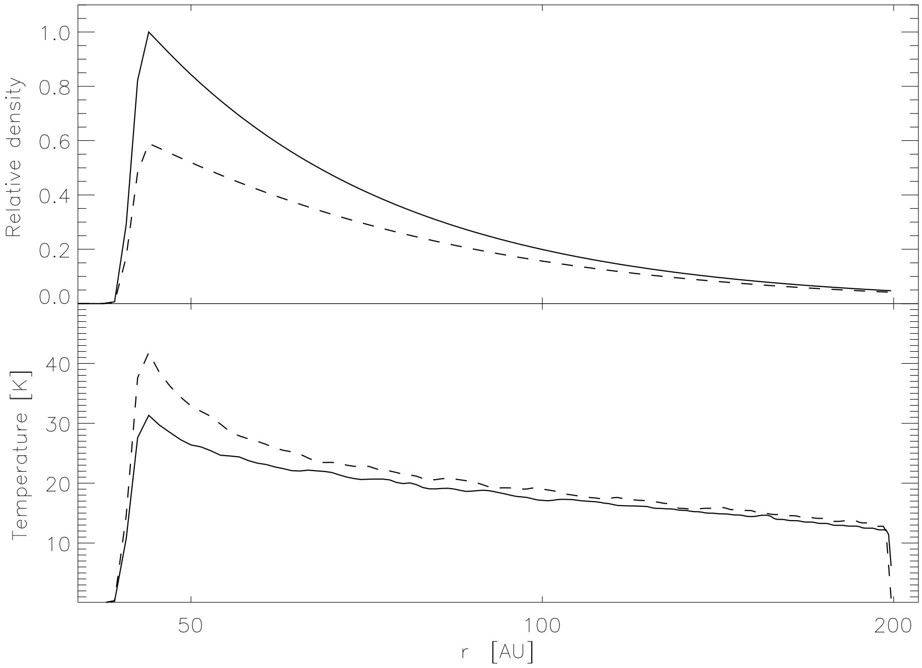

Figure 3.6.: Radial profiles of density (*upper plot*) and temperature (*lower plot*) in the midplane along r (*solid line*) and along $z/r = 0.1$ (*dashed line*). The latter profile is chosen in order to include the scale height h_0 at $r = 100\,\mathrm{AU}$. The maximum density is normalised to 1 (corresponding to $0.34 \times 10^{-8}\,\mathrm{g\,cm^{-3}}$).

Bok globule CB 26, one needs to consider the dust outside the model space as well. A screen is added that mimics the effect of foreground extinction between the object and the observer. For this screen, the extinction properties of interstellar dust grains are being assumed. Such a screen is described in detail by Cardelli *et al.* (1989). Using A_V as a parameter with a minimum value of 2, it turns out that a screen with a visual extinction of $A_\mathrm{V} = 10$ can easily account for the missing flux in the optical. The result is shown in Figure 3.3 as the dashed curve, whereas the dashed-dotted line corresponds to the best-fit model without the screen. It needs to be stressed that this screen only applies an extinction law to all observable quantities. It is not subject to any radiative transfer or thermal re-emission. The possible contribution to re-emitted radiation of such a screen with $A_\mathrm{V} = 10$ composed of ISM grains at the same distance as CB 26 with a temperature of 16K is estimated. The screen is found to be clearly optically thin (e.g. $\tau_{1.3\,\mathrm{mm}} = 8 \times 10^{-5}$) and has only enough mass to have about $\approx 1\%$ of the observed flux in the millimetre regime.

Furthermore, the spectral energy distribution of the model shows that the contribution of the envelope is quite important for shorter wavelengths. In this regime,

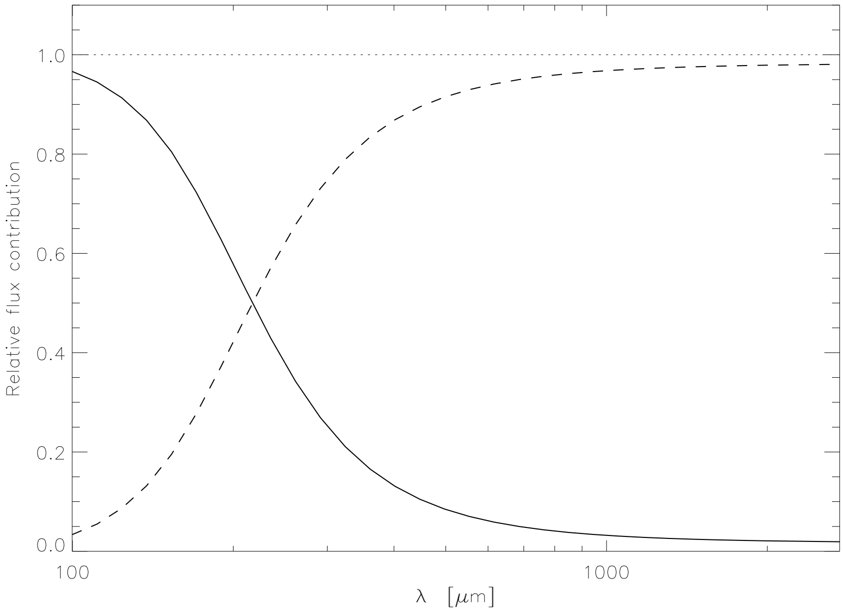

Figure 3.7.: Contributions to the spectral energy distribution from disc (dashed line) and envelope (solid line). The transition from envelope to disc as the major source of radiation (re-emission and scattering) is at $\lambda = 217\,\mu$m.

the main contribution to the spectral energy distribution comes from the envelope whilst in the radio regime the flux comes completely from the dust in the disc which glows at those wavelengths. Figure 3.7 illustrates this.

3.5. Discussion

3.5.1. Grain size and growth

The maximum grain size of the best fit model is $a_{\max} = 2.5\,\mu$m. While this is a factor ten larger than the smallest maximum grain size considered in the parameter space, the value found is only marginally larger then upper grain sizes given for the ISM in the literature. In fact, this is only true for the dust in the the disc component. The maximum grain size in the envelope is the same as found in the ISM, $a_{\max} = 0.25\,\mu$m. If the maximum grain size in the envelope is bigger, then the short wavelength part of the SED could not be reproduced.

The maximum grain size is certainly smaller by several orders of magnitude than the maximum grain size in other disc models such as in the work of Pinte *et al.* (2008). There, a maximum size of a few millimetres has been found. In contrast, models in the parameter space featuring values of $a_{\max} \approx 1\,\mathrm{mm}$ fail to fit the SED in the millimetre regime as the slope of the model SED is not steep enough. Also, the model does not succeed in reproducing the default value for the maximum grain size of $a_{\max} = 250\,\mathrm{nm}$ of ISM. In particular, the model would be off by a factor of ten for the SED data point at 1.3 mm.

Influence of the grain chemistry on Q_{abs}

One needs to discuss why the change for $a_{\max}$ from 250 nm to $2.5\,\mu\mathrm{m}$ allows for a fit in the *millimetre* part of the SED – at wavelengths three orders of magnitude larger than the largest grains in the model. Intuitively, one would expect the millimetre part of the SED to remain unaltered by a change of grain size at that level. However, this expectation is based on the assumption that the absorption efficiency of the grains Q_{abs} in the millimetre regime is also insensitive to a change in the grain size at the micrometre level. Yet, this only holds true for two of the three dust species in the model. For the astronomical silicate and the graphite component with an alignment of the crystals' optical axis perpendicular to the propagation direction of the electromagnetic field Q_{abs} has the same slope in the millimetre regime for grain size distributions with a maximum grain size of 250 nm and $2.5\,\mu\mathrm{m}$. But for the third dust species, namely the graphite component with the crystals' optical axis aligned with the electromagnetic field, this is different. Here, the slope of Q_{abs} is significantly larger for $a_{\max} = 250\,\mathrm{nm}$ than for $a_{\max} = 2.5\,\mu\mathrm{m}$. This effect is large enough to dominate the sensitivity of the SED to changes in the maximum grain size even at the level discussed despite the fact that the dust species responsible for this behaviour has only a 12.5% share of the total dust. Figure 2.1 gives an impression of the dependency of Q_{abs} on $a_{\max}$. This is due to the fact that graphite is a far more effective absorber than silicate.

The opacity slope β_{mm}

A look on the millimetre spectral index of the data yields $\alpha_{\mathrm{mm}} = 3.1 \pm .27$. The corresponding millimetre opacity slope is $\beta_{\mathrm{mm}} = 1.1 \pm .27$, if the millimetre emission is assumed to be optically thin. A $\beta_{\mathrm{mm}} = 1$ and smaller is understood to indicate that dust grain particles larger than in the interstellar medium are present. A value of $\beta_{\mathrm{mm}} = 2$ is expected if only ISM grains were present in the disc (cf. also Section 2.3). The latter is true only for grains whose absorption efficiency Q_{abs} behaves like silicate. The value of β_{mm} obtained from data and model of CB 26 is close to what is expected for large grains despite having still only micrometre sized grains in the model. This is due to the unorthodox behaviour of the parallel graphite component on the one hand side and on the other hand side to the non-vanishing optical depth in the millimetre regime (e.g. $\tau_{1.3\,\mathrm{mm}} \sim 0.6$).

Draine (2006) also considered the behaviour of the millimetre opacity slope β_{mm} for dust mixtures of graphite and silicate. There, no dependency of the opacity index as in the model for CB 26 was found. However, in this analysis crystalline graphite was not used but rather the optical properties of amorphous carbonaceous solids.

As a result, mm sized grains are not needed to model the circumstellar disc CB 26 but grains with a maximum grain size still close to what is found in the ISM. This is in contrast to the modelling of the Butterfly star (Wolf *et al.*, 2003) as well as for the circumstellar disc HH 30 (Wood *et al.*, 2002) where in both cases the authors found it necessary to have their largest grains at least four times larger than the largest grain of the interstellar matter. Of course, this result is based directly on the choice of the grain model. For another model, especially one without graphite, larger grains might be needed to fit the observed SED (e.g. Pinte *et al.*, 2008). Yet, due to the poorly constrained dust composition of circumstellar discs – in particular in the disc interior – this degeneracy between dust model and grain size must remain. As the dust model used in this work is also used in the context of other studies of circumstellar discs such as the Butterfly star Wolf *et al.* (2003), it is a reasonable choice as it keeps the models of similar objects comparable as they are built on common assumptions.

3.5.2. Inner hole

A quite unexpected result of the model is the inner disc radius for the model. In Figure 3.8 the solid line shows the flux profile along the disc midplane at 1.3 mm as seen by OVRO whilst the thin solid line is the PSF of the observation. At the centre of the disc, the profile shows a plateau in the brightness distribution. There are two possible explanations for this dip.

Too much mass and too little

First, the minimum could indicate that emitting dust in that region is present but not visible. If the optical depth in the midplane is sufficiently high, the flux contribution from the inner parts of the disc compared to the contribution of the optically thin parts on the disc's surface would be smaller.

A high optical depth can easily be reached in regions of high dust densities. For a given total disc mass, a disc with small inner radius yields higher densities than the model with the large inner radius. Hence, the smaller the inner radius in the model, the more matter is found to be close to the star and thus reaching higher optical depths in the inner disc regions. However, even for the smallest inner radius in parameter space, 0.1 AU, no optical depth is reached such that enough flux from the disc centre is obscured. This behaviour would also be more obvious when compared with images at shorter wavelengths since the optical depth increases with decreasing wavelength. But in the images at 1.1 mm and 2.7 mm no dip at the centre of the disc is seen. Unfortunately, it is not possible with the other available images to conclude

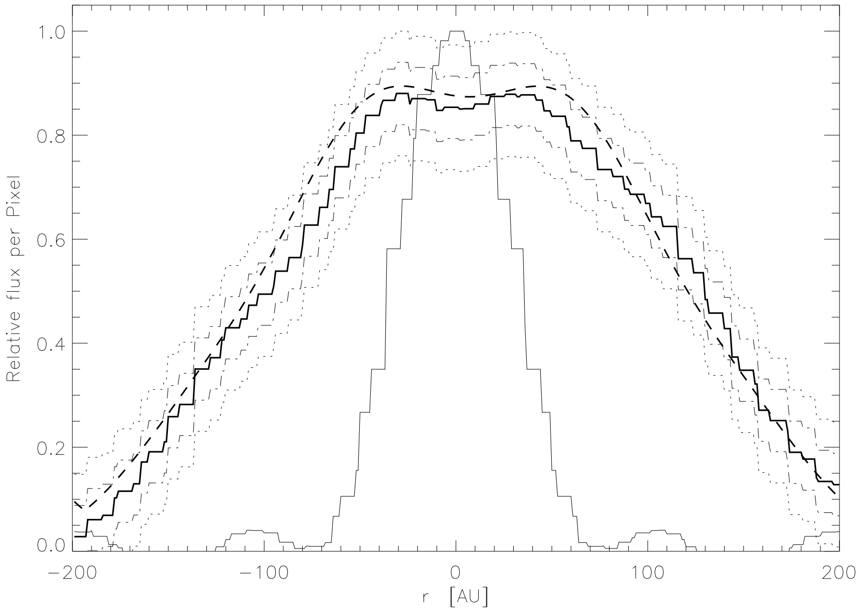

Figure 3.8.: Horizontal cut through the spatial brightness distribution at 1.3 mm. The thick solid line represents the OVRO observation, the dash-dotted lines gives the addition/subtraction of one σ, the dotted line indicates the 2σ-levels, the dashed line corresponds to the best-fit model, and the thin solid is the dirty beam of the observation.

whether the absence of the dip is really an indicator for a substantial void in the disc. This is because the point spread function at those two images is far too large to resolve the feature (see Table 3.1). Wolf *et al.* (2008a) reasoned this way in the case of IRAS 04302+2247 where they found a similar dip in the brightness distribution at $\lambda = 894\,\mu$m but not at 1.3 mm.

The second possible cause for the spatial brightness distribution in the 1.3 mm image is the actual lack of dust in the inner region of the disc. The parameter space study started with an inner radius on the order of magnitude of a few tens of the stellar radius. Yet, it was not possible to match the plateau structure of the 1.3 mm image. Consequently, larger inner disc radii have been considered up to 50 AU. Unfortunately, within the model and parameter framework one is not at liberty to increase the total mass, and hence the density at the disc centre, because the flux at 2.7 mm already sets an upper limit for the total disc dust mass. This is because at this wavelength any model is sufficiently optically thin and the total matter of the disc can be seen.

Optical depth and inner radius

Another way to think about the issue is to consider the optical depth of the disc at 1.3 mm. The optical depth in the midplane from the star to the observer of the best-fit model is $\tau_{1.3\,\mathrm{mm}} = 0.6$. For a model with an inner radius of $r_{\mathrm{in}} = 0.1\,\mathrm{AU}$ but all other parameters left unaltered, the optical depth is $\tau_{1.3\,\mathrm{mm}} = 1.9$. In the first case the system is an optically thin system, while in the second case, the optical depth is borderline. An optical depth of 1.9 means that the initial flux is reduced by a factor of $e^{-1.9} = 0.15$. A much larger value of τ along the line of sight would be required to hide all emitting dust in the central region and produce the observed plateau structure. Consequently, it is not possible to fit the millimetre profile with a small inner radius.

Therefore, in the millimetre regime the entire disc is seen. Hence, the plateau structure rises from the wide spatial separation of the inner rim from the star, whereas a disc with a small inner radius would have a central peak in the brightness distribution.

Based on this line of arguments, the model provides predictive power for high resolution images at wavelengths longer than 1.3 mm. Since the plateau structure in the brightness profile is due to lack of dust, it should also be visible at longer wavelengths. There, the dust becomes more optically thin. Now, if the lack of flux in the disc centre is due to an optical depth effect, the central trough should vanish with longer wavelengths, and the brightness profile should have one central peak instead of a plateau-structure. Unfortunately, the image at 2.7 mm has a point spread function far too large to allow use it to disentangle between the two possibilities. Future observations of the disc CB 26 with higher spatial resolution will provide a perfect opportunity to confirm this prediction. Figure 3.9 shows what the model is expected to look like at different wavelengths according to the model with the inner void. With the Atacama Large Millimeter Array (ALMA) it will be quite easy to confirm the model. It needs to be pointed out that the spectral energy distribution of CB 26 does not hint at the presence of a large inner hole. Its general shape is similar to SEDs of other edge-on discs. This is because the inner regions of the disc which completely dominate the disc emission in the 1-20 micron regime are completely hidden from view in the edge-on configuration. Scattered starlight from the outer disc and/or the envelope accounts for the short wavelength bump of the SED, irrespective of the amount of emission from the disc itself. Only the quality of the OVRO image at 1.3mm requires one to postulate about an inner clearing.

A possible explanation for a large void with 90 AU in diameter is that the disc in the Bok globule CB 26 is actually a circumbinary disc. Binarity is also a possible explanation for the rotating molecular outflow described by Launhardt *et al.* (2008). However, a detailed dynamical study is not the scope of this paper.

Of course, another idea might be that the dust in the inner region has already been processed to planetesimals, or at least to bodies that are large enough to decouple from the disc and its dynamics, and do not contribute to the mm-flux. However, a

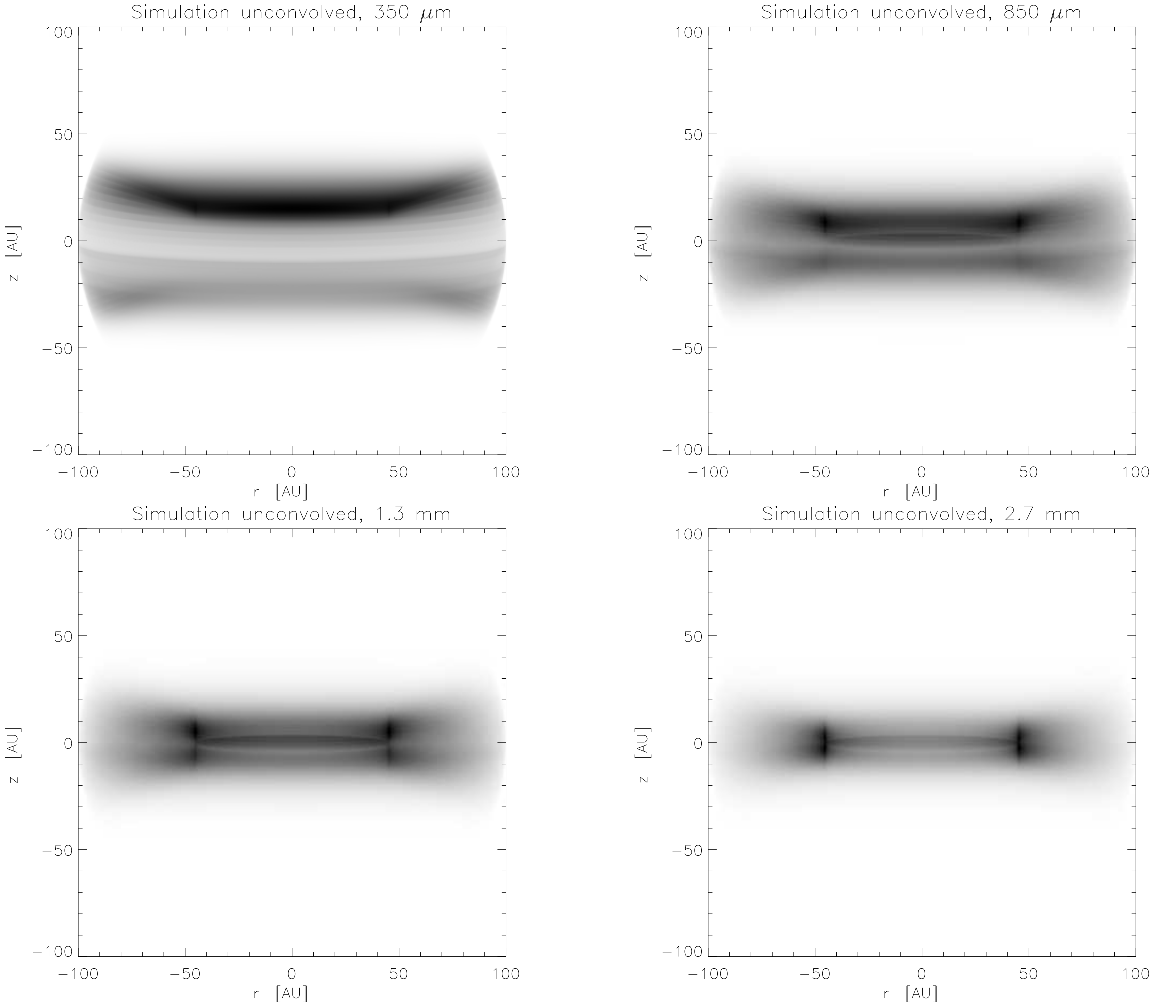

Figure 3.9.: Predicted appearance of the inner region of the disc.

first indicator for a low age of the system is the fact that it is still deeply embedded in its parental cloud. Another indication to the young age of the system is the absence of dust grains larger than are found in the interstellar medium. Hence, it is not to be expected that CB 26 is a so-called “transitional disc”[2] and a planet population in the centre that has already cleaned up formerly dusty regions.

3.5.3. Disc mass

The model features a rather high disc mass to account for the observed flux in the millimetre regime. A total of about $3 \times 10^{-3}\,\mathrm{M}_\odot$ and dust-to-gas ratio of 100 yields a total disc mass of $\sim 0.3\,\mathrm{M}_\odot$ which is close to the star’s mass. The derived disc mass

---

[2] Those discs are considered to be predecessors of evolved debris-type discs.

essentially builds upon the assumptions made about the dust grain chemistry and shape.

Dust grain structure, temperature and density

The radiative transfer calculations are performed under the assumption of spherical dust grains to avoid equivocalities. It would be possible to have a lower estimate of the dust mass if this assumption is moot. This very much complicates the radiative transfer calculations since now all possible fractal grain shapes as well as the spatial orientation of every grain has to be taken into account. So far, such computations are beyond numerical possibilities. But, a thought experiment can be made on behalf of the results. Of course, one expects strong changes in the scattering behaviour of dust grains with complex shapes. But, besides that, one also can think of a plenitude of dust grains with almost the same absorption cross section as spherical dust grains but with much less mass. Voshchinnikov *et al.* (2007) discusses very fluffy particles with a porosity up to 90%.

It furthermore needs to be pointed out, that the grain density ρ_{grain} is not one of the fitting parameters. The disc mass is proportional to this density and the number of grains. Within this framework, it is only possible to constrain the disc structure, the grain size, and their number, but not the density of one grain, which is taken to be $\rho_{\text{grain}} = 2.5\,\text{g}\,\text{cm}^{-3}$, but it might well be less than this value. In turn, this will alter the estimate for the disc mass by the very same factor.

The snow line

The canonical relation (2.13) is used to estimation the total disc mass of gas and dust. This relation assumes that there is some gas and dust of the disc inside the snow line and some outside. The snow line indicates the largest radius for which the temperature in the disc is high enough to keep water from freezing onto the dust grains. This line is usually set at a radius where the disc temperature drops to 170 K and is typically located at a few AU. Yet, the maximum temperature reached within the disc is about 90 K, and the average is only 16 K. This means that the entire disc is outside the snow line. Thus, one needs to adjust the dust to gas ratio (2.13) to about 50 as published by Kokubo & Ida (2002).

However, the very same dust model made use of in this work was also built upon in other modelling projects (Wolf *et al.*, 2003). In order to allow comparison of the model presented for CB 26 with those models, some consideration of the disc stability is in order, if the dust model is to be kept.

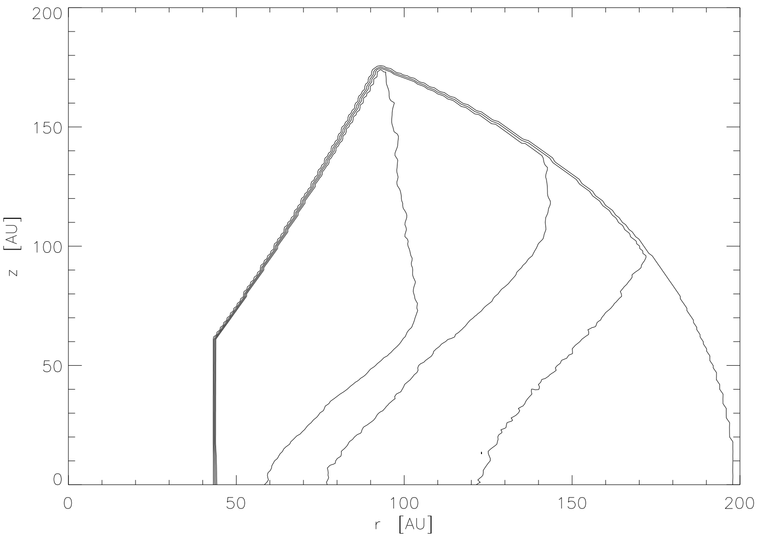

Figure 3.10.: Contour lines of the Toomre parameter Q (see Equation 3.5). The lines, from right to left, are at levels of $Q = 0.1$, 0.3, 0.5, 0.7.

Stability, binarity and dynamics

A criterion for a disc to become unstable was first shown by Toomre (1964). In order to allow self-gravity of the disc to take over, it must satisfy

$$Q = \frac{c_\mathrm{s}\varkappa}{\pi G \Sigma} \simeq 1 \tag{3.5}$$

where c_s is the local sound speed, $\varkappa$ the angular frequency of the disc, G the gravitational constant and Σ the surface density. For values of Q smaller then unity, the disc is assumed to be gravitationally unstable whereas for Q larger than unity the disc is supposed to be stable against gravitational collapse. As Figure 3.10 clearly shows, the model exhibits $Q < 1$ throughout the entire disc by a factor of two to five.

Yet, the Toomre criterion can only be consistently employed for a system that is formed by a central star and a surrounding disc. As discussed above, the inner hole in CB 26 can be an indication for a binary. An example for such a system would be the young binary system GG Tau. Here, a dusty ring around the central stars has been observed by Guilloteau *et al.* (1999) with a total ring mass of $0.13\,\mathrm{M}_\odot$, which is about a factor of two smaller than the total mass of CB 26. The discussion of stability of a binary system is quite delicate and not the topic of the present paper.

However, if one assumes a single central star, there are still effects not considered in the model but which might be important for the system's stability. Following the discussion in the paper of Gammie (2001), discs violating the Toomre criterion are not stable but nevertheless might be in a steady gravoturbulent state. The

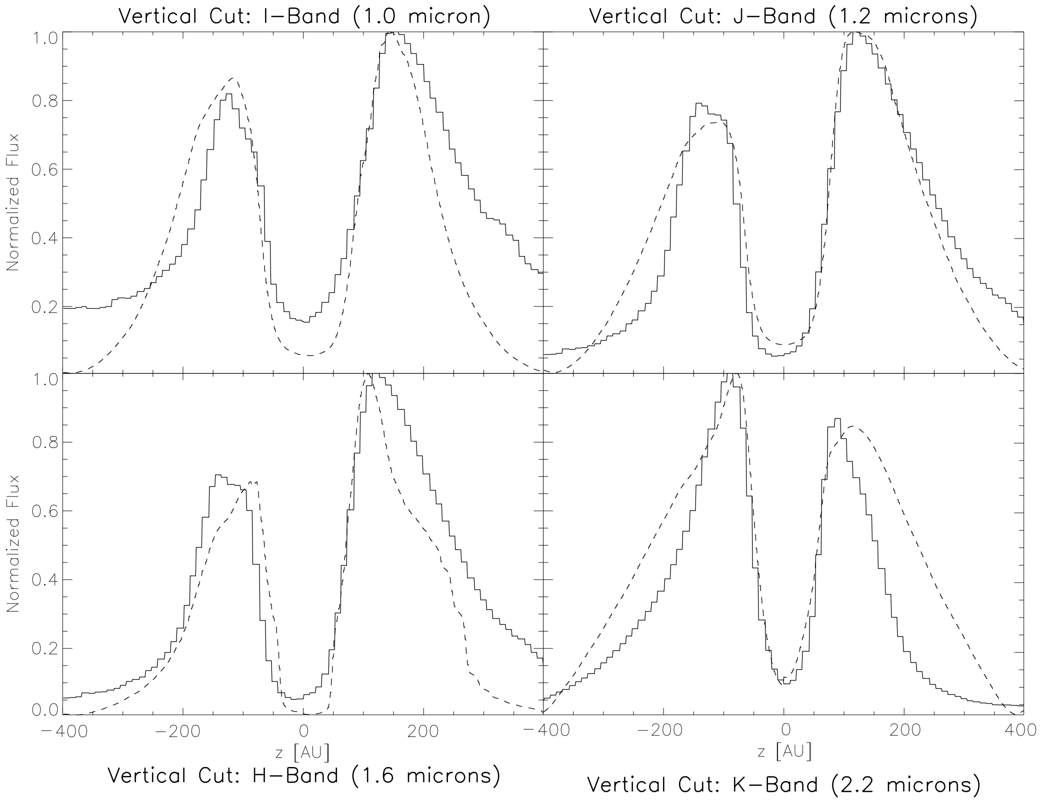

Figure 3.11.: Vertical cuts at the horizontal centre through the near-infrared scattered light images. The solid line is from observational data, and the dashed line is from the best-fit model. For an illustration where those cuts are obtained in the respective images, see Figure 3.12. The plots are normalised to 1. In case of the I-Band, this corresponds to 1.3×10^{-7} Jy/beam, 5×10^{-6} Jy/beam in the J-Band, 2×10^{-5} Jy/beam in the H-Band, and 2.2×10^{-4} Jy/beam ('beam' refers to the FWHM area of the PSF).

paper investigates gravitationally unstable thin Keplerian discs and concludes that the actual outcome of the instability depends on the cooling time.

However, the parametric model used does not account for any dynamical interaction within the dust. Therefore, it would be interesting to couple `MC3D` with hydrodynamic simulations of circumstellar discs in a future investigation.

3.5.4. The width of the dark lane & envelope structure

Another goal of the model is to mimic the chromaticity of the dust lane, which narrows with increasing wavelength. Figure 3.11 shows cuts from north to south through

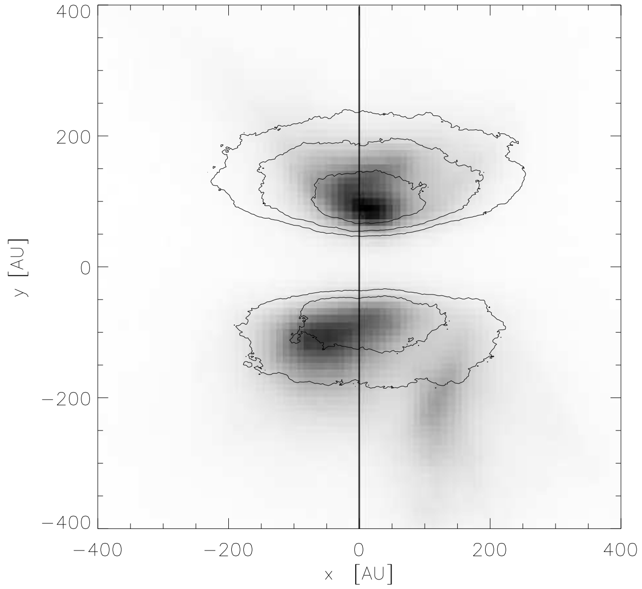

Figure 3.12.: Inverse H-Band image from HST/NICMOS. The contour lines are from the best-fit model. From the outer to the inner lines they are at 27%, 41%, 68% of the peak height. The second dark lane is not reproduced by the model as it does not account for envelope asymmetries. The PSF for those images is rather small $\sim 7\,\mathrm{AU}$ FWHM. The vertical line illustrates how the cuts were taken in Figure 3.11.

the centre of the NIR images from modelling and observations. The envelope model (Equation 3.1) is quite successful in reproducing the overall flux at each wavelength. Also, the wavelength-dependent width of the dark lane is correctly reproduced. Figure 3.12 shows an overlay of the HST/NICMOS H-band image with the contours given by the best-fit model. The Figure clearly shows that the dark lane is well reproduced. Since the envelope model, Equation (3.1), is axially symmetric, the asymmetries of the lower lobe are ignored. Thus, the model yields the discrepancy seen between it and the observation.

A second effect of the neglect of asymmetry is that the lower lobe flux, which in the image is concentrated on the left hand side, is distributed among the complete lower lobe in the model. Since both fluxes are equal in magnitude, the model ends up with a smaller maximum.

Besides the rotating, infalling envelope model as described in Equation (3.1), a spherically symmetric density distribution as a model for the envelope has been

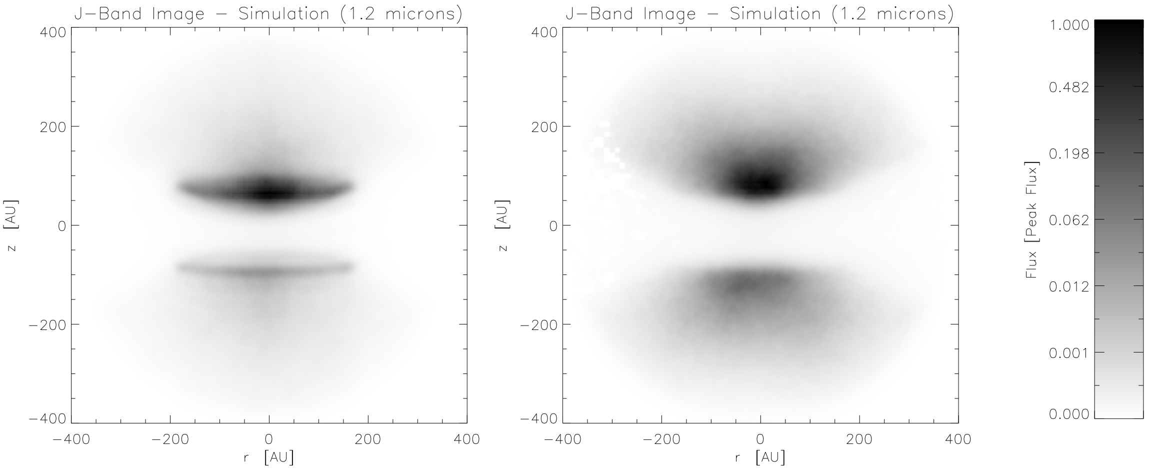

Figure 3.13.: J Band image from a simulation with a power-law envelope structure *(left)* and from rotating envelope *(right)*. The colour bar gives the flux scale for both images. The colour scale is chosen as $\sim S_\nu^{0.25}$. See also Figure 3.1 for the observation.

tested:

$$\rho_{\mathrm{env}}(\vec{r}) = \rho_{0,\mathrm{env}} r_{\mathrm{cyl}}^{\gamma} \tag{3.6}$$

This brings two parameters into the model, the normalising constant $\rho_{0,\mathrm{env}}$ and the power law exponent γ. This envelope model can reproduce the dependency of the dust lane wideness on wavelength as well as the overall SED. Yet, this approach has two major drawbacks:

1. The overall spatial flux distribution as seen in the I, J, H, and K images cannot be reproduced. In fact, it yields a much more concentrated flux distribution above and below the dark lane than what is seen in Figure 2.3. Figure 3.13 illustrates this.

2. In the SED a strong silicate *emission* feature appears between $8\,\mu\mathrm{m} \leq \lambda \leq 10\,\mu\mathrm{m}$. It is not possible to have the feature disappear as required by observations except for the inclination approaching values $75^\circ > \theta$. But this clearly contradicts the edge-on nature of the system.

Therefore, Equation (3.6) is not a suitable model for the envelope.

3.5.5. Inclination of the disc

Two ways are considered to determine disc inclination in this study. The first is to infer it from the millimetre observations, and the second way is to constrain it from

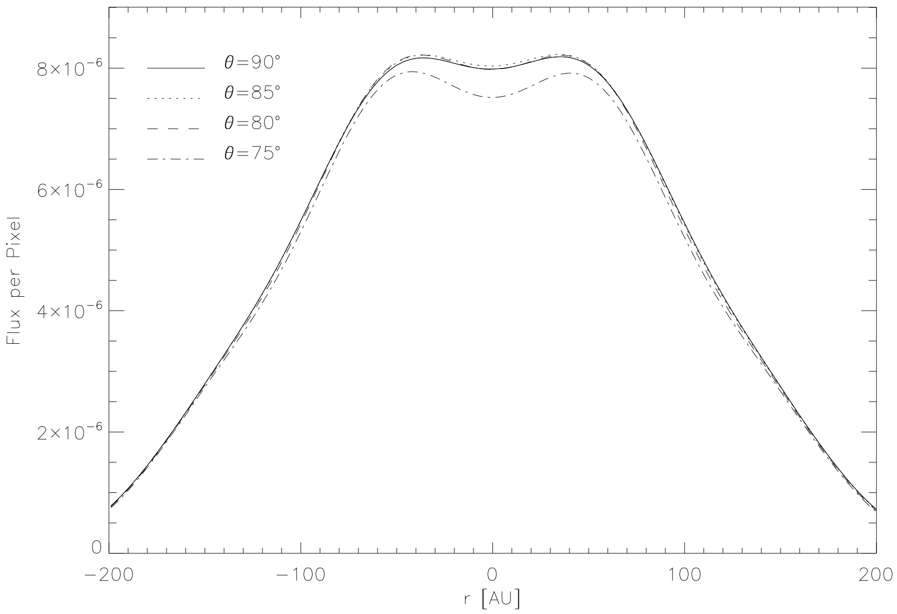

Figure 3.14.: Dependency of the brightness distribution at 1.3mm observing wavelength along a central cut on the inclination. All the curves for $\theta = 90°$, $85°$, $80°$ overlay.

the images in the near-infrared.

In Figure 3.14, the spatial brightness distribution along a horizontal cut in the 1.3mm image from the best-fit model at different inclinations is shown. For inclination values in the range of $\theta = [80° : 90°]$ the profile does not change substantially. For inclinations smaller than 80°, the profile lowers. This is because, for an observer, the warm inner rim of the disc looks like a line at exactly 90° and becomes increasingly a circle as one goes from edge-on to face-on orientation. As long as the complete rim fits into the size of the point spread function, one cannot distinguish between the different inclinations. But as soon as the rim becomes less ellipsoidal and is no longer within the scope of one beam, the flux in the centre decreases. This is what can be seen in Figure 3.14. Thus, from the comparison of models at different inclinations with the observations, one can infer a value for theta in the aforesaid range of $\theta = [80° : 90°]$. Naturally, this way of reasoning is only valid for systems optically thin in the millimetre. As outlined earlier, this is assumed the case for CB 26.

The second way to determine the disc's inclination is to compare the relative peak heights from vertical cuts through the spatial brightness distributions in the near-infrared. Assuming a symmetric system, one expects that peaks to exhibit the same height if the inclination is exactly edge-on. From an analysis of the actual peak heights (see Figure 3.11) in the HST/NICMOS images, it is possible to deduce an inclination of $\theta = 85° \pm 5°$ which is in good agreement with the numbers obtained from the millimetre images.

3.5.6. Comparison with similar objects

In general, the best-fit model has parameters that are comparable with those of the circumstellar environment of other young stellar objects. Yet, there are not many circumstellar discs seen edge-on in the sky for which the same richness of observational data is available for modelling as it is for CB 26. Hence, the number of comparable multi-wavelength studies on edge-on discs is equally limited. Two objects, HH 30 and the "Butterfly-star", share a large number of features with the disc in CB 26. All three have circumstellar discs seen almost edge-on.

Apart from these edge-on seen objects, recent observations with the SMA have revealed dust clearing of the inner disc region for the three face-on seen systems LkHα 330, SR 21N, and HD 135344B (Brown *et al.*, 2009). Aside from images, inner gaps have been identified by means of the SED (Brown *et al.*, 2007). However, the interpretation of SEDs is difficult as disc parameters are often degenerate (e.g. Boss & Yorke, 1996; Schegerer *et al.*, 2009).

Wolf *et al.* (2003) has compiled a similar data set for a model for IRAS 04302+2247, the so called "Butterfly-star". The data set includes millimetre and high-resolution near-infrared images obtained with HST/NICMOS. Utilising the same techniques, the authors' main result is that the dust properties must be different in the circumstellar disc and in the envelope. Whilst a grain size distribution with grain radii up to 100 μm is required to reproduce the millimetre observations of this disc, the envelope is dominated by smaller grains similar to those of the interstellar medium. This is quite in contrast to the CB 26 model, where grains with almost ISM-like properties are needed in both disc and envelope. However, the original millimetre images of the 'Butterfly Star' model do not suggest any presence of a large inner void as the spatial resolution is not good enough. In a later investigation (Wolf *et al.*, 2008a) on the "Butterfly-star" with the Sub-Millimetre Array the authors discover a "dip" in the horizontal brightness distribution as well. According to the model however, in this case the effect is attributed to an effect of the optical depth rather than an inner void. In Chapter 7 a new 1.3mm image with high angular resolution is presented. The image confirms the exclusion of a large inner void.

HH 30 was identified as a circumstellar disc with a large inner void by Guilloteau *et al.* (2008). The authors found an inner hole of radius $r_{\text{in}} = 40 \pm 5\,\text{AU}$ and an outer disc radius of $r_{\text{out}} = 128 \pm 3\,\text{AU}$. With this numbers HH 30 and CB 26 are quite comparable. The separation of two central stars is postulated to be about 15 AU, so this might also be a good guess for CB 26. Yet, in contrast to the model for CB 26, no envelope structure is needed to explain the appearance of HH 30 in the near-infrared bands. This suggests that CB 26 is less dynamically evolved than HH 30. Both systems drive a molecular outflow, but CB 26 shows clear signatures of outflow rotation (Launhardt *et al.*, 2009), while HH 30 does not (Pety *et al.*, 2006). The reason for this difference remains unclear, though the early dynamical state of CB 26 as compared to HH 30 may provide the key. Yet another difference between HH 30 and the CB 26 object is that the presence of cm size grains is needed to model the value for $\beta_{\rm mm}$ (Wood *et al.*, 2002). In summary, although all three objects, CB 26, HH 30, and IRAS 04302+2247, feature the same interior structure, the current investigation suggests that the systems are at different evolutionary states.

3.5.7. Errors & caveats

A matter that has not been touched so far is the uniqueness of the model. Despite the applied simplifications, the volume of the parameter space is still too vast to be completely scanned. Therefore, the step-by-step technique described above has been employed to find the parameters of the best-fit model.

For instance, the modelling started with the millimetre images as for those the envelope structure is not a dominant contribution. Thus, information about the disc total mass was obtained as well as for its inner and outer radius and the apparent absence of large dust grains. The exploration of the near infrared images then showed the requirement for a rotational envelope structure rather then a simple power law distribution. By treating the parameters in this independent and serial manner, the order in which they are fitted might become an issue. For instance, the study could first have focused on the near infrared images and wideness of the dust lane. This width usually requires small grains at least in the envelope. Modelling the SED in the millimetre regime as a second step would still have lead to the overall usage of ISM grains. This raises the question if the model is really a global minimum in the parameter space or just a local one, and if there a model exists in that space that reproduces the observations on CB 26 even better.

This possibility is excluded, however. The best-fit exhibits some unexpected features. In the framework of the parameter space study, the range of those parameters upon which these features sensitively depend has been thoroughly explored. For example, the various combinations of values for the inner radius and the scale height and disc mass have been used. If adjusted accordingly, all three can produce the plateau observed in the 1.3 mm image. However, only the larger inner radius prevailed. A small scale height might squeeze the dust tight enough for high optical depth, but clearly contradicts the wavelength dependence of the dark lane in the NIR images. The same holds for the maximum grain size. In addition, there is no way of mimicking ISM behaviour by means of disc geometry.

As a remaining issue, parameters not subject to variation in the parameter space have to be considered. As explained in the sections above, model assumptions such as spherical grains versus fractal grains can hold the key to the ‘mass problem’ of the disc. However, this would not alter the best-fit model or provide a hint to the “real” global χ^2-minimum if one thinks the model is trapped in a local minimum.

Degeneracy might also be an issue for the stellar parameters. Varying the luminosity and effective temperature of the embedded T Tauri star in general changes the total energy throughput in the radiative transfer and the location of the peak of the stellar spectrum in the wavelength space. Deviations from the assumed “typical” T Tauri star of course will affect the numbers of the best-fit model. For instance, the total mass critically depends on the flux in the millimetre regime and this flux on the total energy provided by the central star. Also, the screen introduced to mimic interstellar extinction is affected by the choice of surface temperature. However, no choice of stellar parameters is able to affect the main conclusions. These are the presence of ISM grains in the disc and the disc inner hole.

Despite the discussed caveats, the fact that it is actually possible to find a good model in the parameter space suggests that it is not necessary to introduce more complex physics, such as grain growth or dust settling. The data do not require this.

4. IRAS 18151-1208: Exploring the high-mass regime

> Ὁμοίους ἡμῖν, ἦν δ’ ἐγώ· τοὺς γὰρ τοιούτους πρῶτον μὲν
> ἑαυτῶν τε καὶ ἀλλήλων οἴει ἄν τι ἑωρακέναι ἄλλο πλὴν
> τὰς σκιὰς τὰς ὑπὸ τοῦ πυρὸς εἰς τὸ καταντικρὺ αὐτῶν τοῦ
> σπηλαίου προσπιπτούσας;
> πῶς γάρ, ἔφη, εἰ ἀκινήτους γε τὰς κεφαλὰς ἔχειν
> ἠναγκασμένοι εἶεν διὰ βίου.
>
> (*Platon*, Πολιτεία)

4.1. Discs’ role in high mass star formation

In the general course of this thesis, this Chapter might be seen as a little detour. While the major part focuses on discs around low-mass circumstellar discs, in this Chapter the applicability of these concepts to the high-mass case is investigated. This is to show that the power of multi-wavelength modelling as presented in Chapter 3 is also a valuable tool in the environment of more massive systems. This is especially important as while the role of discs in the evolution of T Tauri stars is well established, clear evidence for the massive counterpart is lacking thus far (e.g. Cesaroni *et al.*, 2007). If the grain growth and thus the formation of planetesimals is to be established along the same ideas as in the low mass case, the existence of discs is a natural requirement. In this Chapter, a multi-wavelength model of the high-mass disc candidate IRAS 18151-1208 will be presented. This model is built on a series of observations as has been done in the previous Chapter for the low-mass disc CB 26. The content of this chapter has been published in the *Astrophysical Journal* (Fallscheer *et al.*, 2011).

The high-mass protostellar object IRAS 18151-1208 is located at a distance of 3.0 kpc and has a luminosity of approximately 10^4 $L_\odot$ (Sridharan *et al.*, 2002). Single dish observations by Beuther *et al.* (2002) suggest the presence of outflow in the region.

In case of T Tauri stars, circumstellar disks and molecular outflows are integral parts of the formation process. Hence, it is logical to investigate, if a scaled up version of the low-mass case is able to reproduce observational data of IRAS 18151-1208.

4.2. Observations

4.2.1. Images

IRAS 18151-1208 was observed at 1.3mm with the Submillimeter Array on 2007 July 8 and 2007 May 17 respectively using the very extended and the compact configurations. The combination of these two configurations provided baseline lengths between 14 and 520 meters. The shortest baseline in the SMA data sets corresponds to a spatial scale of 19″. The SMA is not sensitive to structures larger than this, so supplementary short spacing information was obtained with the HERA receiver on the IRAM 30m telescope on 2006 November 12.

Combining the very extended and compact configuration interferometer data, the 1.3 mm dust continuum is mapped at a spatial resolution of ~2500 AU. Figure (Fig. 4.1) shows the primary peak of the 1.3mm image. The elongation is orthogonal to the also detected molecular outflow, and may be associated with a disk component in a roughly edge-on orientation. To simplify the analysis of the modelling, the image has been rotated by 61° such that the elongation lies along the horizontal axis. The brightness distribution along this midplane axis is slightly asymmetrical (see also Figure 4.3).

4.2.2. Spectral Energy Distribution

Data points for the SED of IRAS 18151-1208 come from various sources and are shown in Table 4.1. Figure 4.2 gives a plot of the SED. The 1.3 mm data point for the SED is determined by measuring the interferometric flux of IRAS 18151-1208 within the central 10,000 AU by 10,000 AU region.

The flux measured with the interferometer is a factor of four smaller than the corresponding integrated single dish flux reported by Marseille *et al.* (2008). The discrepancy comes from the fact that Marseille *et al.* (2008) integrate over a much larger area. In order to use the 450 and 800 μm fluxes by Marseille *et al.* (2008) nevertheless, these fluxes are divided by a factor 4 since they were measured over the same spatial scales as the 1.3mm data. For the SED, the 24.8 μm point comes from Campbell *et al.* (2008) and the 12.8 μm and 18.7 μm data points are the result of VLT/VISIR observations on 2006 August 5.

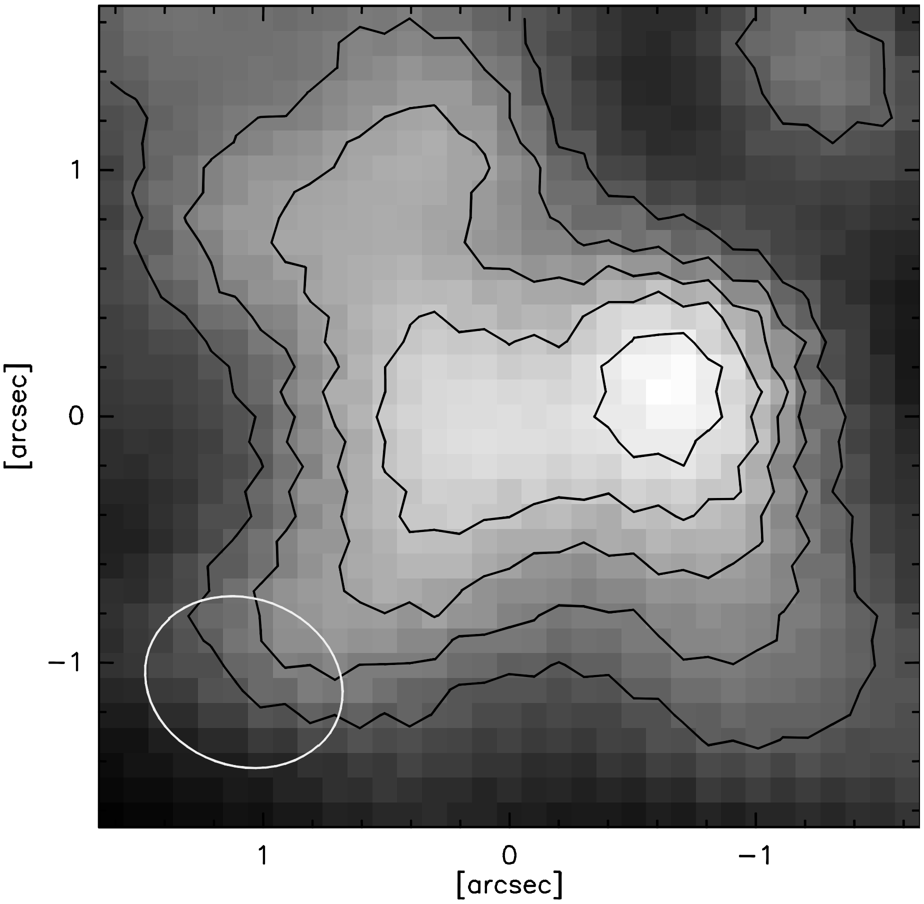

Figure 4.1.: The primary peak of the 1.3 mm dust continuum. The image is rotated by 61° in order to align the elongation with the horizontal axis. The size of the beam is indicated in the lower left corner. The integrated flux in this area is 0.4 Jy. At 3.0 kpc, 1″ corresponds to 3000 AU.

4.3. Modelling

4.3.1. Constraints from observations

The available data for IRAS 18151-1208 is not as abundant as in the case of CB 26. For instance, there are (as of yet) no near-infrared images. Consequently, it cannot be expected that a model as elaborate as for CB 26 can be established since not as many parameters can be constrained.

As for CB 26, the disc geometry can roughly be inferred from the millimetre image and used as a starting point for the investigation of the appropriate parameter space. The best-fit model shall be able to reproduce the elongated structure in the millimetre image (Figure 4.1). Figure 4.3 shows the brightness distribution along the major axis of the elongation in this image. This axis is supposed to be the midplane

λ (μm)	Flux (Jy)	+/- (Jy)	Aperture ($''$)	Reference
12.8	26.3	2	5.0	(1)
18.7	41.0	2	5.0	(1)
24.8	101	30	1.9	(2)
450	12.4	3.7		(3)
800	1.9	0.6		(3)
1300	0.4	0.1	3.3	(4)

Table 4.1.: SED data points. The 450 and 800 μm fluxes are a factor of 4 smaller than the single dish fluxes published in Marseille *et al.* (2008) in order to make a more direct comparison with the interferometer data. For more details see Fallscheer *et al.* (2011). References: (1) H. Linz, *priv. comm.*; (2) Campbell *et al.* (2008); (3) Marseille *et al.* (2008); (4) Fallscheer *et al.* (2011).

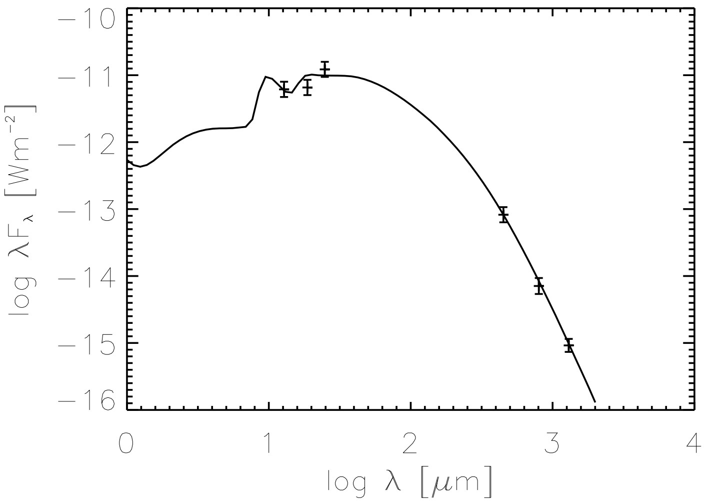

Figure 4.2.: The SED of the best fit model. Due to differences in the observation methods, the 450 and 800 micron data points have been adjusted for a more direct comparison with the 1.3 mm data point (See also see Fallscheer *et al.* (2011)).

of the circumstellar disc. As one can see, the brightness distribution is asymmetric by $\approx \pm 1\sigma$. As in the case of CB 26, this could hint towards a double-peak structure from a large inner radius or some plateau caused by optical depth effects. Unfortunately, the PSF in the present case is too large to have these structures resolved, as can be seen in Figure 4.1. Since the disc model used is rotationally symmetric around the central z-axis, the inner asymmetric part of the brightness distribution is not used

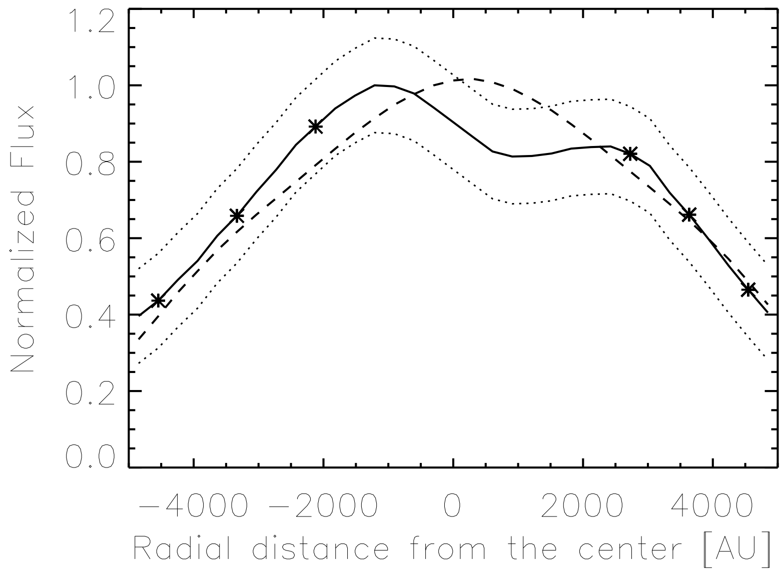

Figure 4.3.: The brightness distribution along the the midplane of the best-fit model *(dashed line)* and the observed data *(solid line)*. The dotted line refers to the observation $\pm 1\sigma$. In order to compute χ^2 of the model, the indicated data points have been used.

to estimate the best-fit model. Instead, the focus is shifted towards the outer part of the distribution. Points being used to compute the models' χ^2 are shown in Figure 4.3, too.

The model shall, of course also reproduce the observed SED data points. However, there is a caveat one needs to be aware of. As can be seen for the low-mass case, at short wavelengths the contribution of an envelope to the SED becomes dominant (cf. Figure 3.7). IRAS 18151-1208 is also embedded in an envelope and hence its spectral contributions are important in the respective wavelength regime. However, for the purpose of this Chapter and for the demonstration of the applicability of the low-mass 'disc paradigm', the omission of the envelope is an acceptable simplification given the available data. For further details see Fallscheer *et al.* (2011).

4.3.2. The parameter space

The procedures, assumptions and techniques described in Chapters 2 and 3 will be applied as widely as possible for the purpose of this Chapter. Unaltered are the density distribution as in Equations (2.2 and 2.3) with its parameters α, β and h_0. Also, the dust model as laid out in Section 2.2 will be used. As IRAS 18151-1802 is still embedded in a large-scale envelope, one can assume that if a scaled-up T Tauri evolution scheme can be applied, the object is not very old and a majority of the dust will still be ISM-like. Therefore, the maximum grain size of $a_{\max} = 250\text{nm}$ will not be a subject of this study. The same holds for the grain size distribution (Equation (2.8)) and the mineralogical composition of the dust.

Of course, some adjustments need to be made to the low-mass parameters in order to be applicable in the present context. These are then subject to the parameter space study of this Chapter. In detail, the parameters in the study are the following:

1. The central star might be the most obvious that requires adjustment. Sridharan *et al.* (2002) report that the luminosity of the IRAS 181511-1208 region is about 20,000 $\text{L}_\odot$. Consequently, the most massive star considered is a B0.5 star with an effective surface temperature $T_{\text{eff}} = 26300\text{K}$, a luminosity of $L = 20000\text{L}_\odot$, and a radius of $R_* = 7.0\text{R}_\odot$. Also tested are a B1 star ($T_{\text{eff}} = 25400\,K$, $L = 16000\text{L}_\odot$, $R_* = 6.4\text{R}_{*\odot}$) and a B2 star ($T_{\text{eff}} = 22500\text{K}$, $L = 6000\text{L}_\odot$, $R_* = 5.6\text{R}_\odot$) as central objects.

2. Other quite obvious parameters that have to be adjusted are the disc's inner and outer radii, r_{in} and r_{out}. Initially, values for r_{in} of 10, 20, and 50 AU, were investigated but in the spirit of the findings of Chapter 3 also considerably larger values such as 400, 1000, 2500, and 4000 AU were examined. As discussed already for CB 26, the outer radius can be constrained by the 1.3mm continuum observations. In order to keep the parameter space small, this value is kept fixed.

3. The next adjustment comes to the disc mass m_{disc} (or the dust mass m_{dust}, respectively). Using the common dust-to-gas ratio of 100, a dust mass of 2.2 $\text{M}_\odot$ is used to start with by means of Equation (3.4). As in the low mass case, the strongest constraint to total dust mass comes from millimetre observations.

4. If the scale-up of the low-mass case is to work, the geometrical disc parameters α, β, and h_0 should be the same or at least comparable to the low-mass case. At first, 13 values of α between 1 and 4 and 11 values of β between 0.5 and 3 have been tested independently. Yet, modifying α alone does not cause significant changes in the modelling results. Hence, subsequent models followed Equation (2.4) relating α and β. Eight values have been tested for h_0 between 1 and 30 AU.

5. Finally, the inclination θ of the disk is a parameter, although not intrinsic for the model but the observer. The observations (see Figure 4.1) hint at an edge-on observed disc. Consequently, six inclination angles from 45° to 90° were tested.

Object	α	β	h_0 [AU]	m_{dust} [$M_\odot$]	θ [°]	r_{in} [AU]	r_{out} [AU]	R_* [$R_\odot$]	T_{eff} [$T_\odot$]	L_* [$L_\odot$]
IRAS 18151	2.4	1.3	200	2.2	60	20	5000	6.4	25400	16000
IRAS 04302	2.37	1.29	15	0.0007	90	0.07	300	2	4000	0.92
CB 26	2.2	1.4	10	0.003	85	45	200	2	4000	0.92

Table 4.2.: The parameters used in the best-fit model for IRAS 18151-1208. For comparison, the respective results for the 'Butterfly Star' IRAS 04302+2237 (Wolf *et al.*, 2003) and CB 26 (Chapter 3) are also shown.

4.4. Results & Discussion

The results of the modelling are summarised in Table 4.2. To demonstrate the success of the primary goal in this chapter, the respective results for the 'Butterfly Star' IRAS 04302+2237 (Wolf *et al.*, 2003) and CB 26 (Chapter 3) are also shown. While absolute parameters (e.g.. radii) and stellar parameters differ, similar values for the parameters that determine the shape of the disc (e.g.. α) are obtained in both mass regimes. Thereby, the initial hypothesis of this Chapter is strengthened. The best-fit model in comparison with the observational data is also plotted in Figures 4.2 and 4.3. The χ^2 value of the best-fit model is 2.4, while the worst combination within the parameter space achieved 30.

4.4.1. Impact of individual parameters

In Figure 4.4, the impact of the parameters of the model on the resulting SED is shown. One can nicely see that while some parameters have a very strong impact, the effect of, say, the total dust mass seems less severe.

Figure 4.4 suggests that the flaring parameter β (and via Equation (2.4) also α) is well constrained. Both, too much flaring and too little leads to considerable deviations from the observed data points. Small values for β describe a disk with a very flat 'surface' that becomes convex if $\beta < 1$. This results in less effective disc surface to be seen from the central star and consequently to less flux overall as not enough disc material can effectively be heated up. On the other hand, larger values for β describe a much more flared disc. Such discs do present more of its surface layers to the central star. But if compared to β slightly above 1, most of this extremely flared surface is at larger radii. As a result, although more stellar flux is absorbed and reemitted, this is done at larger radii and hence colder temperatures and longer wavelengths. Therefore, the short wavelength flux decreases again with growing β.

The effects of h_0 are similar. Small values for h_0 indicate a disc where the disc material is denser in the midplane region and consequently optically thicker. The optical depth decreases with wavelength and hence the effect of h_0 at large λ de-

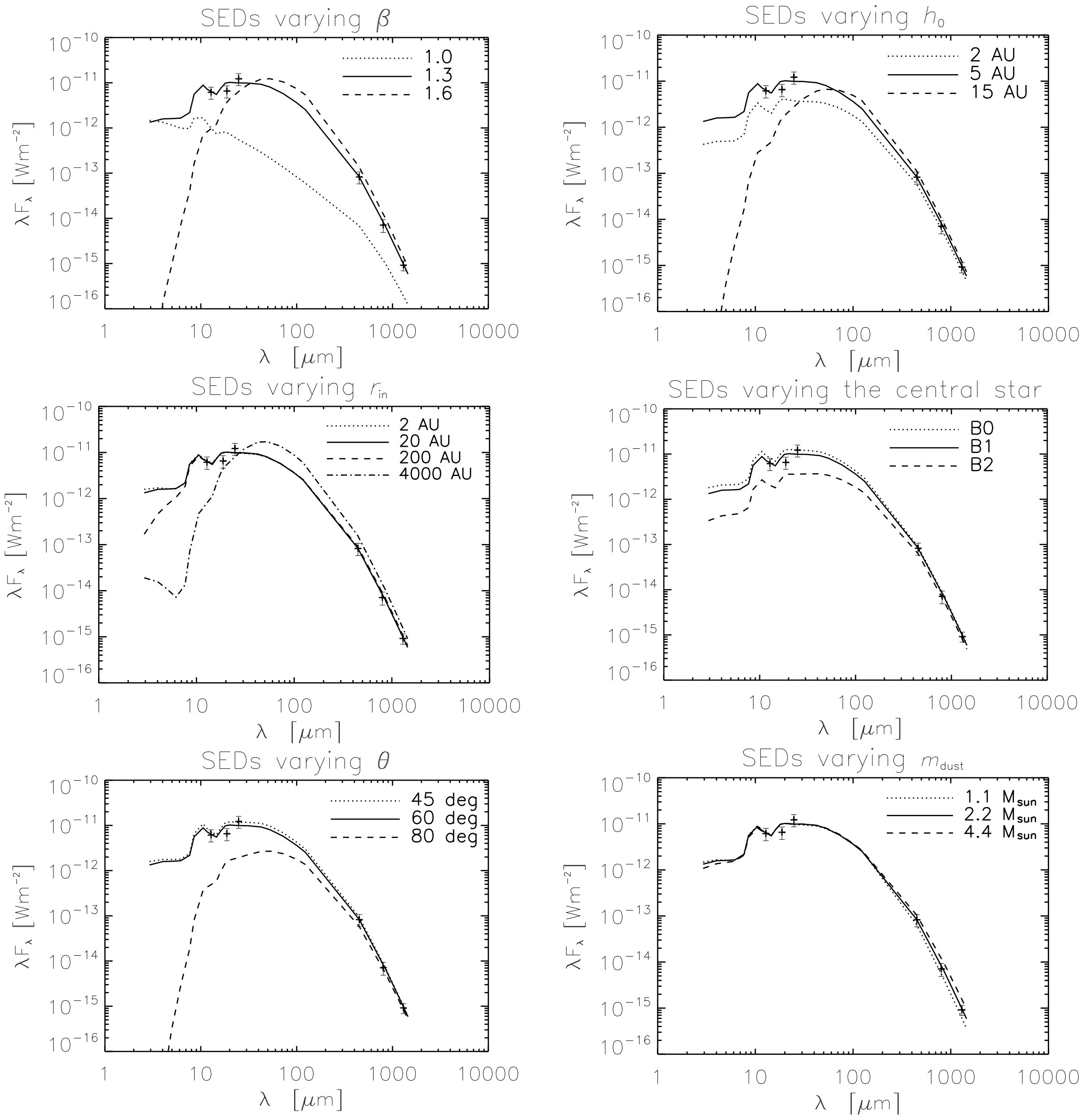

Figure 4.4.: The effects of model parameters on the SED of IRAS 18151-1208. To illustrate the impact of individual parameters most clearly, only selected values of the entire parameter space have been taken.

creases. Large values for h_0 yield thicker discs and tend to shield the central star more effectively.

In the parameter study, large values for the inner radius $r_{\rm in}$ were tested in order to approximate the central region of the brightness distribution in the 1.3mm image at least with a plateau. One of these models is shown in Figure 4.5 where $r_{\rm in} = 2500\,\rm AU$.

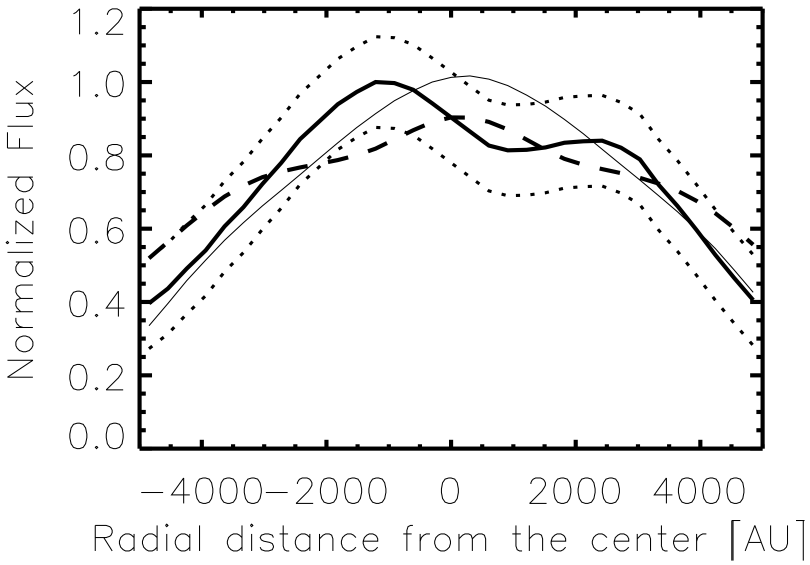

Figure 4.5.: The impact of $r_{\mathrm{in}} = 2500\,\mathrm{AU}$ on the brightness distribution in the midplane. Shown are the data *(thick solid line)*, the $\pm 1\sigma$ boundary *(dotted)*, the best-fit model *(thin solid line)* and the model with large r_{in}.

The disc described by this choice features a large inner void. However, although the central region could be modelled better than with the best-fit model (although being still symmetrical), the performance of models with r_{in} in the outer regions generally is much worse.

The inclination θ under which the disc is observed has its major impact also on the SED (Figure 4.4). While there is no real difference between $\theta = 45°$ and $\theta = 60°$, tilting the disc further towards the edge-on orientation causes considerable problems at short wavelengths.

The fact that the disc mass only affects the millimetre part of the SED is a clear indication for high optical depth at shorter wavelengths. With a gas-to-dust ratio of 100 the best-fit model yields a total disc mass of $220\,\mathrm{M}_{\odot}$. This is much more than the central star which harbours about $13\,\mathrm{M}_{\odot}$. As a consequence, IRAS 18151-1208 is an even more unstable system under the Toomre-criterion (cf. Equation (3.5)) Therefore, IRAS 18151-1208 is quite likely to fragment as described by Krumholz *et al.* (2009).

4.4.2. Applicability of the T Tauri disc scheme

The primary goal of this Chapter was to show that the disc paradigm which is successful in the low-mass regime could also be used to interpret observations of young high mass objects. By virtue of Table 4.2 one can assert that this is indeed true. When compared with the disc CB 26 of the previous chapter, the parameters describing the shape of the disc are quite similar and in each case are capable of reproducing the respective observations.

On first sight, the scale height h_0 seems to contradict this by a factor of 2, however, since $h_0 = 10\,\mathrm{AU}$ for CB 26 and $h_0 = 5\,\mathrm{AU}$ for IRAS 18151-1208. This can be resolved if one considers that in the low-mass case h_0 is taken at $r_\mathrm{cyl} = 100\,\mathrm{AU}$ which is about $\frac{1}{2} r_\mathrm{out}$ whereas for IRAS 18151-1208 $r_\mathrm{cyl} = 100\,\mathrm{AU}$ corresponds to $\frac{1}{50} r_\mathrm{out}$. Hence, h_0 should not be compared directly but moved to the same relative position in the respective disc. At $\frac{1}{2} r_\mathrm{out}$, h_0 of the massive disc is $\approx 4\%$ r_out while the relative scale for CB 26 is $\approx 3\%$ r_out. This shows nicely that the high mass disc has the same proportions as the low-mass disc and as is also demonstrated by the values for the power-law exponents α and β.

If the scaled version of the low-mass disc for the high-mass disc works, this should also be reflected in an appropriate scaling behaviour of the disc mass and outer radius. The extent of the elongated structure in the millimetre image of IRAS 18151-1208 is ≈ 10 times larger than the corresponding observation of CB 26. It is hence quite noteworthy, that the disc mass of IRAS 18151-1208 is $\approx 15^3$ times larger than in the typical low-mass case. Of course, this simplistic assessment shall not be over interpreted, and cannot by far replace detailed (and especially dynamical) studies of the evolution of young massive stars. However, this is far beyond the scope of this thesis. The results of this Chapter nicely demonstrate that an appropriate scaled of the T Tauri disc paradigm can contribute its part to this field.

5. Observing grain growth and sedimentation

> Τί δὲ τῶν παραφερομένων; οὐ ταὐτὸν τοῦτο;
> τί μήν;
>
> *(Platon*, Πολιτεία*)*

After the last two Chapters, where the focus was on the interpretation of existing observational data, in this Chapter the general effects of dust grain growth and sedimentation in the course of planetesimal formation shall be investigated. The previous Chapters have shown that although quite some constraints can be extracted from state of the art instruments, models able to constrain further dust grain features require higher spatial sensitivity. As such instruments (see Table 2.2) will become operational in the not so distant future, it is vital to identify the respective observational tracers. The present chapter addresses this need for a general investigation of the effects of dust grain growth and sedimentation on images from the near-infrared to the millimetre-regime and identify indicators that allow the classification of observations and point out directions of interest that are worth a more detailed approach in subsequent studies. The content of this chapter has been published in *Astronomy & Astrophysics* (Sauter & Wolf, 2011).

5.1. Method

The general outline of the methodology used in this Chapter has already been outlined in Chapter 2, especially in Section 2.5. The investigation requires four steps:

1. Set-up of a model that includes the effects of dust settling and coagulation as an extension of the disc model used in Chapters 3 and 4,
2. Identification of the important model parameters for the task and their range,
3. Radiative transfer computations for these models, and
4. The identification of the sought-for tracers in the simulations.

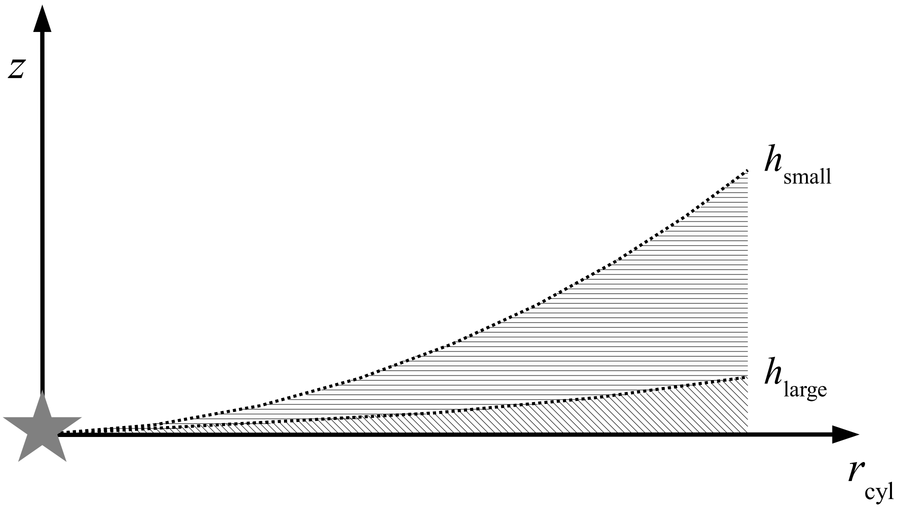

Figure 5.1.: Sketch of the general model setup. Shown are the scale heights h_{small} and h_{large} of the two dust populations with $\tilde{h} = \frac{h_{\text{small}}}{h_{\text{large}}}$. Note that the scale height is not the upper border of a dust population.

In this Section, the first three steps are dealt with.

5.1.1. The model

The basis of all models is a parametrised disc density distribution as given by Equations (2.2) and (2.3). To incorporate dust settling and coagulation, this ansatz has to be extended. In order to identify general tracers, a detailed growth picture of the dust growth process developed by Weidling *et al.* (2009); Güttler *et al.* (2009) and others is not necessary. A parametrised ansatz is more suited to this generic task. Such an ansatz has been developed and successfully employed by D'Alessio *et al.* (2006).

With this concept it is possible to formulate a parameter space that includes not only basic parameters of the coagulation/sedimentation process but also important observational parameters that do not influence the disc physics but the way observations perceive them such as the disc inclination θ.

To describe grain growth and settling, the model features two distinct dust populations which differ only in the maximum grain size. For each population, the minimum grain size is the same as found in the ISM: $a_{\text{min}} = 5\,\text{nm}$. The first population has the same maximum grain size as commonly assumed for the interstellar medium: $a_{\text{max}} = 250\,\text{nm}$ (Mathis *et al.*, 1977). This dust population is considered the reservoir of small dust grains from which the second population of larger grains is fed. The second component features a maximum grain size of 1 mm.

As described by Dullemond & Dominik (2004), the height to which a dust grain

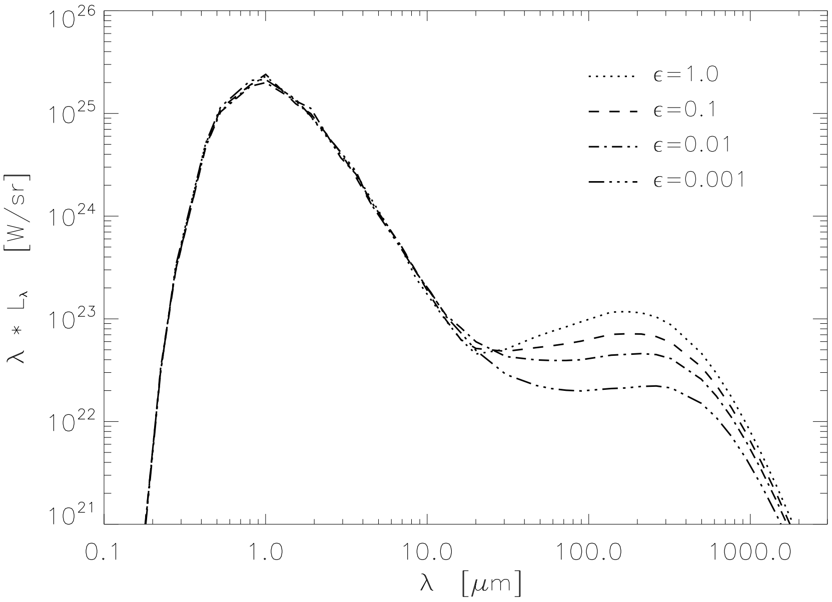

Figure 5.2.: Spectral energy distribution of the fiducial disc model seen at an inclination of $\theta = 50°$ at various stages of evolution. The depletion parameter ϵ parametrises the degree of grain growth and resulting sedimentation. Large values of ϵ indicate little growth and sedimentation and vice-versa. See Section 5.1.1 for details.

settles does not only depend on its size but also on the level of turbulence present in the disc. To model dust settling both grain populations feature different scale heights that are related via

$$\tilde{h} = \frac{h_{0,\text{small grains}}}{h_{0,\text{large grains}}}. \tag{5.1}$$

Here, $h_{0,\text{smallgrains}}$ and $h_{0,\text{largegrains}}$ are the respective scale heights. Figure 5.1 depicts the model concept.

In the initial state, both populations have the same gas-to-dust ratio. However, once the disc evolves towards the grown and settled case, the small dust grain population gets depleted and mass is transferred to the large dust grain population. The model of D'Alessio *et al.* (2006) parametrises the relative weighting of the two populations by the depletion parameter ϵ which is the relation of the gas-to-dust ratio in the small grain population ζ_{small} to the default gas-to-dust ratio $\zeta = \frac{m_{\text{gas}}}{m_{\text{dust}}} = 100$:

$$\epsilon = \frac{\zeta_{\text{small}}}{\zeta}. \tag{5.2}$$

ϵ is independent of the radial position in the disc.

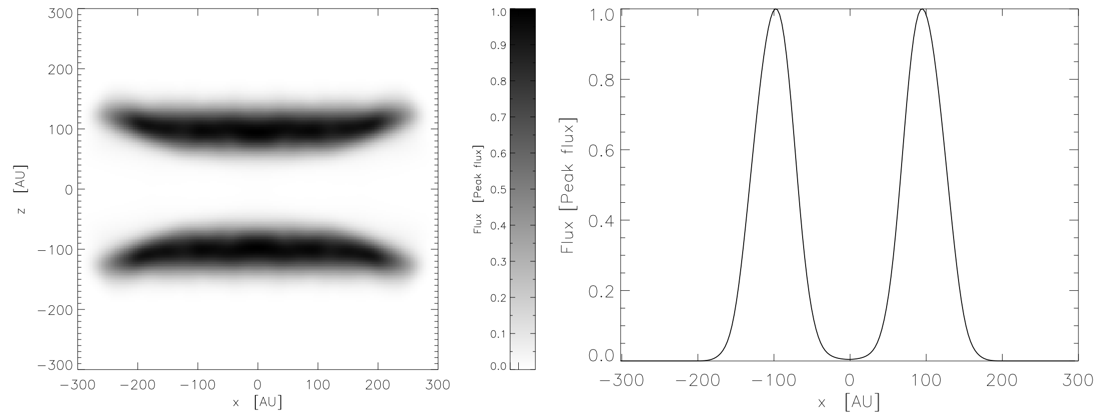

Figure 5.3.: Edge-on image (*right*) of the fiducial model with $\epsilon = 1.0$ at $\lambda = 1\,\mu$m. The lane intersecting the bipolar structure is due to the high optical depth in the disc midplane. Also shown (*left*) is a vertical cut through the brightness distribution at $x = 0$.

As no accretion by the central star nor mass loss to the ambient space is considered, the gas-to-dust-ratio ζ_{large} of the large grain population has to be altered in order to keep ζ at its initial value. The values of ζ_{large} as a function of ζ_{small} are taken from D'Alessio *et al.* (2006).

Both dust populations have the same size distribution as given by Equation (2.8) with the power-law exponent of -3.5. Also, the mineralogical composition of the dust is not altered by the extension of the model.

5.1.2. The model's parameters

The model extension with ϵ and $\tilde{h}$ introduces two new parameters to the whole disc paradigm as used in the previous chapters. A parameter space not too large is desirable as this allows more room for a finer investigation of the parameters. Consequently, some parameters that where used to fit the observational data earlier will be kept fixed here. Good choices are the parameters α and β. As can be seen from Table 4.2, their values are for individual objects quite similar and not much generality is lost by keeping them fixed. Flaring of the disc surface given by β has a significant influence on the amount of intercepted stellar radiation and consequently on the thermal structure of the disc, as well as the spatial distribution of scattered light. As discussed by Watson *et al.* (2007), these two parameters also have an impact on the width of the dark lane similar as the depletion parameter ϵ (see Section 5.2.1). Consequently, the freedom to vary α and β harbours a degeneracy in this respect. Yet, this is not necessarily a draw back: In order to understand the influence of all possible physical processes, careful investigation of each is needed separately. This is

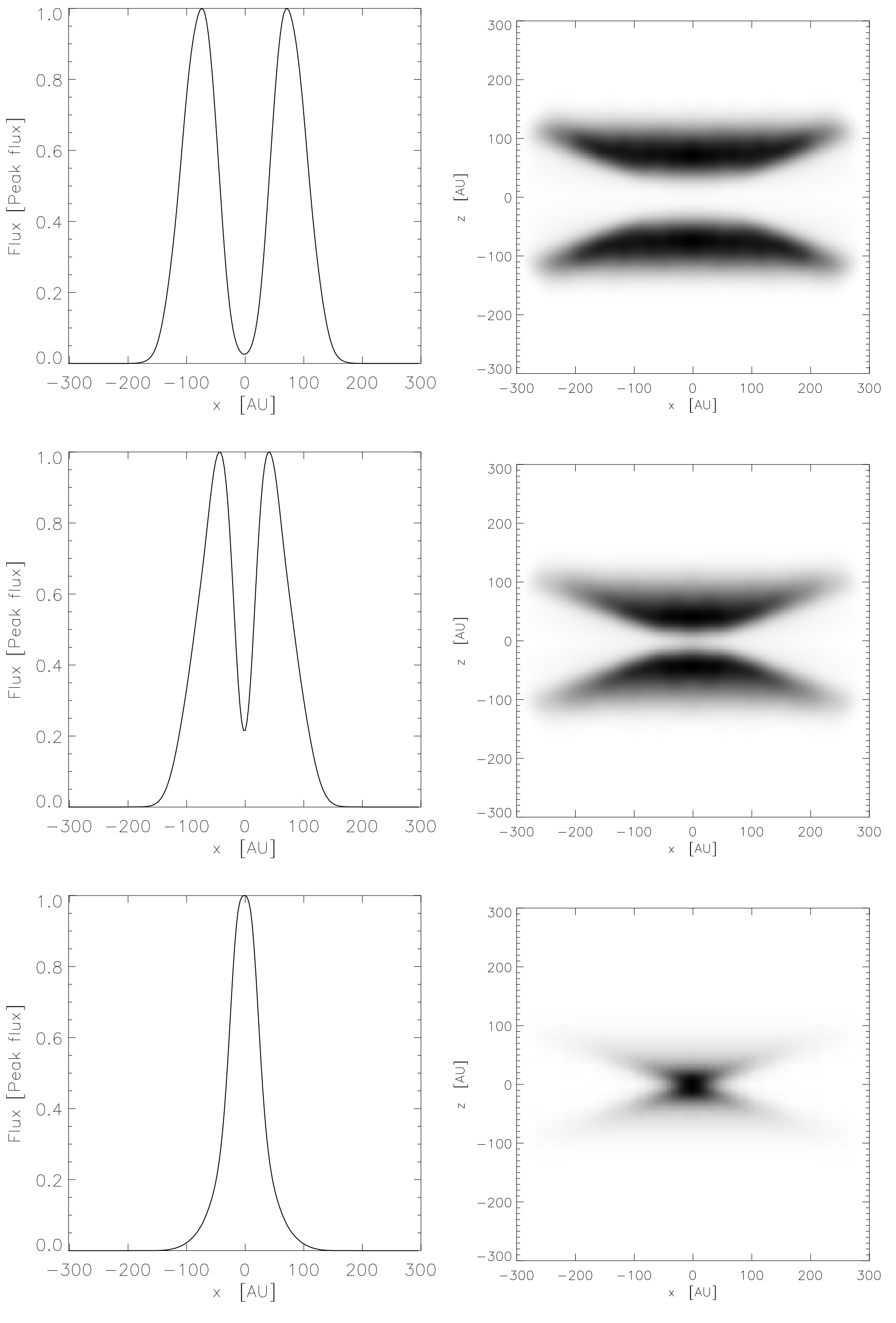

Figure 5.4.: Dependency of the dark lane in scattered light images on the depletion parameter ϵ. Shown are edge-on images and vertical cuts through them at the image centre. All flux values are normalised to the respective peak values. The images feature a linear colour scale. Shown are models with $\epsilon = 0.1$, 0.01, and 0.001, respectively. The fiducial model with $\epsilon = 1.0$ and $\lambda = 1\,\mu$m is shown in Figure 5.3. See also Figure 5.5.

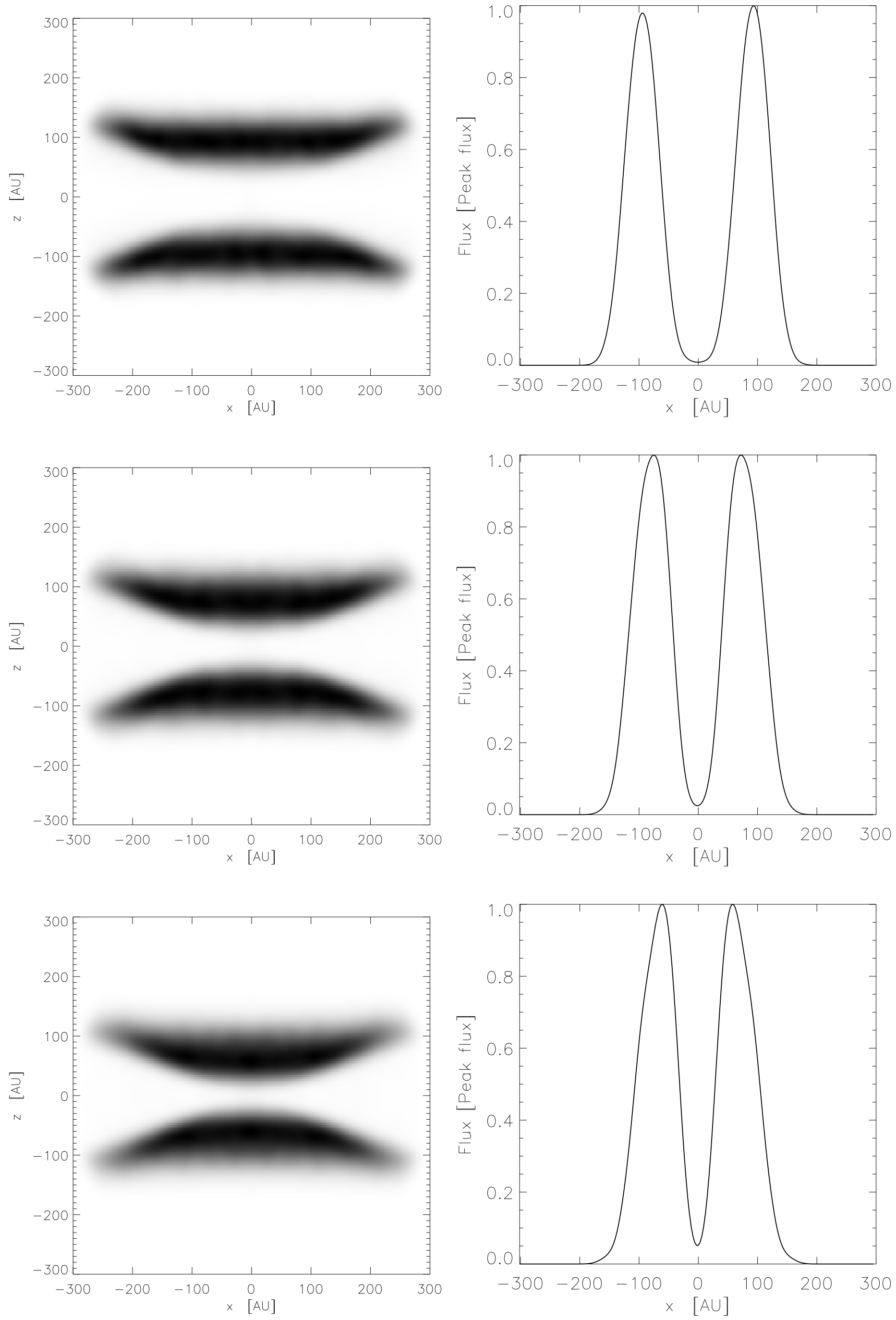

Figure 5.5.: Dependency of the dark lane in scattered light images on the observing wavelength λ. Shown are edge-on images and vertical cuts through them at the image centre. All flux values are normalised to the respective peak values. The images feature a linear colour scale. Shown are models in the J, H, and K Band, respectively. The fiducial model with $\epsilon = 1.0$ and $\lambda = 1\,\mu$m is shown in Figure 5.3. See also Figure 5.4.

done for the effects of sedimentation on images in this Chapter. In the course of this Chapter, values as obtained for the Butterfly star (Wolf *et al.*, 2003) are being used. That is, $\alpha = 2.37$ and $\beta = 1.29$. The choice of a generic T Tauri star (cf. Section 2.1) has proven to be a good central object for low-mass discs and is also employed here.

In total, the model investigated in this Chapter has five parameters intrinsic to the disc. They are joined by two observer related parameters. In detail, these seven parameters are:

- The depletion parameter ϵ. For coagulation and settling induced deviations from the default mass-to-gas relation of the small grain population the following values are used: $\epsilon = 1.0$, 0.1, 0.01, and 0.001. These values have also been used in the initial work by D'Alessio *et al.* (2006). Sticking to these allows to check if the model idea is correctly reproduced. Figure 5.2 shows the resulting SEDs.
- The relative scale height $\tilde{h}$. This level describes the level of turbulence in the disc. As this level is generally not known, three values for $\tilde{h}_0$ are adopted which are scattered around the D'Alessio *et al.* (2006) value of 10. This values are $\tilde{h} = 8$, 12, and 20.
- The inner disc radius r_{in}. Modelling efforts have shown a variety of size scales of the inner disc radius. Some discs are best described using an inner radius as small as the sublimation radius for silicate at $T = 1500\,\text{K}$. This temperature is reached at a distance of $\approx 0.07\,\text{AU}$ from the generic T Tauri star (see e. g. Section 7.3.1 and Wolf *et al.* (2003)). Other discs (cf. Section 3.5.2) apparently feature a large inner void with radii up to $\sim 45\,\text{AU}$ from the star. To incorporate both types of discs, values for r_{in} are 0.1 AU, 1.0 AU, and 10 AU.
- The outer radial extend of the disc r_{out}. The outer radius of the dust disc is also subject to variation. For discs around T Tauri stars, disc radii vary from 25 AU Neuhäuser *et al.* (2009) up to 400 AU Simon *et al.* (2000). Consequently, values for r_{out} are 100 AU, 300 AU, and 400 AU.
- The total disc dust mass m_{dust}. The values for the total dust mass of the disc span a range of three orders of magnitude: $m_{\text{dust}} = 3.2\times10^{-6}\,\text{M}_\odot$, $3.2\times10^{-5}\,\text{M}_\odot$, and $3.2 \times 10^{-4}\,\text{M}_\odot$.
- The disc inclination θ. The inclination under which the disc is observed is a non-intrinsic quantity of the model. In the case of face-on discs ($\theta = 0°$) one has direct observational access to the central star while in the edge-on case ($\theta = 90°$) the star is typically completely obscured by the dust disc. If the upper disc layers are sufficiently transparent the edge-on case allows to examine the vertical structure. Hence, both inclinations are included.

- Observing wavelength λ. To predict observational quantities in a multi-wavelength set-up, images are computed in the near-infrared, in the mid-infrared, and in the sub-millimetre and millimetre regime. Altogether, this gives images in the I, J, H, K, L, M, N, and Q Band (see Table 2.1) as well as $15\,\mu$m, $50\,\mu$m, $100\,\mu$m, $350\,\mu$m, $670\,\mu$m, $840\,\mu$m, $1100\,\mu$m, and $1300\,\mu$m. For computations of observed fluxes a distance of 140pc is assumed, representative for the well-studied low-mass star-forming region in the Taurus constellation.

5.2. Results

In the final step, the parameter space of the model is investigated for effects on various observational quantities that might allow to constrain dust settling and coagulation. In particular, the depletion parameter ϵ and the scale height relation $\tilde{h}$ are the focus of Section 5.2.1. The general result is that dust settling and coagulation as described by the depletion parameter ϵ can be constrained by various observations if the disc is seen edge-on. The respective findings are presented in Section 5.2.2 and 5.2.3. Possibilities to constrain the relative scale height $\tilde{h}$ (i. e. the amount of turbulence in the disc), is discussed in Section 5.2.4. These findings hold true only in the parameter space outlined in Section 5.1.2. Especially the exact values of modelled fluxes or the morphology of images, particularly in the mid-infrared, depend on the parameter values. Nevertheless, the qualitative behaviour of tracers for grain growth and sedimentation outlined in this Section can be also expected for models with, for instance, different choices for α, β or h_0 in the density distribution (cf. Equation (2.2)).

In the model framework, images in the NIR, $\lambda = 1\,\mu\text{m} \ldots 5\,\mu\text{m}$, are dominated by stellar light scattered on the dust grains of the disc. Due to the high optical depths at these wavelengths, only the upper layers of the disc can be seen. Images taken in the (sub)millimetre regime, $\lambda = 670\,\mu\text{m} \ldots 1.3\,\text{mm}$, trace the disc much closer to the midplane. At these wavelengths, the disc becomes optically thin even in the edge-on images. The radiation here stems from re-emission of cold dust at $\approx 30\,$K. The mid-infrared, $\lambda = 10\,\mu\text{m} \ldots 50\,\mu\text{m}$, yields images that are also dominated by thermal re-emission of the dust grains by a factor of ≈ 100 in total flux over scattered stellar light. This is also the regime where the iso-surface of $\tau_\lambda = 1$ is strongly sensitive to the specific choice of parameter values in our setup. For face-on images this yields a useful tracer for the relative scale height $\tilde{h}$ and as discussed in Section 5.2.4.

5.2.1. The fiducial model

It is insightful to discuss the effects of dust grain growth and coagulation on observable quantities and as a reference for further investigations using a fiducial model. Its parameters are given by: $r_\text{in} = 0.1\,\text{AU}$, $r_\text{out} = 300\,\text{AU}$, $m_\text{dust} = 3.2 \times 10^{-4}\,\text{M}_\odot$,

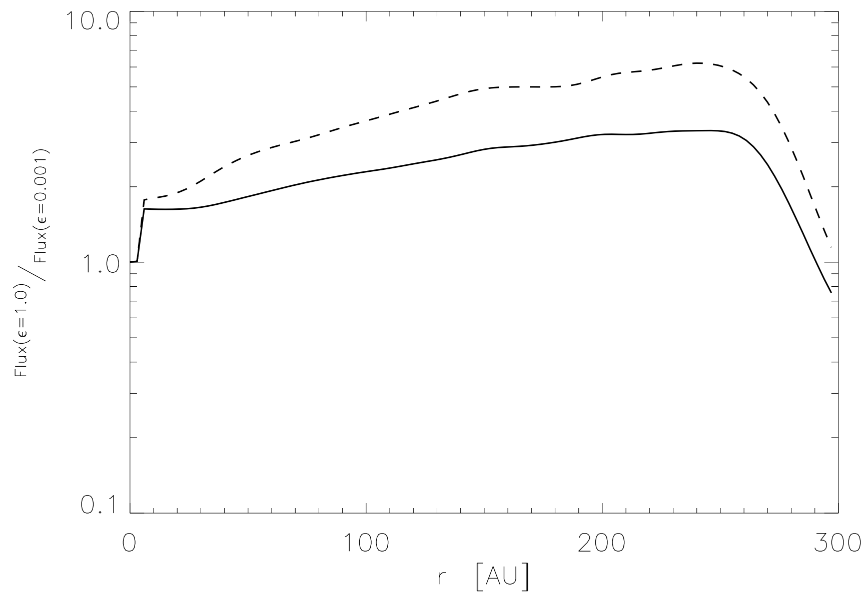

Figure 5.6.: Selected flux ratios of the radial brightness profile of the fiducial model seen in the H band face-on. The solid line shows the flux ratio between models with $\epsilon = 1.0$ and $\epsilon = 0.001$. The dashed line shows the ratio between fiducial models with $m_{\mathrm{dust}} = 3.2 \times 10^{-4}\,\mathrm{M}_{\odot}$ and $m_{\mathrm{dust}} = 3.2 \times 10^{-6}\,\mathrm{M}_{\odot}$.

$\tilde{h} = 8$, and $\epsilon = 1.0$. This approach allows to evaluate the impact of variations of the individual model parameters on the observable quantities.

Effects of the depletion parameter ϵ The depletion parameter ϵ governs how much mass is transferred from the small to the large dust grain population. Therefore, ϵ can be understood as a parameter for dust grain coagulation and the resulting sedimentation. The near-infrared images of edge-on discs exhibit a pronounced chromaticity. In this wavelength regime the disc's midplane is optically thick and shields the central star from direct observation. The height above the midplane at which the disc becomes transparent to the scattered stellar light constrains the disc's scale height.

Besides the optical properties of the dust particles, the opacity of the disc depends on the amount of dust from both dust populations present in the respective disc layers. Considering dust settling, the composition of those layers is a function of the degree of depletion. Thus, the width of the dark lane is not a function of the disc gas scale height alone but must also be a function the depletion parameter ϵ. The fiducial model exhibits this behaviour. Figure 5.4 shows the dependency of the dark lane on

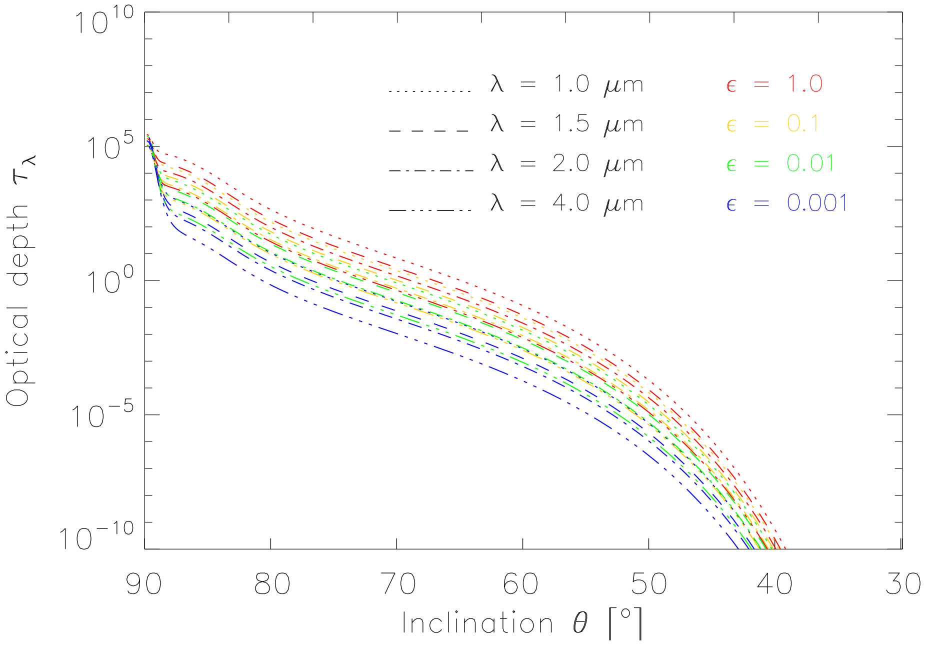

Figure 5.7.: The optical depth along radial paths for selected wavelengths as function of inclination, wavelength, and depletion for the fiducial model. Only for inclinations close to 90° is the optical depth larger then 1 for all models.

the depletion parameter ϵ and Figure 5.5 shows the dependency on the observing wavelength λ. Although the values for λ and ϵ in the plot do not exactly mirror each other, the width of the dark lane can be reproduced adjusting both parameters.

Figure 5.6 shows the relation of the radial brightness profile of the fiducial model with different total dust masses and different depletion parameters ϵ observed face-on. For $r = 0$, the ratio between the fluxes of the fiducial model with $\epsilon = 1.0$ and with $\epsilon = 0.001$ 1 since the same stellar properties are used for all models. For $r > 0$, the ratio between the brightness profiles is ≈ 2 for different depletion parameters ϵ while it is slightly sloped for different total dust masses. A variation of the density structure (i.e. α and β in Equation 2.2) can easily counterbalance the effects shown in the plot. For an inclination of $\theta = 0°$ the dependence of the brightness distribution on ϵ is almost lost.

The first reason for this ambiguity is that as the disc is tilted to smaller inclinations, the dark lane vanishes. This is because the optical depth along the line of sight decreases and more scattered stellar light reaches the observer. Figure 5.7 illustrates this for the fiducial model. Secondly, as the disc itself is still optically thick in the near infrared, it is still only the upper disc layers that are penetrated by stellar light. Hence, it is the same physical environment as in the edge-on case that determines the characteristics of the scattered light.

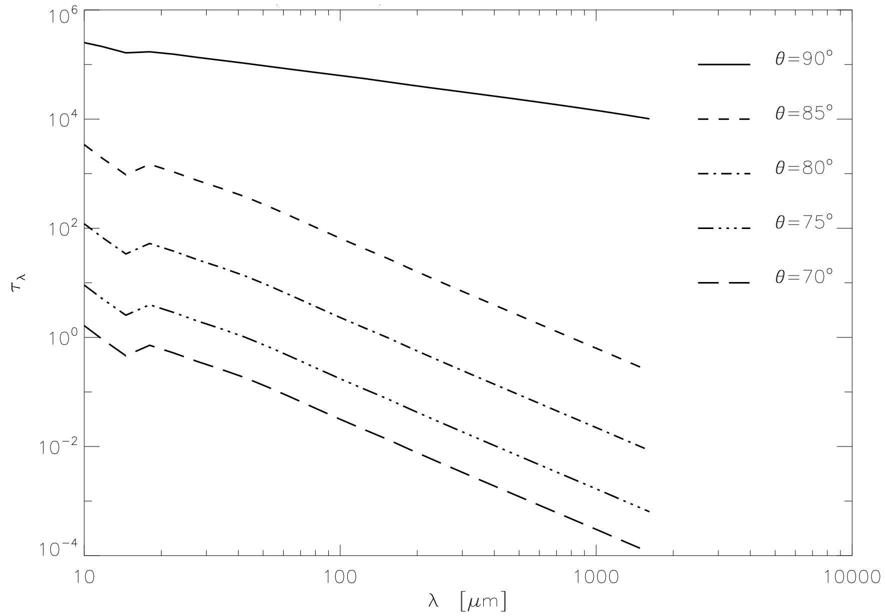

Figure 5.8.: Optical depth of the fiducial model along radial paths for selected inclinations as a function of wavelength. A high optical depth in the millimetre regime is obtained only for high inclinations while for shorter wavelengths the model is opaque in a wider range.

Figure 5.8 shows the dependency of the optical depth as a function of the wavelength for selected radial paths. A high optical depth ($\tau_\lambda \gg 1$) in the millimetre regime is obtained only at high inclinations. For shorter wavelengths, especially in the near-infrared, the fiducial model is opaque even for $\theta \sim 70°$. Figures 5.9 and 5.10 show the dependency of τ_λ along a radial path on the depletion parameter ϵ. For the edge-on orientation $\theta = 90°$ the dependency $\tau_\lambda(\epsilon)$ is very weak (Figure 5.9). Yet, 5° away from the edge-on orientation, the optical depth is much more sensitive to the depletion parameter ϵ.

For images taken in the sub-millimetre and millimetre regime no distinctive effect is observed. While absolute flux values change as the large dust grain population becomes more massive, no relative effect is seen either with respect to the location within one image or as a function of wavelength. These findings hold true for any inclination considered. Since for smaller values of ϵ more large grains are present in the system and large grains re-emit more efficiently at larger wavelengths than smaller grains do, one might expect observable effects in the millimetre regime. For the case of an edge-on disc the results are discussed in Section 5.2.2.

However, if the disc is seen face-on, there are no distinctive observable effects. Shown in Figure 5.11 as an example is the relation of the radial brightness profiles of the fiducial model at 1.3mm in a face-on view for different values of ϵ. Plotted are

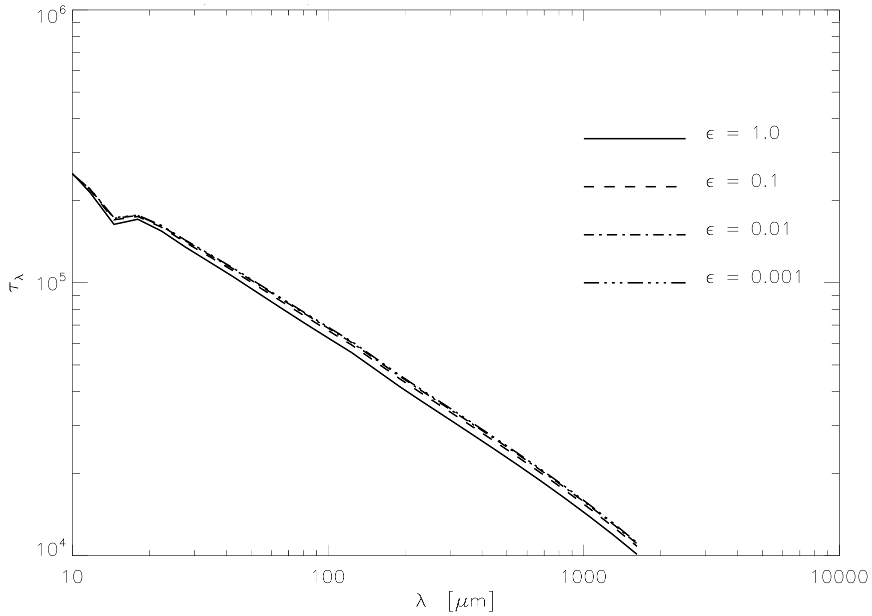

Figure 5.9.: Optical depth of the fiducial model along a radial path at 90° inclination as a function of wavelength. Only a weak dependency on the depletion parameter ϵ exists.

the relation between the $\epsilon = 1.0$ and the $\epsilon = 0.001$ model and the relation between the $m_{\text{dust}} = 3.2 \times 10^{-4}\,\mathrm{M}_\odot$ and the $m_{\text{dust}} = 3.2 \times 10^{-6}\,\mathrm{M}_\odot$ model. An obvious change is induced by a different mass. The change is larger then in the near-infrared case shown in Figure 5.6 exemplarily for the H band and it is in the order of magnitude of the respective mass relation. For both comparisons the relation is approximately constant for $r >\sim 30\,\mathrm{AU}$ rendering the relative effects (not the total flux) of the depletion parameter ϵ insignificant.

Effects of the height relation $\tilde{h}$ The height relation $\tilde{h}$ as defined in Equation 5.1 describes the level of turbulence in the disc as well as the magnitude of the viscosity parameter α. Figure 5.12 illustrates the effects of $\tilde{h}$ on the density distribution. The density distribution of the small grain population does not depend on $\tilde{h}$. According to the model set-up the large grain population becomes concentrated in a much smaller space for larger $\tilde{h}$.

The effects of $\tilde{h}$ on images at different inclinations is essentially that of an amplifier of effects caused by the depletion parameter ϵ. In the case of near-infrared images of edge-on discs, the width of the dark, high-opacity lane is affected. Larger values for the height relation $\tilde{h}$ result in a dark lane with larger contrast and vice versa. This can be readily understood in terms of optical depth. Higher values for $\tilde{h}$ essentially squeezes the large dust grain population into a smaller volume and thus increases the

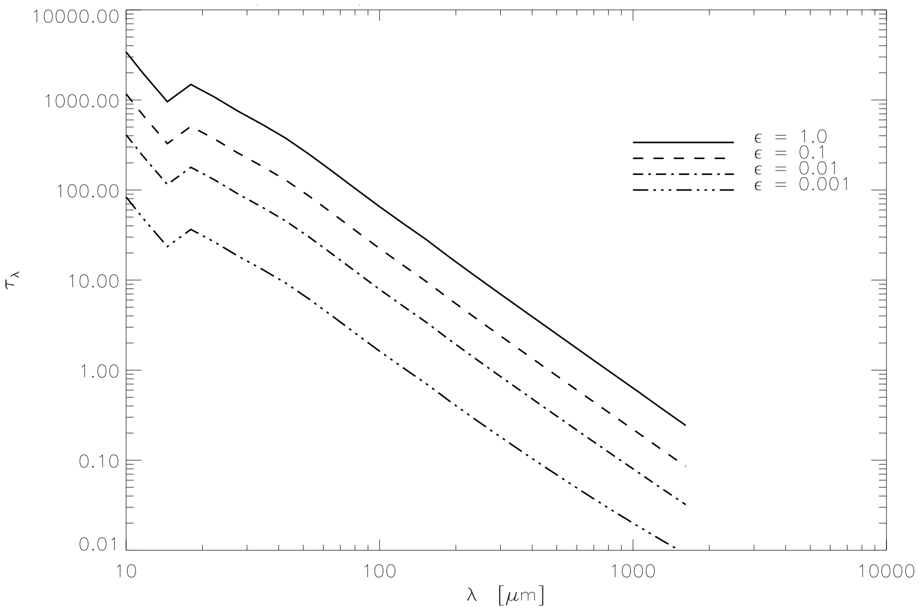

Figure 5.10.: Optical depth of the fiducial model along a radial path at 85° inclination as a function of wavelength. Unlike the situation in the exact edge-on case (Figure 5.9), the optical depth becomes sensitive to the depletion parameter ϵ by typically half an order of magnitude.

optical depth. The amplifying effect is stronger for smaller values of ϵ: more mass is packed into the large dust grain population yielding a height optical depth. The magnitude of the effects caused by the variation of $\tilde{h}$ is considerably small.

In Figure 5.13 the optical depth of the fiducial model along a radial path in the edge-on orientation as a function of wavelength is shown. The comparison with Figs. 5.9 and 5.10 shows that for $\tilde{h}$ the dependency is not as strong as for ϵ.

5.2.2. Millimetre Images

Millimetre images are well suited to classify dust settling and coagulation because at these wavelengths the dominant fraction of the radiation has its origin in the thermal re-emission of the dust grains. Further, the redistribution of the mass also alters the optical depth structure. The most illustrative way to see how millimetre images provide means to constrain disc evolution (the changing radial and vertical opacity and thus the re-emission structure) is to compare different regions of a disc image, especially if the disc is seen edge-on.

The regions of choice are depicted in Figure 5.14 and labelled (cw, starting in the image/disc centre) A, B, C, and D. One expects that as the disc evolves, the layers distant from the midplane loose more and more mass due to the dust grain growth

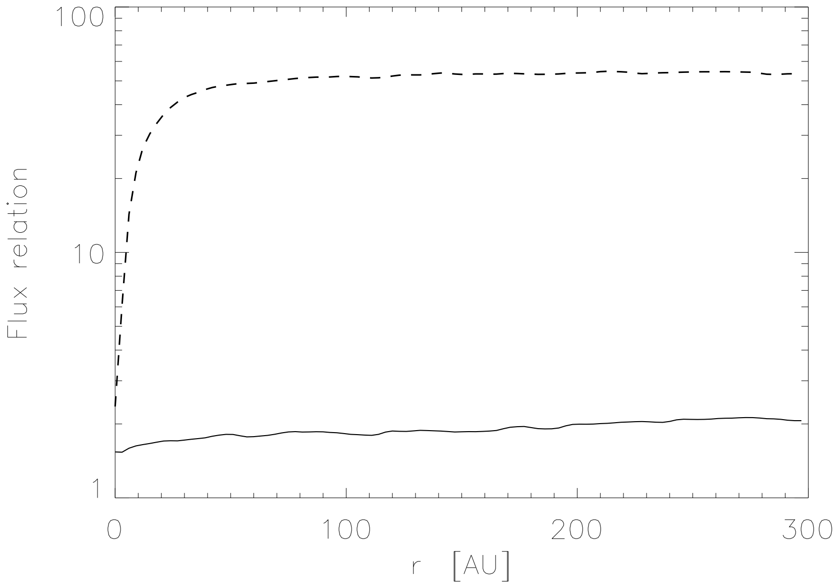

Figure 5.11.: Relative radial brightness profiles of the fiducial model at 1.3mm in a face-on view. The solid line shows the relation between the $\epsilon = 1.0$ and the $\epsilon = 0.001$ model. The dashed line shows the relation between the $m_{\text{dust}} = 3.2\times10^{-4}\,\text{M}_\odot$ and the $m_{\text{dust}} = 3.2\times10^{-6}\,\text{M}_\odot$ model. An obvious change is induced by a different mass larger than in the near-infrared case shown in Figure 5.6 exemplarily for the H band.

and settling towards the midplane, the amount of thermal re-emission from those layers decreases as well. Radiation originating close to the midplane is expected to raise or to stay at the same level, since the growing midplane mass not only yields more emitting grains but also more absorbing grains (important in the submillimetre regime). Densities values are already orders of magnitude higher close to the disc midplane, the down-raining grains therefore cannot significantly increase the optical depth and thus level any gain in emitter numbers.

Figure 5.15 shows exemplarily these findings by relating the flux from the four different regions to the total flux. Starting from red for the early, $\epsilon = 1.0$ case and ending at blue with a depletion parameter $\epsilon = 0.001$. The shape of any mark denotes the region from whence it is taken. Plotted is the relative flux from a certain region versus the size of that region. The latter can be understood as the degree of resolution of the observing instruments. As an indicator, the maximum resolution 1.3mm of various instruments (ALMA, PdBI, SMA) is given as dashed black lines. Although all three interferometers shown in the plot provide the required resolution to detect the effect, only ALMA provides the required sensitivity. As the flux is given in units

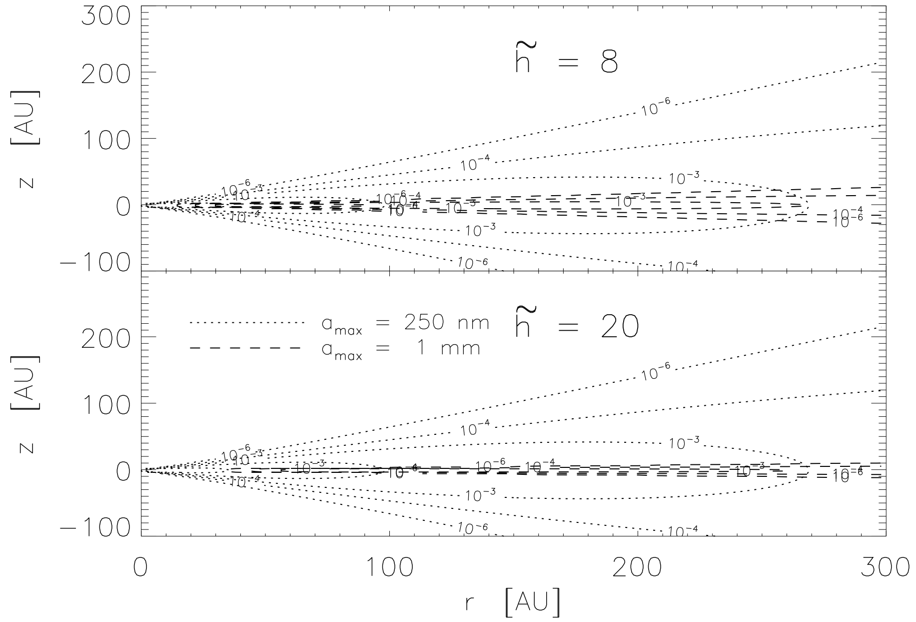

Figure 5.12.: Contour lines of the density distribution normalised to the respective peak density of the two grain populations. The two panels show the effect of small (*top*) and large (*bottom*) relative scale height $\tilde{h}$.

of the total flux of the image, which depends on ϵ, the sensitivity is also a function of ϵ. As expected, fluxes taken in the midplane do not vary considerably with the evolutionary state: all four colours are almost atop of each other. However, for fluxes taken from above the disc midplane, a clear decrease in flux is visible. From the initial $\epsilon = 1.0$ to the final $\epsilon = 0.001$, it spans almost two orders of magnitude.

This effect of flux decrease though is limited to the edge-on case, only. Figure 5.16 (*left*) depicts the same analysis as done in Figure 5.15 but with an inclination of $\theta = 60°$. At inclinations of $\theta = 60°, 0°$, the lines of sight are no longer within the midplane or any parallel plane but intersect higher disc layers as well as the disc midplane. As a result the radiation comes from various disc layers, representing different stages of dust coagulation and sedimentation. The amount of flux collected in the four different regions is not a function of the depletion anymore but just of the disc's geometrical thickness. As the inclination can be determined from image-morphology, these findings are a valuable tracer for dust sedimentation in the edge-on case. The robustness of this result is estimated by considering the influence of disc parameters other than the depletion factor ϵ. Although the total flux value from different regions changes, the effect of separation of the flux values in the upper and lower layers of the image with later evolutionary states does not depend on the chosen parameter value. It is also independent of the observing wavelength in the (sub) millimetre

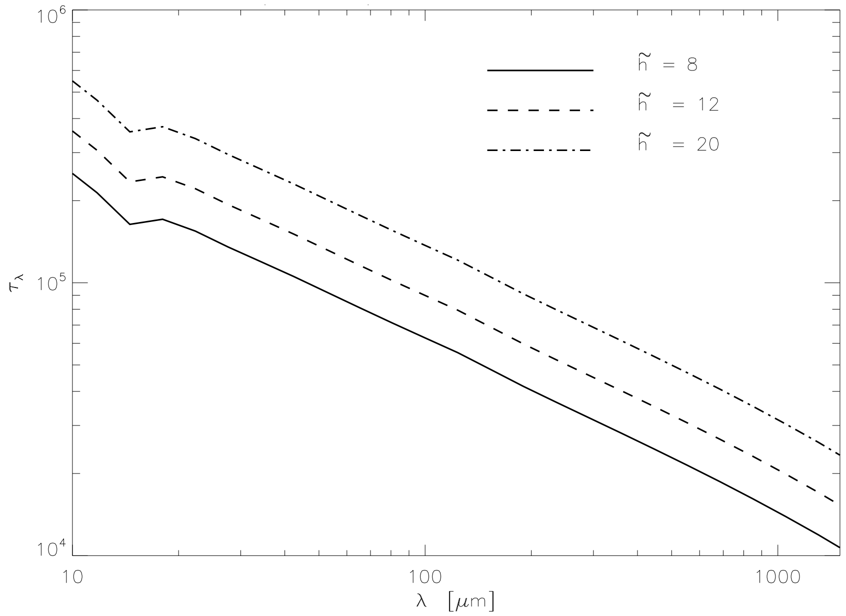

Figure 5.13.: Optical depth of the fiducial model along a radial path at 90° inclination as a function of wavelength. Plotted is the dependence on the relative scale height $\tilde{h}$. A comparison with Figure 5.10 shows, that the dependence on $\tilde{h}$ is not as pronounced as the dependency on ϵ.

regime. Figure 5.16 (*right*) shows this exemplarily for the dependency of the fluxes of the respective regions on the scale height relation $\tilde{h}$.

5.2.3. The disc in N and Q band edge-on

The re-emission in N and Q bands dominates the scattered stellar flux by several orders of magnitude. Morphologically, it is the transition region from the ‘dark lane’ type of brightness distribution as seen in the near-infrared (see Section 5.3.2) to the extended and elongated typical for (sub)millimetre images. In the edge-on images, the typical central dark lane is very thin, in the order of one resolution element of the Giant Magellan Telescope.

The major difference to millimetre images of edge-on discs is that the flux due to re-emission is concentrated in the central region while at increasing wavelengths the emission becomes increasingly extended as cooler material dominates the emission. Based on the model framework, various morphologies that can be observed in this wavelength regime. Possible scenarios include a single central peak, two elongated emission regions separated by a dark lane, three emission maxima in the midplane, a four-legged x-like shape and others more. Figure 5.17 gives an impression of the variety of possibilities. The reason for this zoo of different morphologies resides in the

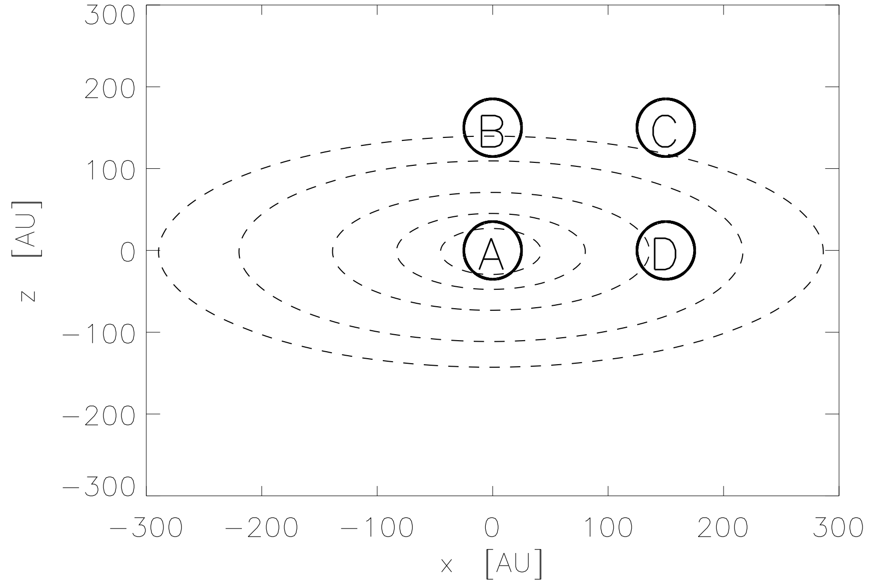

Figure 5.14.: Location of the four regions used to compare intensities. The dashed lines are logarithmic contour lines of the brightness distribution of the fiducial model observed at $\lambda = 1.3\,\mathrm{mm}$ and $\theta = 60°$.

fine-tuning of the optical depth. Depending on the total mass and its distribution, different regions of the disc are rendered opaque enough for a specific choice of values parameters such that their radiation contributes to an image (or not). In most cases τ_λ is close to unity within an order of magnitude.

However, the overall width of the brightness distribution turns out to be a valuable tracer for dust grain growth and sedimentation in the edge-on case (see Figure 5.18). A linear relation between the FWHM of the emissions in the two bands is observed. For all possible combinations of parameters, the scattering of the Q band peak width vs. the N band peak width is strongest for a large depletion parameter and ceases for later evolutionary stages. Introducing a straight line as a fit, the chi-square ($\tilde{\chi}^2$) is a function of the depletion parameter ϵ as shown in Table 5.1.

Depletion ϵ	Linear slope	$\tilde{\chi}^2$
1.0	1.0	10715
0.1	0.9	1820
0.01	0.8	381
0.001	0.8	191

Table 5.1.: Linear slope and $\tilde{\chi}^2$ of the N/Q band width of the models.

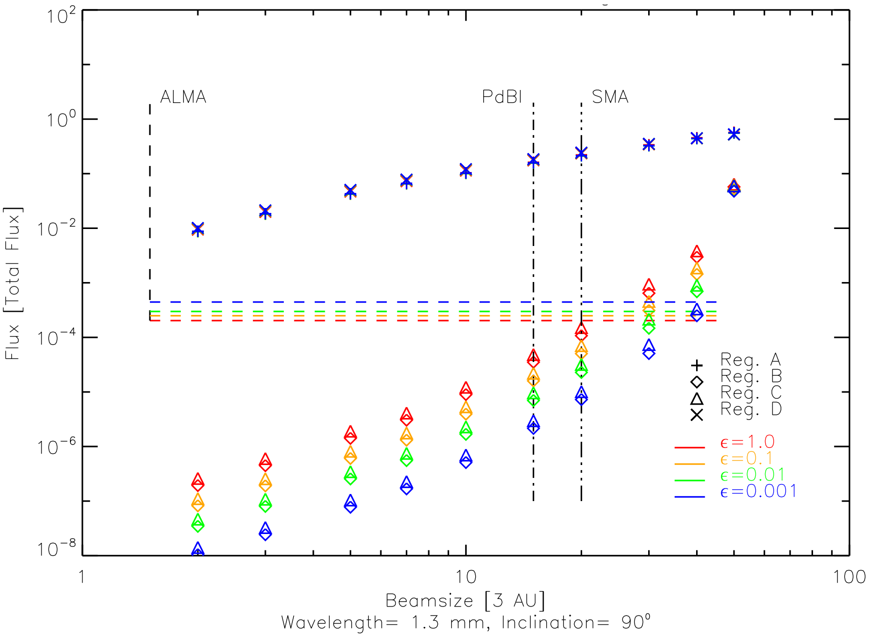

Figure 5.15.: Analysis of image brightness distribution of a circumstellar disk at different evolutionary stages. The results for different evolutionary states are coded in colour. The shape of any mark denotes the region from whence it is taken. Vertical lines indicate resolution limits of selected interferometer. Horizontal lines give the ALMA sensitivity limit, the other two instruments do not have the required sensitivity. The flux is given in units of the total flux. Since this flux depends on ϵ as well, the sensitivity limit is affected. The dependency of the flux in regions B and C on ϵ is shown.

The reason for this increasing linearity is the fine-tuning of the optical depth. Re-emitted radiation received from the object originates at regions with an optical depth smaller than unity. For large values of ϵ the disc dust mass is distributed over a larger volume. Thus, the iso-surface with τ_{Nband} has more morphological freedom. Consequently, the width of the brightness distribution of one disc model picked at random depends more on the setting of the other parameters than this is the case for smaller values of ϵ. There the bulk of matter is concentrated close to the midplane and the shape of the regions seen is less subject to a specific choice of parameters: The density distribution of the large grain population determines the width of the brightness distribution alone, not the interplay between two grain populations.

The specific value of the slope in Table 5.1 is roughly determined by the wavelength dependency of τ and the vertical density increase of the large dust grain population as given by Equation 2.2. Increasing the observing wavelength from 10 μm to 20 μm allows a deeper look into regions of higher disc densities. For $\epsilon = 0.001$ a slope of 0.8

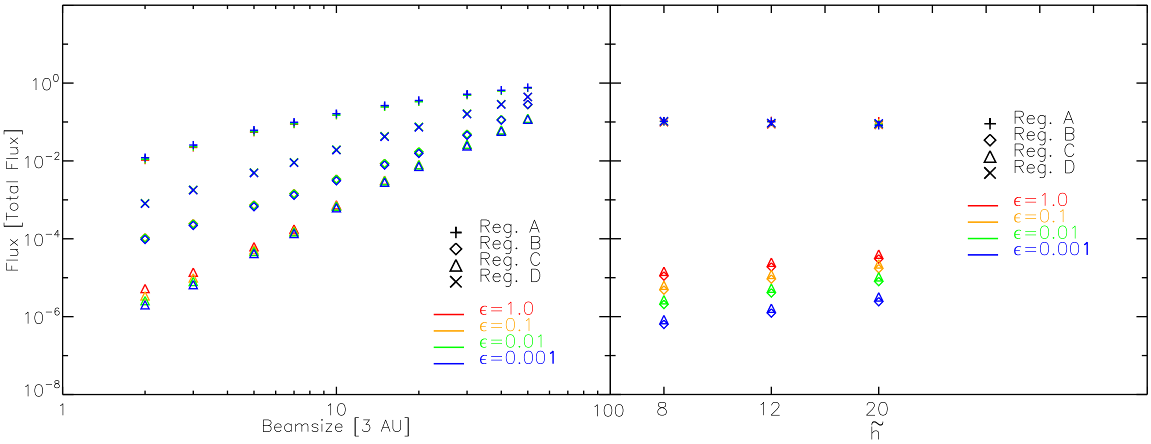

Figure 5.16.: *Left:* Same analysis as in Figure 5.15 at an inclination $\theta = 60°$. A dependency on the depletion parameter ϵ cannot be seen.
Right: The robustness of the flux change in upper disc lanes shown here exemplarily as a function of relative scale height $\tilde{h}$.

implies that the Q band image is a little thinner than the N band image. This means that the spatial gain by reduced optical depth is almost counterbalanced by the increased density in deeper layers. Within the parameter space the FWHM-relation of the emission thickness in N and Q band for one disc depends on the total dust mass. An analysis of disc models shows, that they group in Figure 5.18 according to their total dust mass, not their relative scale height, as shown in Figure 5.19. This is also true for later evolutionary stages.

Consequently, the evolutionary stage of a single observed disc can be inferred by comparing the extent of the emission in the N and Q band only. The precise value of this relation will depend on the global geometry of the disc. Nevertheless, a peak width ratio of ~ 0.8 from Q to N band is a good indicator for discs with most of their masses settled in large dust grains close to the midplane.

5.2.4. Q and N band face-on: Turbulence digs in

This Section investigates the possibility to constrain the relative scale height $\tilde{h}$. Figure 5.17 already indicates that images in the N and Q band are sensitive to the fine-tuning of the density distribution. Figure 5.20 illustrates this in the N band for the case of face-on discs. In this regime the observed flux originates predominantly from re-emission of hot dust at $\sim 300\,\mathrm{K}$.

The marker for the relative scale height is the gap in the flux distribution at intermediate disc radii of $\sim 100\,\mathrm{AU}$. The strength of this emission gap depends directly on the relative scale height $\tilde{h}$. For large $\tilde{h}$, i. e. a small scale height of the large dust grain population, the gap is clearly visible. It ceases for smaller values of

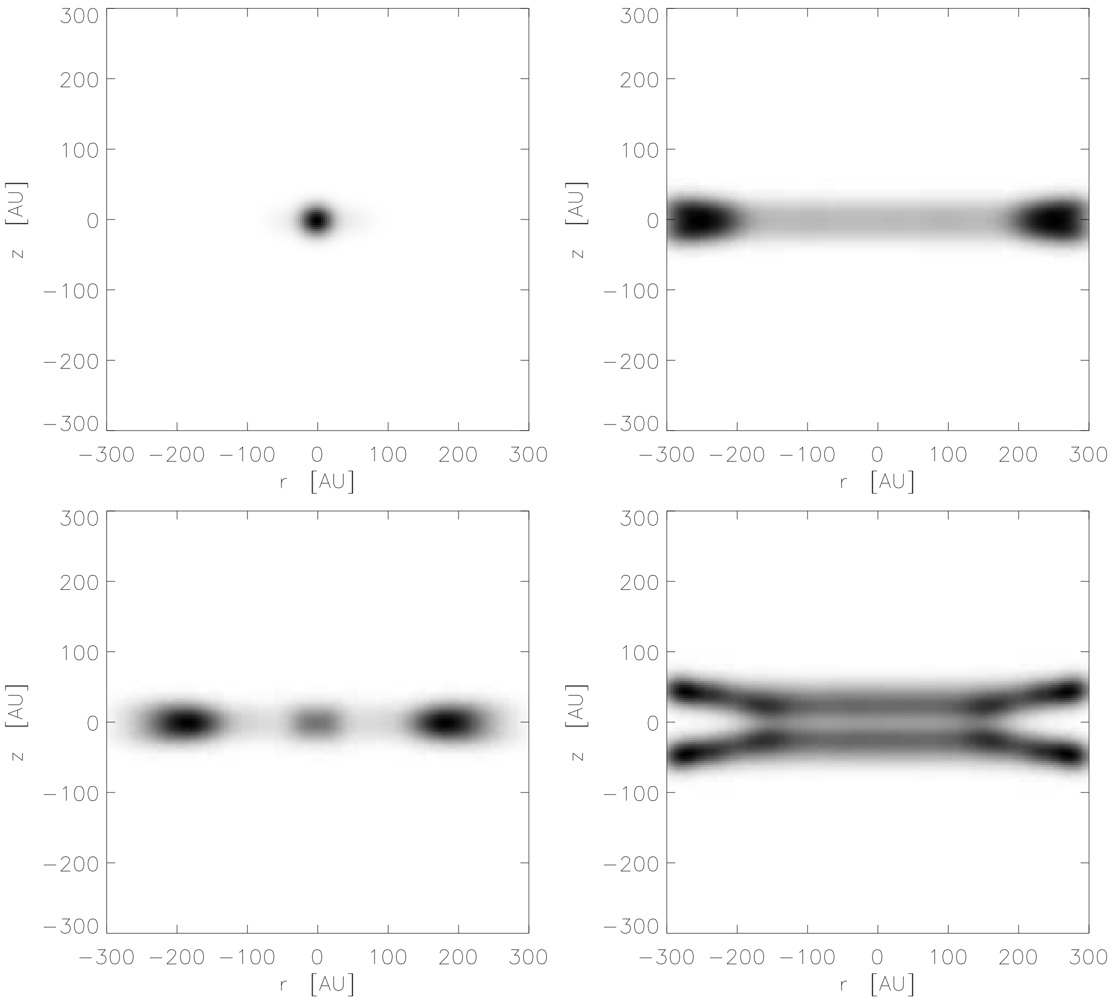

Figure 5.17.: Morphologies of an edge-on disc in the N band with $r_{\rm in} = 0.1\,{\rm AU}$.
Top left: $m_{\rm dust} = 3.2 \times 10^{-6}$, $r_{\rm out} = 300\,{\rm AU}$, $\tilde{h} = 12$, $\epsilon = 0.001$.
Top right: $m_{\rm dust} = 3.2 \times 10^{-4}$, $r_{\rm out} = 300\,{\rm AU}$, $\tilde{h} = 20$, $\epsilon = 0.1$.
Bottom left: $m_{\rm dust} = 3.2 \times 10^{-4}$, $r_{\rm out} = 300\,{\rm AU}$, $\tilde{h} = 20$, $\epsilon = 0.1$.
Bottom right: $m_{\rm dust} = 3.2 \times 10^{-4}$, $r_{\rm out} = 400\,{\rm AU}$, $\tilde{h} = 8$, $\epsilon = 1.0$.
All images feature a linear colour scale.

$\tilde{h}$. The effect also depends on the observing wavelength.

The nature of this apparent gap can be understood by analysing the spatial temperature distribution together with the optical depth. Figure 5.21 shows temperature contour lines of the large-grain population enclosing regions with temperatures higher than the black-body emission peak in the Q and N band. This emission peak occurs for the Q band at 144K and in the N band at 315K. Regions outside are cooler. Closer to the midplane the reason for this is the high optical depth such that the ma-

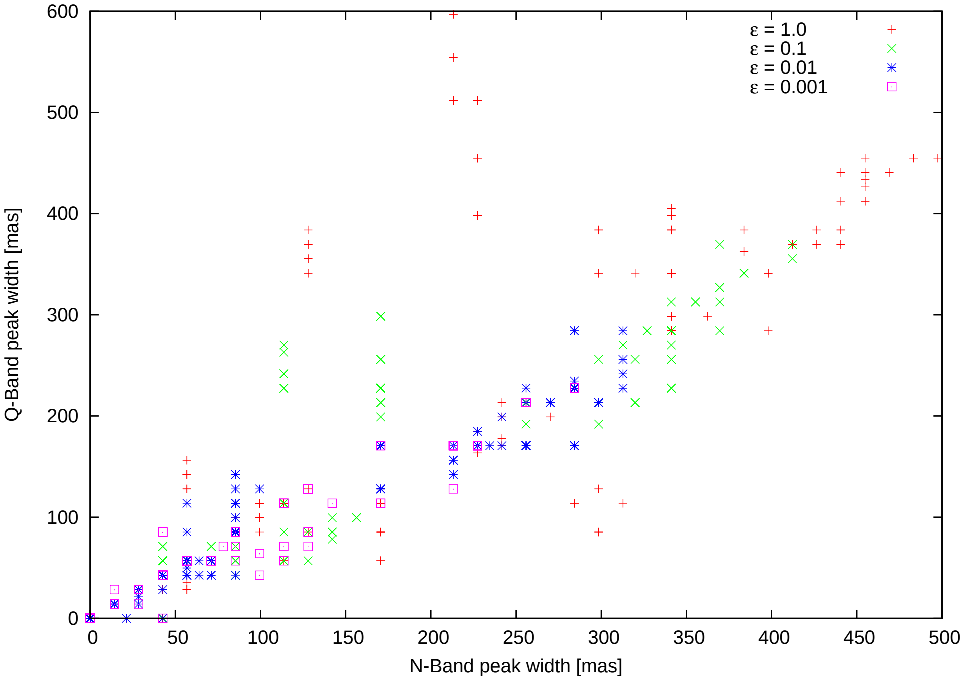

Figure 5.18.: FWHM of the height of the emission in N band versus the same in Q band for different values of the depletion parameter ϵ. A general tendency of a linear relation between the FWHMs for smaller values of ϵ can be observed.

terial there cannot be heated effectively by stellar radiation. Far above the midplane the density of the disc is too low to assign a meaningful temperature (cf. Figure 5.12). Figure 5.21 also shows the $\tau_{\mathrm{Q,N}} = 1$ isoline for the two bands obtained by integrating perpendicular to the midplane, starting at $z = \infty$. For both bands and the two extreme values for $\tilde{h}$, the high temperature regions of the small grain population are far above the $\tau_{\mathrm{Q,N}} = 1$ line and are not shown in the plot. In both bands, these regions most efficiently contribute to the face-on image of the disc for any value of $\tilde{h}$. These regions are the origin of the flux peak in the centre, cf. Figure 5.20.

In the Q band, also the large-grain population contributes to the image for both values of $\tilde{h}$. Unconvolved face-on images show that the surface brightness of the small-grain population is about an order of magnitude larger. The emission region of the small grain population is close to the rotation axis of the system. Seen from above, all emission of the small grain population is seen piling up in a narrow region while the emission regions of the large grain population are stretched above the midplane. In the edge-on case, this geometrical effect yields the opposite result: The emission from the large grain population is seen in a smaller area and thus contributes more to the image than the small grain population.

Matters are different in the N band. An optical depth of $\tau_{\mathrm{N}} = 1$ is reached at

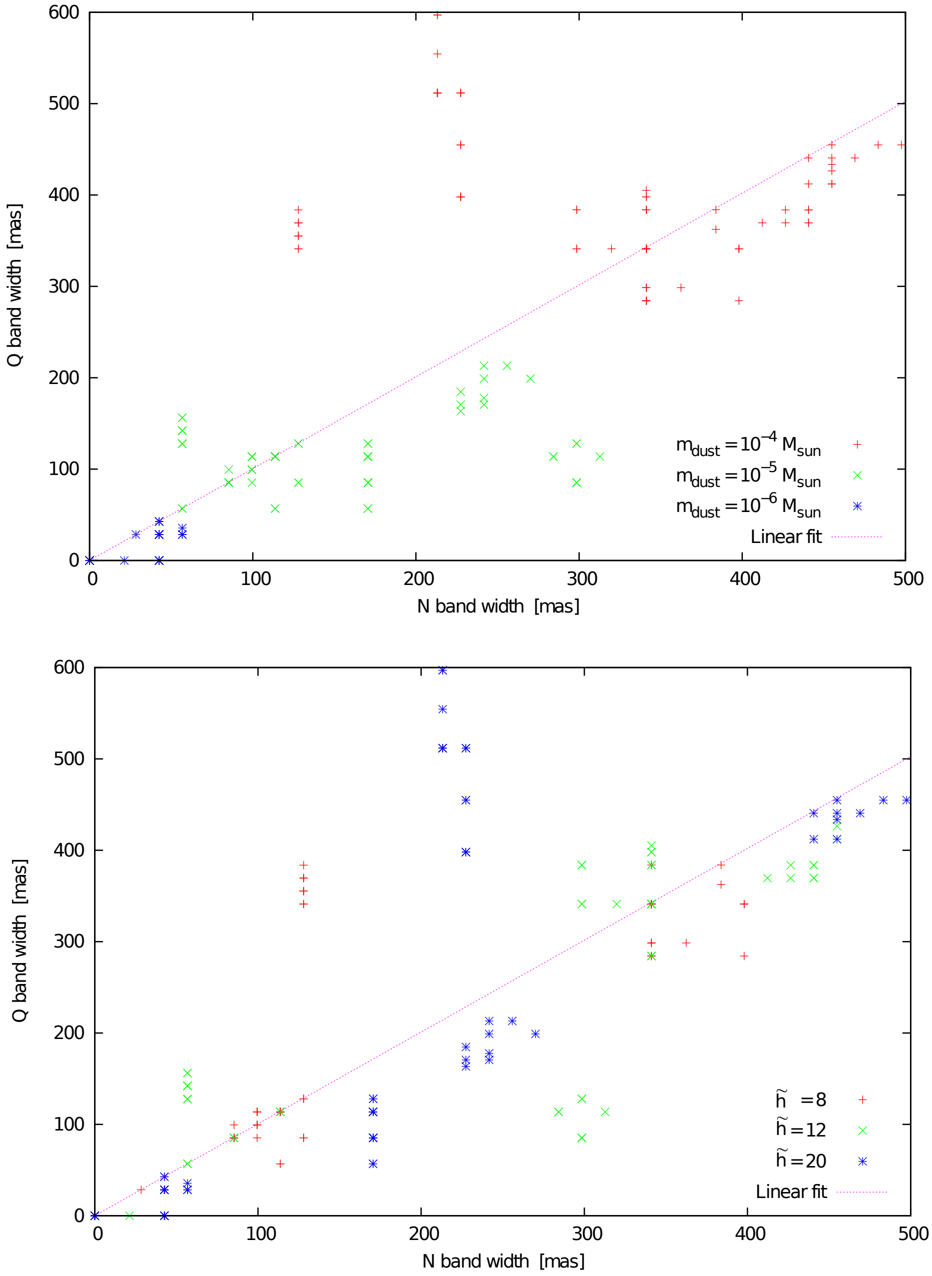

Figure 5.19.: *Top:* FWHM of the emission in N band versus the FWHM in Q band for the depletion parameter $\epsilon = 1.0$.
Bottom: FWHM of the emission in N band versus the FWHM in Q band for the depletion parameter $\epsilon = 1.0$. Colour coded are models with different relative scale heights $\tilde{h}$.

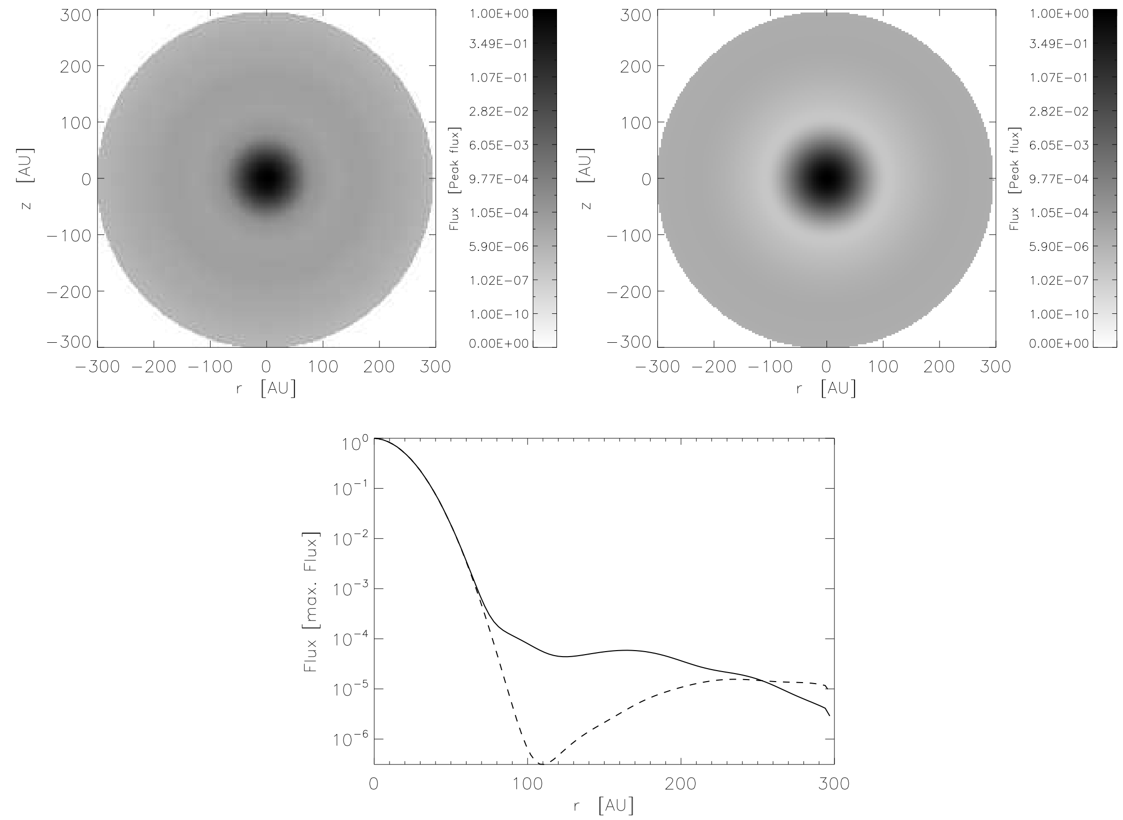

Figure 5.20.: Face-on images in the N band and radial profiles of the brightness distribution.
Top left: Fiducial model with a scale height relation of $\tilde{h} = 8$.
Top right: Fiducial model with a scale height relation of $\tilde{h} = 20$.
Bottom: Radial profiles. The solid lines corresponds to the first image, the dashed line to the second. All images have been convolved with a PSF of 30 AU. The colour scale is chosen as $\sim S_\nu^{0.1}$.

higher altitudes from the midplane than in the Q band. For $\tilde{h} = 20$ and small radii, the emitting region is below the $\tau_{\mathrm{Q}} = 1$ isoline. This leads to a more dimmed emission in the N band for middle radii which results in the brightness gap at these radii. The isolines are just indicating how deep face-on observations penetrate into the disc. Wien's law only allows to determine those grains and disc layers which emit most efficiently in a given wavelength band Schegerer *et al.* (2006). Many more grains with lower or higher temperature can also provide the dominating flux at the wavelengths in question. However, in Figure 5.21 all regions with higher temperatures are included by the temperature contour lines. Considering that the emitted energy is proportional to $\sim T^4$, the reasoning in the previous paragraph remains robust.

Figure 5.22 shows that the contrast of the brightness gap is a function of the relative

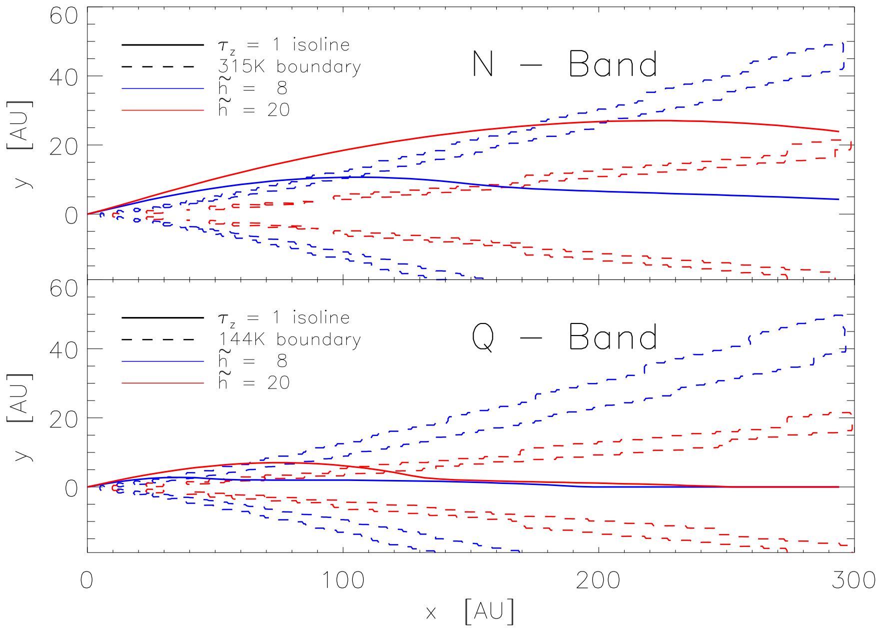

Figure 5.21.: Temperature distribution and isolines of constant optical depth $\tau = 1$ in the N band *(top)* and Q band *(bottom)* for the fiducial model. Different colours refer to different relative scale heights $\tilde{h}$. Note the inclusion/exclusion of the 315K - emission region in the N band of the large-grain population.

scale height for two thirds of the parameter space. Plotted is the total brightness minimum in units of the average disc brightness in the outer third of the disc versus the minimum brightness in the outer third of the disc also in units of the average outer disc brightness. Models featuring a gap have a flux minimum within the first two thirds of the disc and are located left of the line with unity slope. Models without an inner gap appear on the line with unity slope.

The gap is typically located at radii $r \approx 100\,\mathrm{AU}$. Discs with an outer disc radius of $r_{\mathrm{out}} = 100\,\mathrm{AU}$ consequently do not exhibit a gap. In Figure 5.22, these discs are all located on the line with unity slope. The width of the gap is readily defined as the radial distance between the location of the first brightness maximum after the gap and the location where the brightness distribution close to the centre reaches the maximum value. Figure 5.23 shows the minimum flux in the gap as a function of this gap width.

Models with very pronounced gaps are thus located in the lower right part of the plot. Shown are models with different values of $\tilde{h}$. The strength of the gap does not correlate with $\tilde{h}$ as can be seen from Figure 5.23. Yet, the width of the gap does. The analysis further shows that the gap width does not correlate with the outer disc

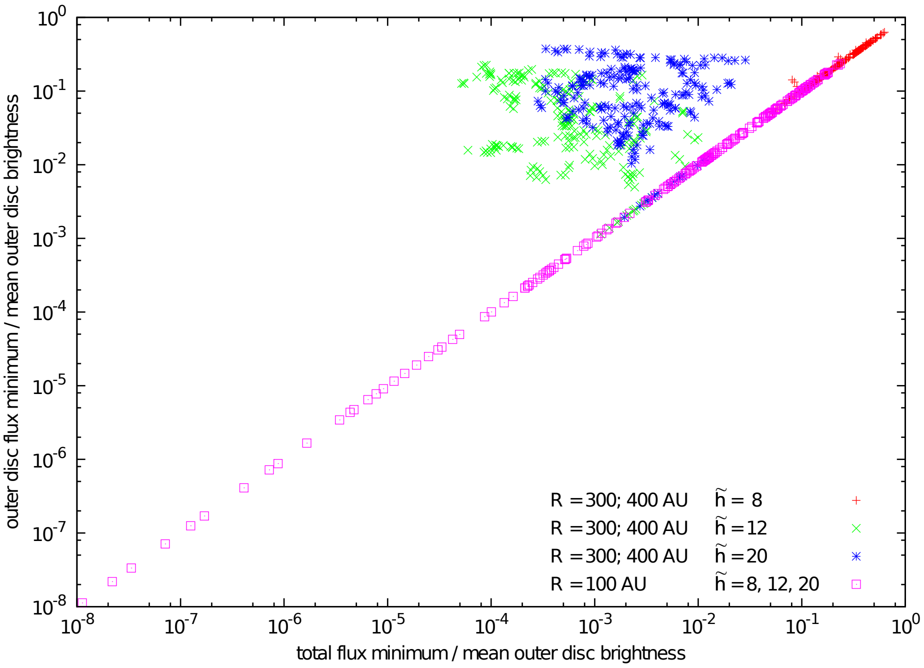

Figure 5.22.: Classification of the apparent gap in the brightness distribution of edge-on seen in the N band. Shown is the total brightness minimum in units of the average disc brightness in the outer $^1/_3$ of the disc versus the minimum brightness in the outer $^1/_3$ of the disc. Colour coded are model sets with different parameter values.

radius r_{out}.

5.3. Other markers: Discussion

A further result of this Chapter is that markers others than those presented in Section 5.2 are not sufficient to constrain grain growth and coagulation. Their discussion is the subject of this section in order to shed further light on the nature of the images of circumstellar discs.

5.3.1. Radial profiles in the millimetre regime at low inclinations

The observed flux in (sub-)millimetre images stems from dust grain re-emission at these long wavelengths. The optical depth is small rendering all dust particles visible. As all models are rotationally symmetric, it suffices to consider the radial brightness profile instead of the whole image.

However, those profiles do not provide means by which discs at different stages of their evolution could be distinguished. While the absolute value of the radial profile

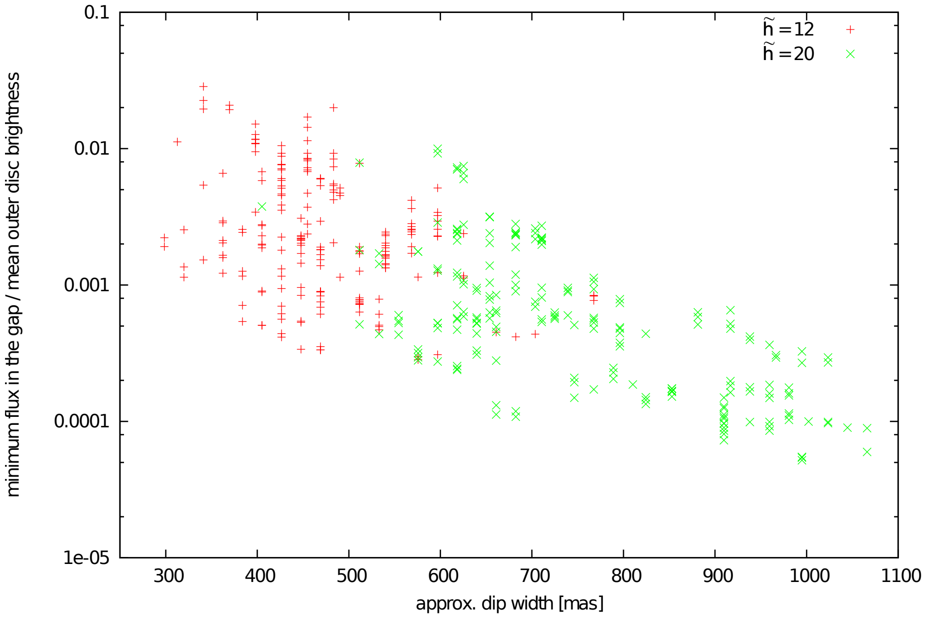

Figure 5.23.: Classification of the brightness gap of face-on seen discs at $\lambda = 10\,\mu$m. Plotted on a log-linear scale is the total brightness minimum in units of the average disc brightness in the outer $^1/_3$ of the disc versus the gap width. Colour coded are models with different scale height relation $\tilde{h}$. Models featuring $\tilde{h} = 8$ do not exhibit a gap, see Figure 5.22.

of the surface brightness distribution depends on the evolutionary stage of the disc, the shape of the profile does not. Figure 5.24 illustrates the situation. This renders the radial profile for $\theta < 90°$ degenerate with respect to m_{dust} and ϵ. This behaviour agrees with the findings of Section 5.2.2.

5.3.2. Dust lane chromaticity in the near-infrared

In the near-infrared, the typical appearance of a circumstellar disc seen edge-on is a bipolar structure that is intersected by a dark lane. The width of the dark lane is an effect of optical depth and wavelength dependent. In addition, at wavelengths between $2\,\mu$m and $10\,\mu$m, radiation due to thermal re-emission of the dust grains becomes increasingly important in the disc models and is in the mid-infrared by far the dominant contributor to the total flux.

As the optical depth is a function of the disc mass, one expects the width of the dark lane to be dependent also on the depletion of the upper disc layers. As grains grow and rain down towards the midplane, the upper layers become less opaque and might affect the width of the dark lane as an indicator for ϵ. Increasing the observing wavelength unveils deeper layers in the disc and the large dust gain population (cf.

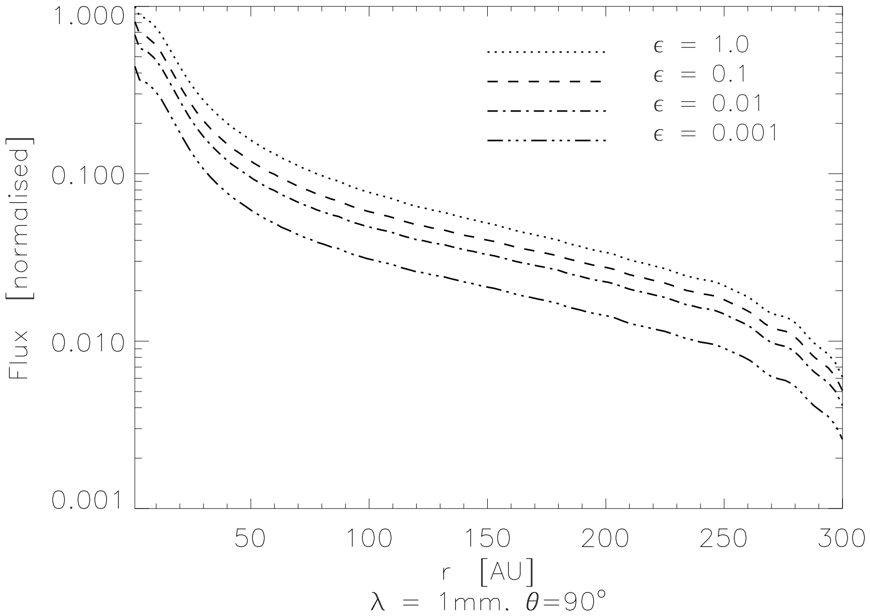

Figure 5.24.: Radial profiles of the fiducial disc model at different evolutionary states. As the disc evolves, the absolute value of the radial profile changes; however the intrinsic shape does not.

Figure 5.12) increasingly influences the appearance of the disk. Figure 5.25 shows the width of the dark lane for the fiducial model. As expected, the width of the dark lane decreases with both, wavelength and with progressing depletion of the upper disc layers. The chromaticity itself is a function of ϵ (otherwise the fitted lines would be parallel): For smaller ϵ the chromaticity of the dark lane is less steep.

Moreover, the chromaticity's dependence on ϵ provides means to identify dust grain growth and settling uniquely via near- to mid-infrared imaging only. In Figure 5.26 all chromaticity slopes m_ϵ for all possible parameter combinations are given. For any given ϵ, the slope obtained is either zero or scatters within a certain range. The depletion of the upper disc layers could be inferred from the slope if a unique relation between ϵ and the chromaticity slope could be observed. This is not the case.

The same behaviour is observed when not only images in the I, J, H, and K bands but also in the L and M bands are considered. These two bands mark the transition region between images dominated by scattered stellar light and dust grain re-emission. This is independent of the resolution used to image a given circumstellar disc in the NIR.

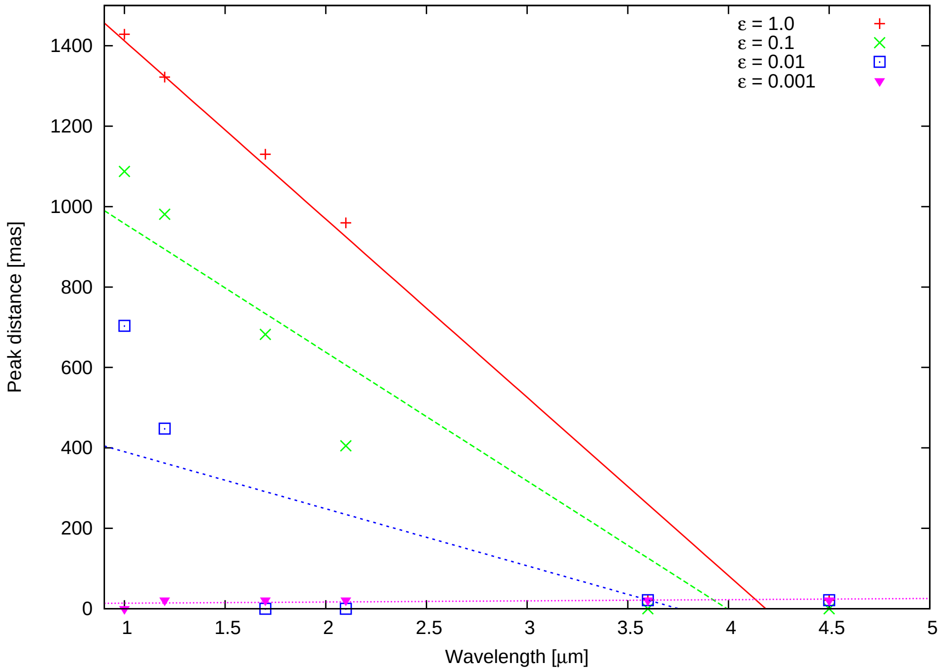

Figure 5.25.: The chromaticity and dependency of the width of the dark lane on the depletion of upper disk layers in the NIR wavelength regime. For longer wavelengths and smaller ϵ the width is generally smaller. Shown also are straight line fits.

5.3.3. Combining near-infrared and millimetre images

One might expect that a combination of millimetre images and near-infrared images yields tracers for dust grain growth and sedimentation just as the combination of images in the N and Q. Figure 5.27 gives the relation between the FWHM of the vertical extend of the spatial brightness distribution in the millimetre regime and the width of the dark lane in the J Band. The high dust densities in the disc midplane are responsible for the dark lane in the NIR and the elongated spatial brightness distribution in the millimetre regime. Thus, a relation between the width of the dark lane and the millimetre emission region could hint to the disc's evolution. However, as Figure 5.27 shows, no correlation between the two quantities is observable.

5.3.4. Degeneracy between parameters and panchromatic studies

It is important to point out that if all disc parameters in the parameter-space are known, in most cases the chromaticity of the dark lane determines the evolutionary state, as illustrated by the fiducial model (cf. Section 5.2.1). In general, it is not possible, though, to determine the evolutionary stage of a disc when other parameter

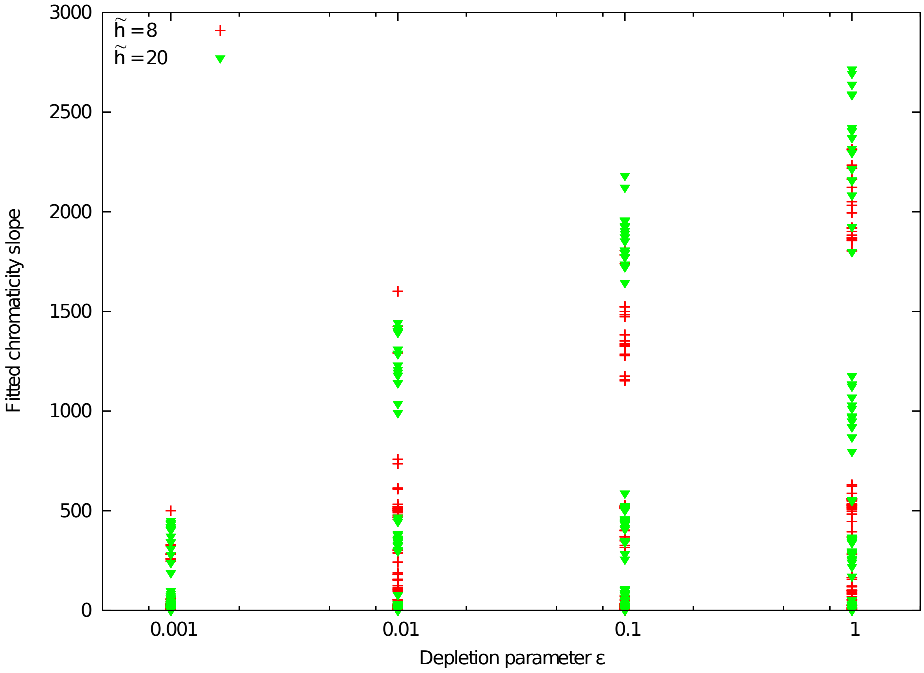

Figure 5.26.: Scatter plot of the chromaticity-slope of the dark lane for different ϵ and different fit ranges.

values remain unconstrained as well.

As a simple counter-example, consider a system that is optically thin at all near-infrared wavelengths, and thus a dark lane is not visible and no chromaticity can be seen. In the current framework, his happens for discs with either a low total dust mass, a low scale height relation $\tilde{h}$, a high depletion parameter ϵ, or combinations thereof. The total dust mass can be constrained by the systems' total flux in the millimetre regime where the disc is generally optically thin. However, to constrain $\tilde{h}$ a certain total dust mass is required. Otherwise the effects of $\tilde{h}$ are rendered indistinguishable.

5.3.5. The general face-on case

As shown for millimetre images in Section 5.2.2, the ability to constrain dust sedimentation by single imaging is lost for $\theta < 90°$. For images in the near-infrared and mid-infrared the situation is similar. In Figure 5.28 shows plots of the FWHM of the disc's brightness distribution seen edge-on at different wavelengths.

At short wavelengths, the emission region is very small as in the NIR the star is the dominant contributor to the image flux. Images exhibit an apparently broader flux distribution at larger wavelengths since the origin of the observed flux shifts from scattering to re-emission. The size of the re-emission regions growths as the observing

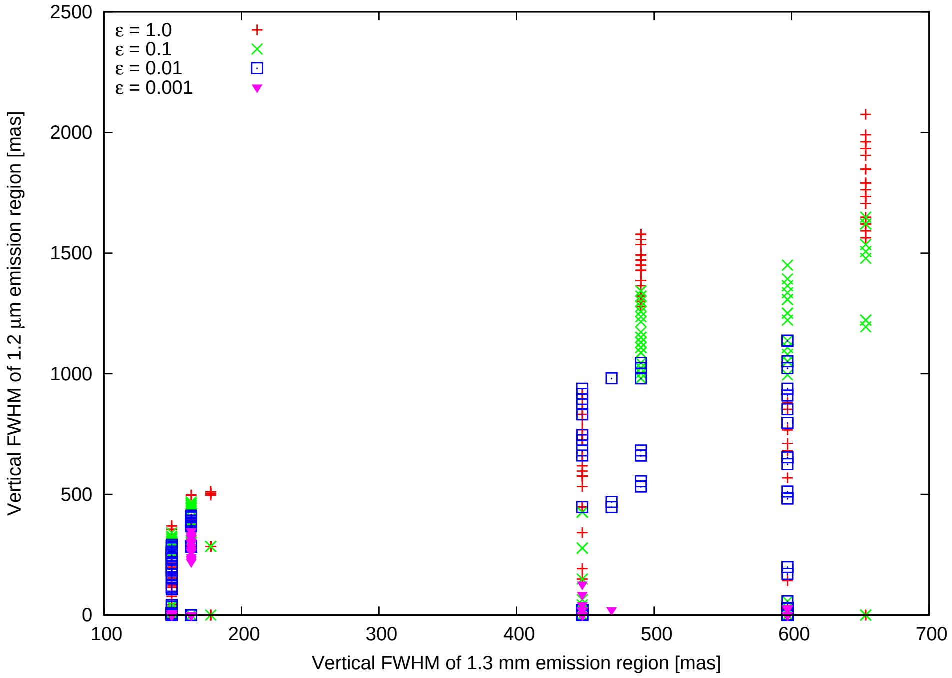

Figure 5.27.: Width of the dark lane as function of the FWHM of the millimetre emission. Colour coded is the depletion parameter ϵ. A clear dependency between ϵ and the width of both is not seen.

wavelengths gets larger and cooler parts become more important contributors.

Whereas in Figure 5.18 a grouping of data points with smaller ϵ to a linear relation between the N and Q band emission width can be observed, no such relation can be found in Figure 5.28.

This observation does not contradict the findings of Dullemond & Dominik (2004). In this work, dust grain growth and sedimentation have not been modelled with a parametrised model but including radius dependent sedimentation. The present model framework does not allow for radial depended dust settling. Quicker dust grain growth at smaller radii renders the upper disc layers in the inner disc more transparent and allows to heat the outer disc more efficient. The radial brightness profile would be shifted and/or spread outward. In contrast, the upper layers deplete all at the same rate in in the present models. Hence the radial brightness profile is unaltered.

The latter is only true for the relative profile, that is a profile normalised to some other disc inherent quantity. For most practical reasons this would be the total disc flux. The absolute value of fluxes changes with a the evolution of the disc (cf. Section 5.3.1).

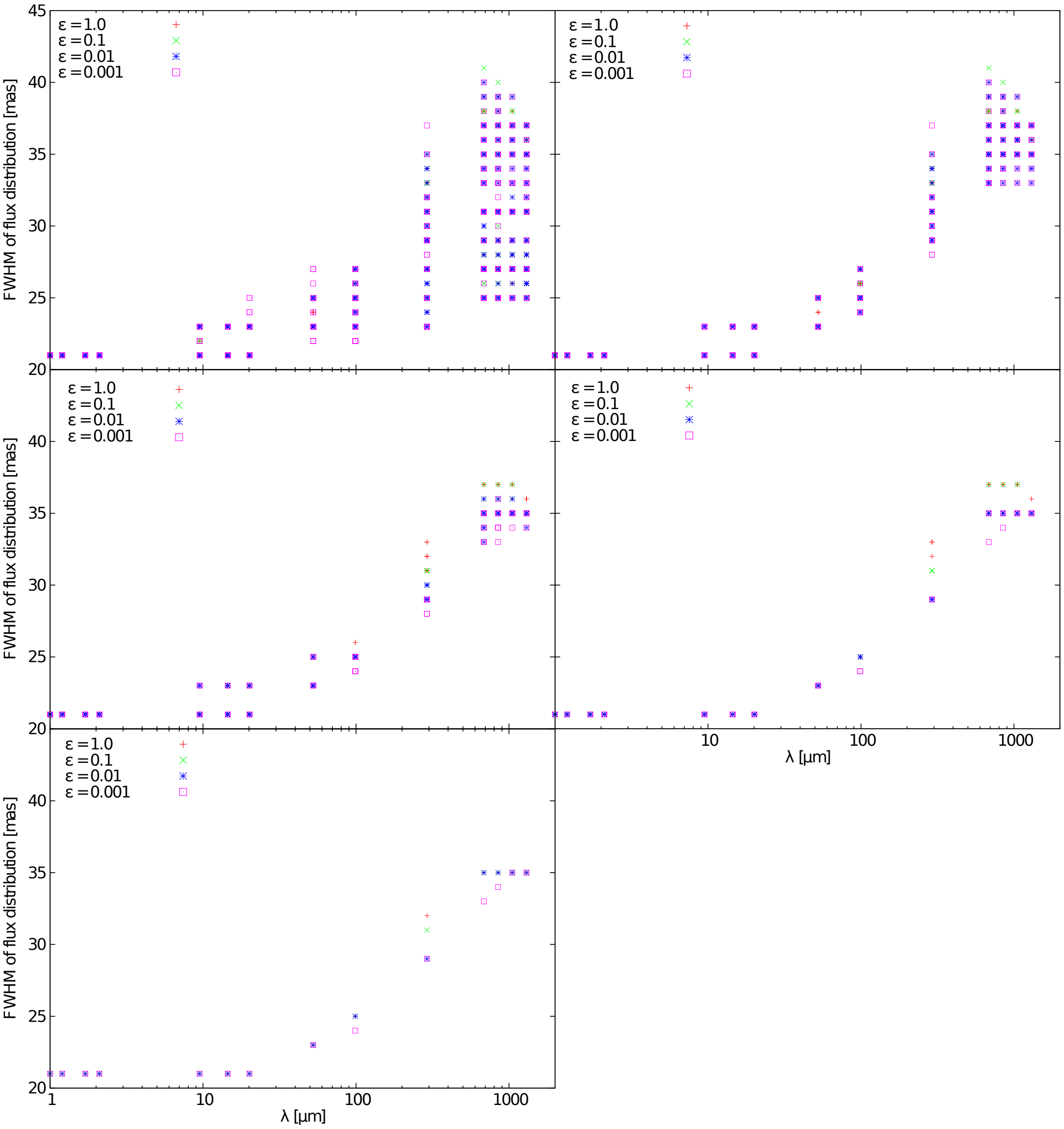

Figure 5.28.: The FWHM of the spatial intensity distribution of a disc observed face-on as function of the wavelength. The FWHM of the spatial intensity distribution of disc observed face-on as function of the wavelength λ and the depletion parameter ϵ. Starting at the top left plot an increasing number of disc parameters are kept fixed, starting with just one and ending up with five fixed parameters in the bottom plot. Hence, a respectively smaller subspace of the original parameter space is considered. Yet, no correlation between ϵ and the FWHM can be seen.

6. Observing trapped dust

> Εἰ οὖν διαλέγεσθαι οἷοί τ’ εἶεν πρὸς ἀλλήλους, οὐ ταῦτα
> ἡγῇ ἂν τὰ ὄντα αὐτοὺς νομίζειν ἅπερ ὁρῷεν;
> ἀνάγκη.
>
> *(Platon*, Πολιτεία*)*

In the previous Chapter, markers of dust grain growth and sedimentation have been identified in a very general model framework. The focus of this chapter, however, are the observational consequences of one specific model. Whereas previously parametrised disc models and growth/sedimentation descriptions have been used, now a dynamic and self-consistent model forms the basis of the investigation and the radiative transfer calculations.

6.1. The drift barrier and dead zones

As already hinted in section 2.2, there are several barriers apparently prohibiting dust grain growth from ISM-sized grains to several meter-sized objects. The radial drift barrier is due to the fact that circumstellar discs are pressure stabilised against the star. Therefore, they do not rotate with exactly Keplerian speed but sightly slower. Dust grains do not feel gas pressure and hence are due to orbit with Keplerian rotation. Consequently, each dust grain feels a continues head wind v_{rel} that translates via Equation (2.7) into a drag force. The grain thereby loses angular momentum and moves closer to the star as the rotation velocity of the gas increases monotonically for decreasing radii. If this mechanism is not stopped, the grain ultimately is lost to the star.

One possibility to circumvent the radial drift barrier might be the trapping of dust grains in local maxima of the disc gas pressure as discussed by Klahr & Lin (2001); Klahr & Henning (1997); Kretke & Lin (2007), and Brauer *et al.* (2008b). In this Chapter, only radial maxima are considered as the disc is assumed to be rotational symmetric. Dust grains drift towards maxima of gas pressure in discs. This can be understood by considering the respective pressure gradient $\partial_r p$ of the gas. Assuming that the pressure maxima is located at r_{trap}, then the gas at $r < r_{\mathrm{trap}}$

feels an additional force due to $\partial_r p$ towards the central star. As a consequence, the gas at slightly smaller radii than r_{trap} rotates slightly faster since the effect of the additional force is the same as a gravitational force. At $r > r_{\mathrm{trap}}$, the situation is the other way round. The pressure gradient $\partial_r p$ now points away from the star effectively decreasing its gravitational potential and causing a slightly less rapid rotation. As a result of this pressure maxima at r_{trap}, the rotation speed of the gas is no longer a monotonic function but features a local minimum slightly outside r_{trap}. Hence, grains of a certain size do no longer experience a head wind v_{rel} and according to (2.7), also no drag force and thus do not loose angular momentum. That is, they stay at their respective radius, i.e. they are ‘trapped’. Additionally, the relative dust grain velocities are much lower in such traps, offering thereby a possibility to avoid the fragmentation barrier as well.

One possible cause for local pressure maxima are local gravitational instabilities as discussed by Johansen *et al.* (2007) or the presence of an evaporation front (e.g. the snow line) (Kretke & Lin, 2007). In this thesis, another cause for local maxima is assumed, namely dead zones, as investigated by Dzyurkevich *et al.* (2010).

As discussed in Section 2.1, the precise nature of the viscosity $\tilde{\nu}$ in circumstellar discs is yet unknown. A candidate for the origin of the viscosity is the magneto-rotational instability. In order for the MRI to work, the presence of ions within the discs is required. The typical temperatures in a circumstellar discs are considerably low (cf. Figure 3.5), only some 10 to 1000K. Hence, the main source for these ions ought not to be seen in thermal ionisation of the gas but in cosmic rays and stellar X-rays. If these rays do not penetrate the entire disc, because of optical thickness in the respective wavelength, then there will be regions of the disc, where the MRI is not able to operate as no ions are available. These regions are called dead zones. Naturally, dead zones are expected to be deep embedded in the disc around the midplane. Because of high-energetic stellar radiation, dead zones also do not extend entirely to the inner disc rim.

A consequence of dead zones is that the MRI-driven viscosity changes as function of radius. Close to the inner rim, $\tilde{\nu}_\alpha$ is a factor ≈ 100 larger as compared to regions with dead zones. Now, the mass transfer in the disc, the accretion rate $\dot{M}$, is understood to be constant in the disc. This in turn means, that a change in $\tilde{\nu}_\alpha$ causes the opposite change in the surface density Σ, since $\dot{M} \sim \tilde{\nu}_\alpha \Sigma$. Thus, if the viscosity decreases at some radius r_{trap}, then Σ, and hence p, increase. In this manner, dead zones might be able to provide for a local pressure maximum that is able to prevent dust grains from spiralling into the central star and allow them to grow to planetesimal seeds.

6.2. The model with pressure maxima

The model used to investigate the observational consequences of dust grain trapping is not a parametrised disc as in the other Chapters of this thesis. Instead, the results

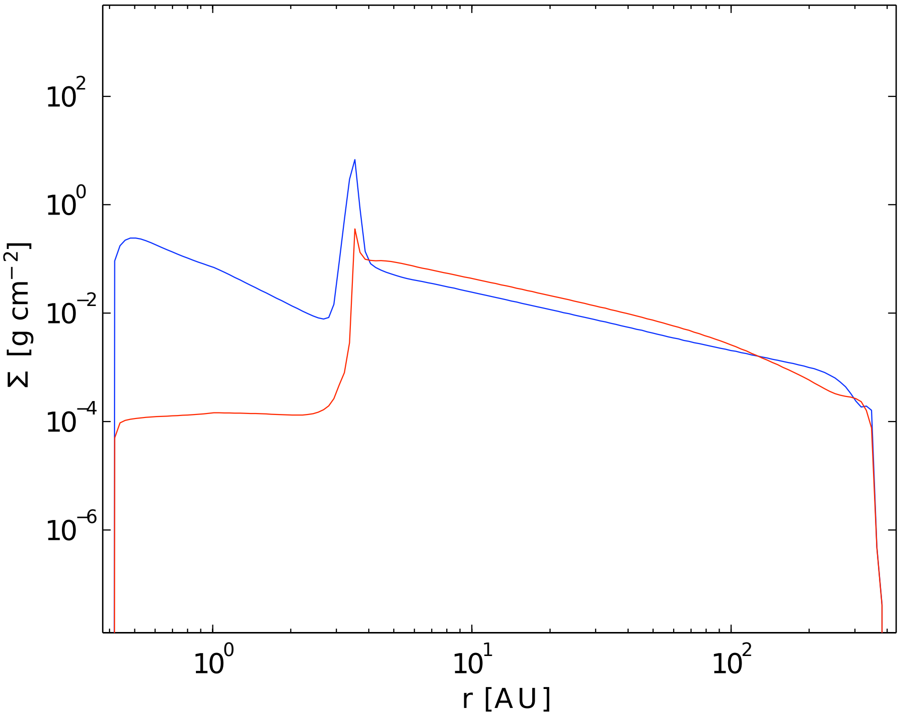

Figure 6.1.: Surface density as function of radius of the disc model with $r_{\mathrm{trap}} = 3\,\mathrm{AU}$ at $t = 10^5\,\mathrm{yr}$ for different fragmentation velocities. Shown in blue is the disc model with $v_{\mathrm{frag}} = 1\ {}^{\mathrm{m}}/_{\mathrm{s}}$ and in red $v_{\mathrm{frag}} = 5\ {}^{\mathrm{m}}/_{\mathrm{s}}$. See also Figure 6.2.

of the gas and dust evolution code by Birnstiel *et al.* (2010a) are being used. This dust coagulation and fragmentation code is an enhancement of the work of Brauer *et al.* (2008a) that also includes the time-dependent viscous evolution of the disc which is important for the incorporation of dead zones. Magnetohydrodynamical computations are not the scope of this code and the effects of dead zones on the viscosity $\tilde{\nu}_\alpha$ are incorporated by virtue of the α_ν parameter (cf. Equation (2.1)) which is set to $\alpha_\nu = 10^{-3}$ for $r < r_{\mathrm{trap}}$, where the MRI is to operate. Within in the regime of dead zones, at $r > r_{\mathrm{trap}}$, the viscosity is set to $\alpha_\nu = 10^{-5}$. The location of the pressure maximum is set to $r_{\mathrm{trap}} = 3\,\mathrm{AU}$, as obtained by Dzyurkevich *et al.* (2010). As a reference, the location at $r_{\mathrm{trap}} = 30\,\mathrm{AU}$ is also subject of the investigation.

Particles encountering each other with a relative velocity v_{rel} are considered to fragment, if $v_{\mathrm{rel}} > v_{\mathrm{frag}}$, while particles with $v_{\mathrm{rel}} < v_{\mathrm{frag}}$ coagulate or fragment with a certain probability. Here, v_{frag} is the critical fragmentation velocity. In the scope of this Chapter, $v_{\mathrm{frag}} = 1\ {}^{\mathrm{m}}/_{\mathrm{s}}$ and $v_{\mathrm{frag}} = 5\ {}^{\mathrm{m}}/_{\mathrm{s}}$ have been studied. The different values for v_{frag} have implications for the maximum grain size a_{max} that can be found in the

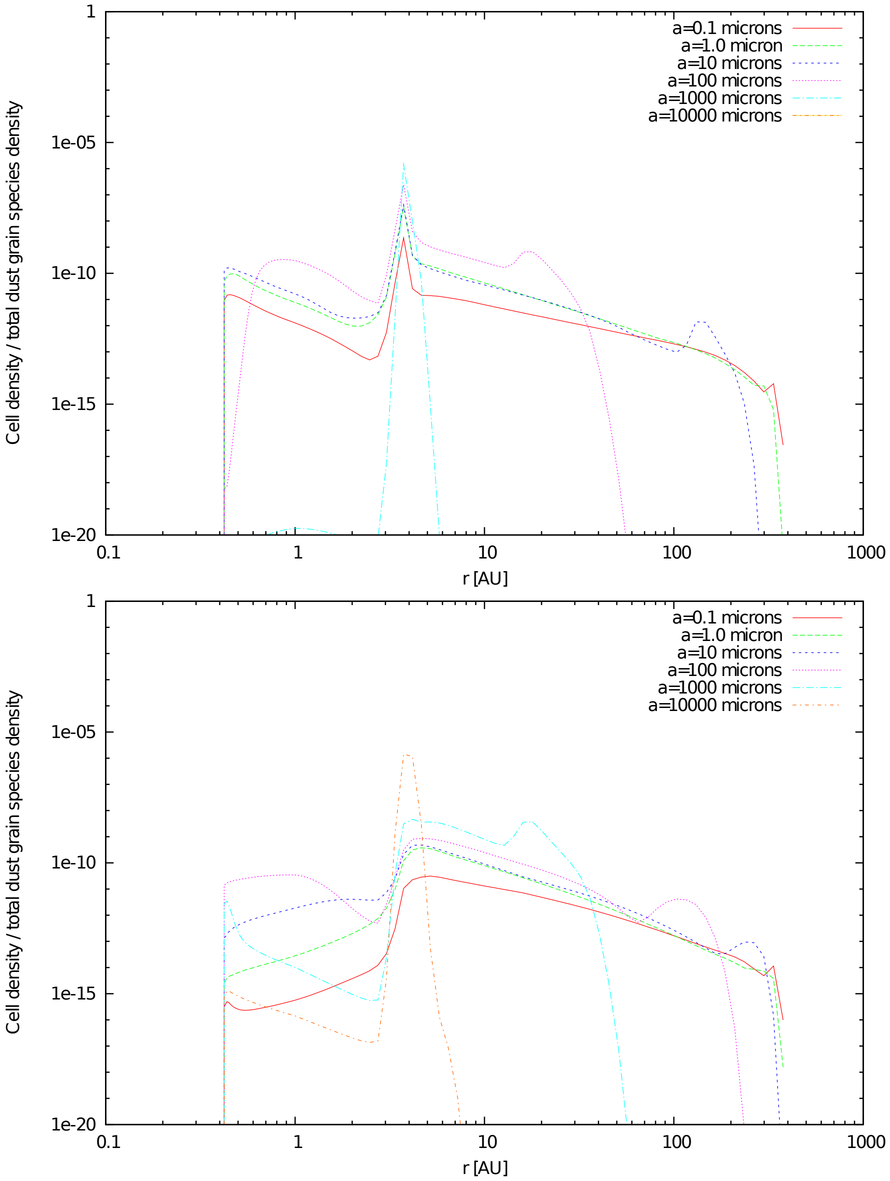

Figure 6.2.: Relative dust composition in the disc midplane with respect to grain sizes. Only selected grain sizes are shown. The pressure maximum is located at $r_{\mathrm{trap}} = 3\,\mathrm{AU}$ in these models. *Top:* $v_{\mathrm{frag}} = 1\ ^{\mathrm{m}}/_{\mathrm{s}}$. *Bottom:* $v_{\mathrm{frag}} = 5\ ^{\mathrm{m}}/_{\mathrm{s}}$.

disc. This is because the relative dust grain particle speed increases with the grains' size:

$$a_{\max} \sim \frac{\Sigma}{\alpha_\nu c_{\mathrm{s}}^2}\, v_{\mathrm{frag}}^2, \tag{6.1}$$

as shown by Birnstiel *et al.* (2009). Here, c_{s} is the sound speed. If the grains are to survive collisions up to $v_{\mathrm{frag}} = 5\ {}^{\mathrm{m}}\!/_{\mathrm{s}}$, then larger grains are present in the disc and in the pressure trap. As a consequence, the composition of the dust in the disc changes. Figure 6.2 depicts the relative abundance of dust grains with selected sizes in the disc midplane.

Of course, not all dust grains are trapped by pressure maxima, as turbulent radial mixing is also accounted for. Hence, some dust grains break through the pressure maxima and are lost to the star. Discs with large dust grains are more prone to this mass loss as radial drift is more effective for larger grains. The disc mass for both models, with $v_{\mathrm{frag}} = 1\ {}^{\mathrm{m}}\!/_{\mathrm{s}}$ and $v_{\mathrm{frag}} = 5\ {}^{\mathrm{m}}\!/_{\mathrm{s}}$ is chosen such that their mass at $t = 10^6\,\mathrm{yr}$ is comparable ($\approx 5.7 \times 10^{-5}\,\mathrm{M}_\odot$).

The inner disc rim is set to $r_{\mathrm{in}} = 0.4\,\mathrm{AU}$ and the model space reaches to $r_{\mathrm{out}} = 4000\,\mathrm{AU}$. However, the radius of the disc only extends to $\sim 400\,\mathrm{AU}$. The gas-to-dust ratio is assumed to be 100 throughout the disc. The surface density exponent (cf. Equation (2.5)) is set to $p = -1$. The central object, that is also used to perform radiative transfer calculations, is a generic T Tauri star with a mass of $m_* = 1\,\mathrm{M}_\odot$ (see Section 2.1). In the simulations, the evolution of the disc is followed from $t = 10^3\,\mathrm{yr}$ to $t = 10^6\,\mathrm{yr}$. Starting at $t = 10^5\,\mathrm{yr}$, the model is investigated every $t = 10^5\,\mathrm{yr}$. The model operates with vertically integrated quantities, such as Σ (instead of ρ). In order to provide a 3D model for the radiative transfer calculations, hydrostatic equilibrium vertical to the midplane is assumed to derive the gas pressure scale height. As discussed by Dullemond & Dominik (2004), this determines a respective sedimentation height for a dust grain of given size a which is used as the dust scale height.

6.3. Observational consequences for millimetre images

The question answered in this Chapter is whether the mechanism to enable dust grain growth as presented in Section 6.1 and implemented as described 6.2 has observational consequences. For two reasons, the natural place to look for these are face-on images of the disc described by the models in the millimetre regime. Figure 6.3 shows such an image, representatively.

The first reason for this wavelength range is that in the millimetre wavelength regime the spectral slope can be used as a tracer for the largest dust grain present, as discussed in section 2.3.2. Figure 6.2 shows that the composition of the dust is different at the pressure maximum. Especially, it is there that the largest grains are found in the disc while at other locations of the disc a_{max} is considerably smaller.

The second reason is that, as already demonstrated in Chapter 3, discs in the millimetre regime are typically optically thin. As a consequence, it is possible to trace all the dust grains at these wavelengths. In contrast, shorter wavelengths only probe the upper dust layers due to the optical depth. As the sedimentation time scale is rather short and hence small dust grains are relatively more dominant in

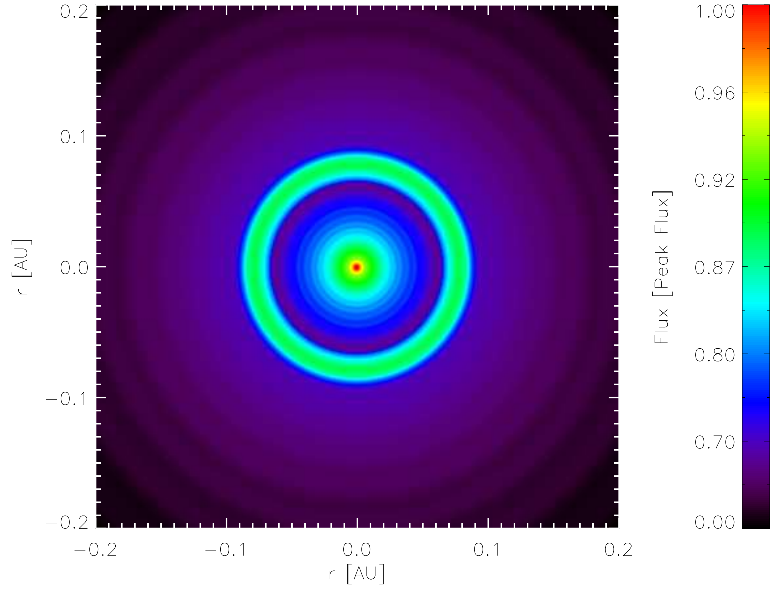

Figure 6.3.: Zoom-in image of a disc model with $r_{\mathrm{trap}} = 30\,\mathrm{AU}$ at $t = 2 \times 10^5\,\mathrm{yr}$ for $v_{\mathrm{frag}} = 1\ {}^{\mathrm{m}}\!/_{\mathrm{s}}$ as seen with an observing wavelength of $\lambda = 1.3\,\mathrm{mm}$. The colour scale is not linear but scales as $\sim S_\nu^{\frac{1}{5}}$.

these layers despite that large dust grains might be trapped at the respective radius in the midplane, well hidden from sight.

6.3.1. Optical depth structure

Since the mechanism of dust grain trapping is dependent on radius, edge-on observations are not suited to trace pressure maxima. Lines of sight in the millimetre pierce through the dust distribution at all radii if the disc is seen with $\theta = 90°$. This would render the specific effect of the various grain size composition as a function radius moot as the position information is lost.

Figure 6.6 shows an analysis of the optical depth structure of the models used in this Chapter. The columns refer to different values of v_{frag} and the dashed/solid line to different locations of the pressure maximum. Shown are the values of the optical depth at the midplane as well as the $\tau_\lambda = 1$ isosurface. Also plotted are the relative grain abundances at the midplane and at the location of the $\tau_\lambda = 1$ isosurface. The latter is interesting, as this is generally the location of the deepest embedded parts of the dust disc that still contribute to the flux seen in the face-on images. Especially at larger radii, the optical depth does not even reach values as high as $\tau_\lambda = 1$ even at the considered wavelength $\lambda = 330\,\mu\mathrm{m}$. There, the location of the isosurface (red

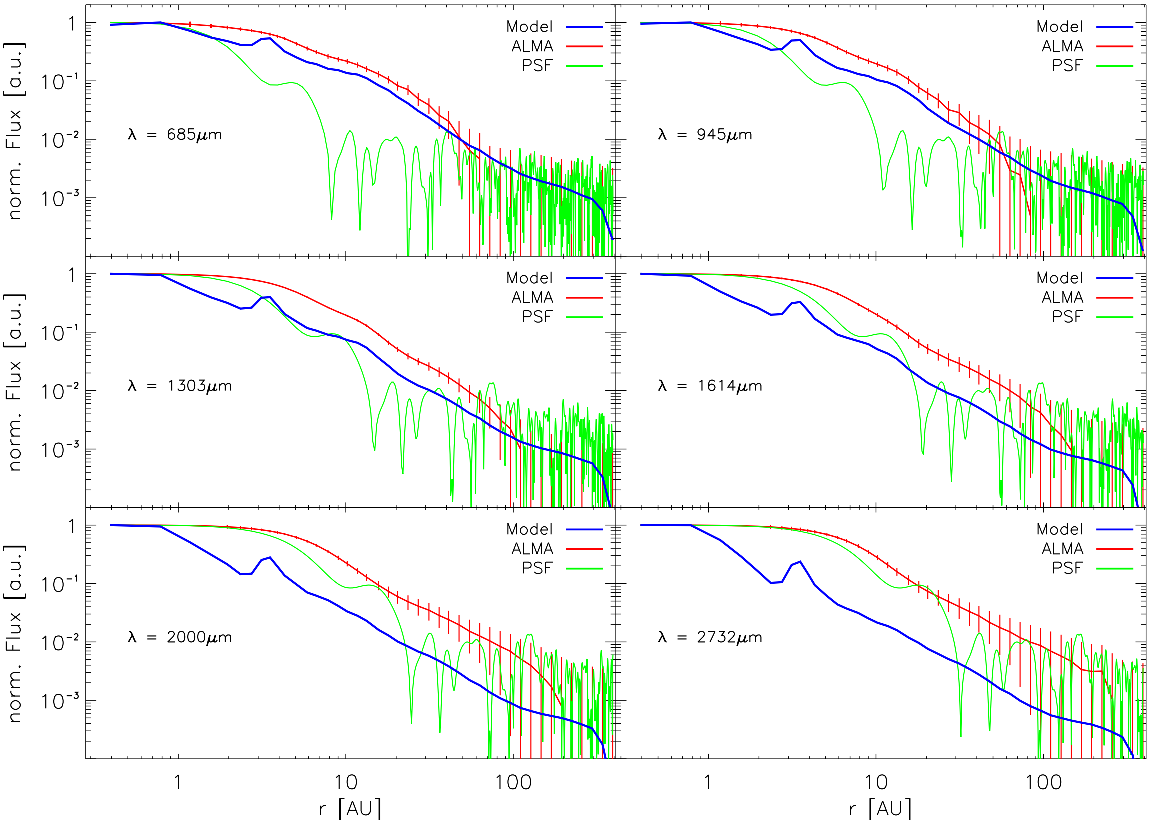

Figure 6.4.: Radial flux profiles of a disc with pressure maximum at 3 AU. The flux scale is normalised to the peak value. Given is the fragmentation velocity $v_{\mathrm{frag}} = 1\ {}^{\mathrm{m}}\!/_{\mathrm{s}}$.

lines) cannot be determined any more and hence, at large radii they are not seen in the plot. The dust amounting in the pressure trap is not always dense enough to provide an optical depth ≈ 1, as a respective 'peak' for $v_{\mathrm{frag}} = 5\ {}^{\mathrm{m}}\!/_{\mathrm{s}}$ is missing for $r_{\mathrm{trap}} = 30\,\mathrm{AU}$ while it is clearly visible for $v_{\mathrm{frag}} = 1\ {}^{\mathrm{m}}\!/_{\mathrm{s}}$. As a consequence, the respective grain abundances cannot always be given in the second row of the plot. This is of course different in the last row, where the midplane relations are given.

As it can be seen, small dust grains are more often to be found in all disc model combinations. In contrast, the large grains are concentrated to the locations of the pressure maxima, either at the $\tau_\lambda = 1$ isosurface or in the disc midplane. This is fostering the idea that the slope α_{mm} of radially resolved SEDs are able to serve as observable tracers of trapped dust.

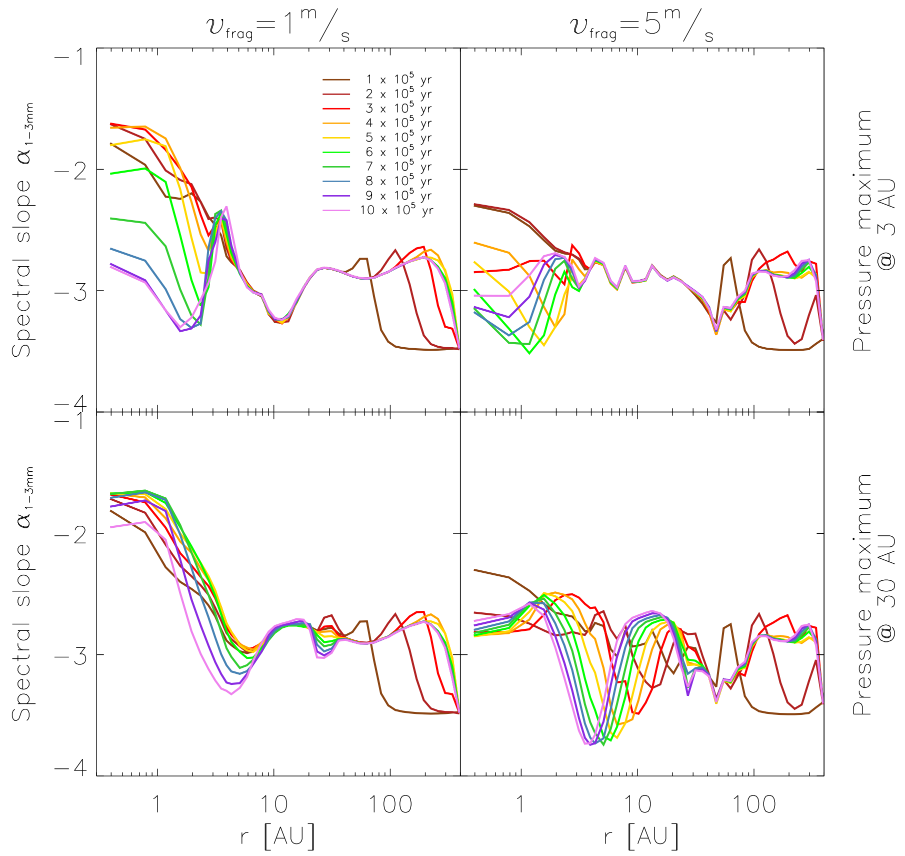

Figure 6.5.: Spectral slopes for different models at different times of their evolution (colour coded). The slopes result from 1.3mm and 2.7mm images.

6.3.2. Radial profiles and spectral slope

The discussion of SEDs and their slope in Section 2.3.2 referred to the SED of the complete object. However, this is not a necessary requirement. In fact, the properties of the millimetre slope α_{mm} apply naturally to any system with the respective low temperatures (Rayleigh-Jeans-Limit) and dust grain composition. Consequently, spatially resolved SED should be able to identify the specific dust composition of trapped dust. The composition outside the trap is not necessarily ISM-like. Hence, one cannot expect that the value of α_{mm} outside the pressure maximum drops to the ISM value of -4. Also, inside the trap in the model are not arbitrarily large grains (cf. Figure 6.2 *left*) which would yield $\alpha_{\mathrm{mm}} = -2$. These two values are just the borders in between which α_{mm} is to be expected, with (pronounced) larger values at the location of the pressure maximum.

Unfortunately, integral field spectrographic instruments such as VLT/SINFONI do not yet provide the spatial resolution that would allow to use them to get spatially resolved SEDs of a disc. Besides, SINFONI does not operate in the millimetre regime. Therefore, millimetre observatories such as ALMA are to be used to identify pressure maxima. Images of different wavelengths are to be taken and then the fluxes at the respective radii have to be compared in order to derive the required SED. As the disc is rotational symmetric, it suffices to consider the radial profiles of the images. Figure 6.4 shows the radial profile of the model at different wavelengths. The result of the pressure maximum translates into a local flux maximum due to larger number of dust grains. Also, this peak is more pronounced for larger wavelengths since the optical depth is lower there shielding less and less grains from sight.

6.3.3. The slope α_{mm} of different models

Figure 6.5 shows the slope α_{mm} for different values of v_{frag}. The slopes have been computed by using images at 1.3 mm and 2.7 mm. Flux values at these two values uniquely determine the spectral slope α_{mm}. Initially, more images at additional wavelengths have been used and α_{mm} has been determined by a fitting process. Fitting a line and a black body (to account for deviations from the Rayleigh-Jeans limit at shorter wavelengths), the results however have not been found to be more distinctive than those derived from using just two images.

In all models, the pressure maxima leave a clear footprint in the radial distribution of the spectral slope α_{mm} at the respective positions. As it is to be expected, the exact values for α_{mm} range in between the ISM value of -4 and -2, which indicates the presence of large bodies. The model with the pressure maximum located at $r_{\mathrm{trap}} = 3\,\mathrm{AU}$ and $v_{\mathrm{frag}} = 1\ {}^{\mathrm{m}}/_{\mathrm{s}}$ exhibits the most pronounced peak. While at $r = r_{\mathrm{trap}}$ the values for α_{mm} are ≈ -2.4, most parts of the disc show $\alpha_{\mathrm{mm}} > 3$. At early stages of the disc's evolution, inside r_{trap} similar values for α_{mm} are reached as for $r = r_{\mathrm{trap}}$. The reason for this is to be seen in the respective viscous evolution time scales of the disc regions. Initially, the disc has a homogeneous distribution of dust grains, that is subject to change in time. The large grains present at small radii initially are lost due to the star because of radial drift as these grains cannot be caught in the pressure maximum. The same observation can be made in the model with $r_{\mathrm{trap}} = 3\,\mathrm{AU}$ and $v_{\mathrm{frag}} = 5\ {}^{\mathrm{m}}/_{\mathrm{s}}$. Although the peak in the radial distribution of α_{mm} is less pronounced due to the clearing of the the region $r < r_{\mathrm{trap}}$, it is also well visible.

Signature of pressure maxima at 30 AU

The issue is a little different if the pressure maximum is located further outside at 30 AU. For $v_{\mathrm{frag}} = 1\ {}^{\mathrm{m}}/_{\mathrm{s}}$, there is a well-pronounced peak of the spectral slope for radii between $\approx 10\,\mathrm{AU}$ and $\approx 20\,\mathrm{AU}$, a little further inside than the jump in the viscosity parameter α_{ν} that was used to mimic the effect of dead zones. Clearly, this does not directly translate into the location of the dust trapping spot. This is also

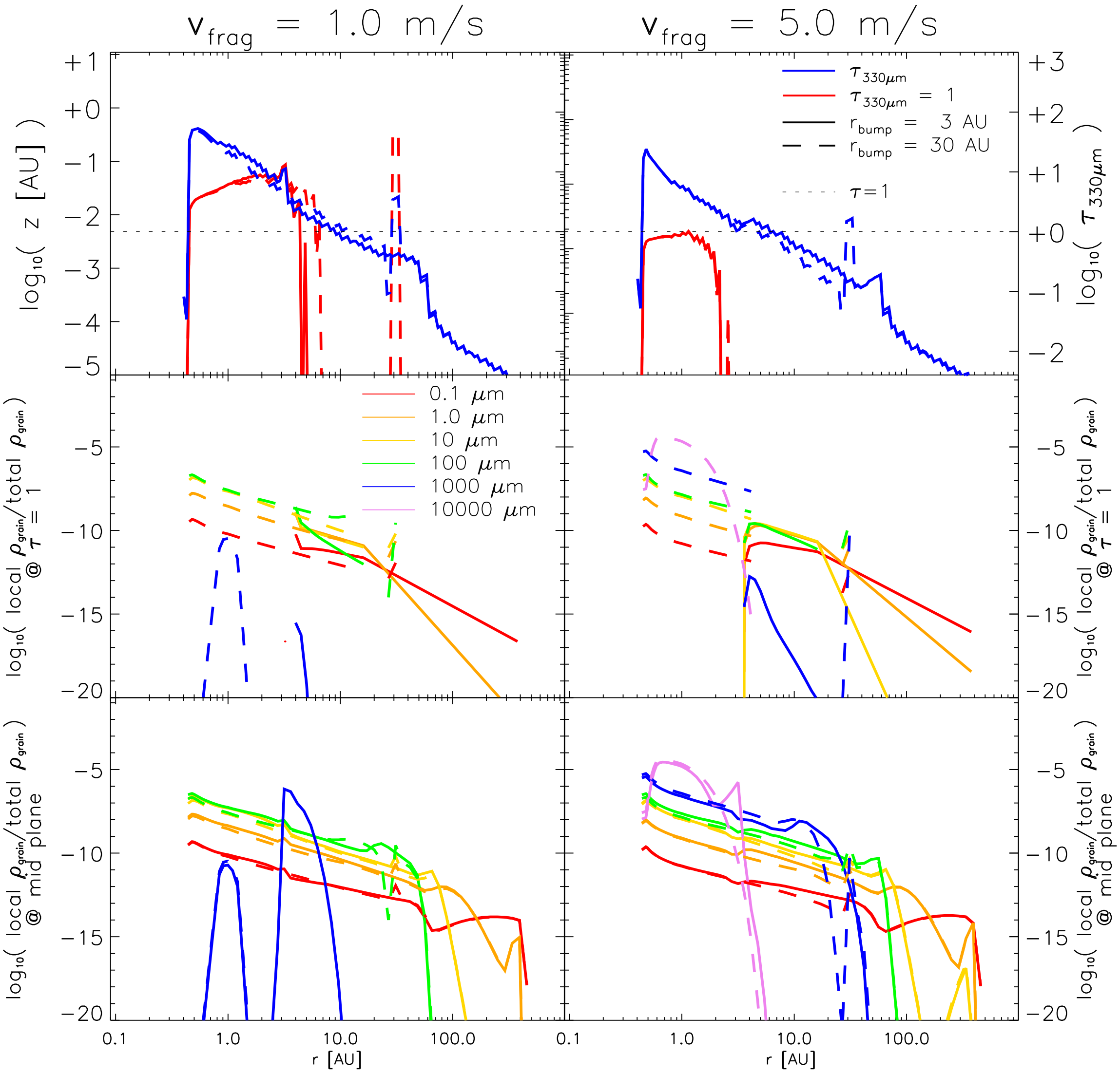

Figure 6.6.: *Top row:* Analysis of the optical depth structure of the models in this Chapter. Shown is the optical depth as integrated parallel to the z-axis starting at $z = \infty$. The value of the blue lines are to be read from the right y-axis of the plot, giving the optical depth at the midplane. The value of the red lines are to be taken from the left y-axis, indicating the height above the midplane at which $\tau_\lambda = 1$. The solid/dashed lines refer to different locations of the pressure maximum.
Centre row: Relative abundance of grains with selected size a (colour coded) at the location of $\tau_\lambda = 1$ (see row above).
Bottom row: Relative abundance of grains with selected size a (same colours as above) at the midplane.

true for the 3 AU models, where the peak of $\alpha_{\mathrm{mm}}(r)$ is to be found at slightly smaller radii (≈ 2 AU to 3 AU)than r_{trap}. The feature that lacks in the $r_{\mathrm{trap}} = 30$ AU models is the clearing of the region inside the pressure maximum. As it can be seen, here large grains retain their impact on the spectral slope in the entire evolution of the disc in the simulation. Apparently, large grains are able to grow inside the pressure trap and finally are accreted by the star. One must bear in mind that the absolute flux of the disc in the millimetre images decreases by roughly a factor of ≈ 1.5, just as the dust mass of the disc does due to accretion. The possibility $r_{\mathrm{trap}} = 30$ AU was included in this study in order to investigate the dependence of the results on r_{trap}. Figure 6.5 clearly shows that not only the spectral slope which is due to the dust trapping mechanism changes, but also that the entire disc structure provides for a different spatial-spectral profile. However, a fully three dimensional treatment of the underlying MRI by Dzyurkevich *et al.* (2010) yields typical values for r_{trap} of 3 AU and 4.5 AU. This renders the applicability of the present choice of 30 AU as a realistic model moot.

6.4. Interferometric observation of pressure maxima

In the previous section, the observational consequences of dust grain trapping by local pressure maxima have been discussed. One important assumption in this respect was usage of ideal images. That is, the images obtained from radiative transfer (RT) calculations have not been convolved with instrument PSFs. As a result, the initial hypothesis that the spatially resolved spectral slope in the millimetre was shown to work, especially for the $r_{\mathrm{trap}} = 3$ AU case. In this section now the focus is shifted towards the posibility to recover of Figure 6.5 under realistic observing conditions, which complicates the issue.

6.4.1. Abilities and limitations of ALMA

The instrument of choice to measure one of the curves in Figure 6.5 is ALMA. Only this interferometer will offer the spatial resolution and the required millimetre wavelength regime. The set-up of the array would be a detour in the course of this section and is therefore subject of Chapter A in the appendix. Besides spatial resolution and observing wavelength, ALMA also offers the required sensitivity for the task (cf. also Figure 5.15). Observations with ALMA have been simulated with the help of the `CASA`[1] software package.

The employment of an interferometric instrument such as ALMA has three major drawbacks as compared to the ideal images from RT. The first is due to the convolution of the image with the PSF; the generally limited spatial resolution. The second one arises from the fact that instead of an image, samples of the (u, v)-plane

---

[1] `http://casa.nrao.edu/`

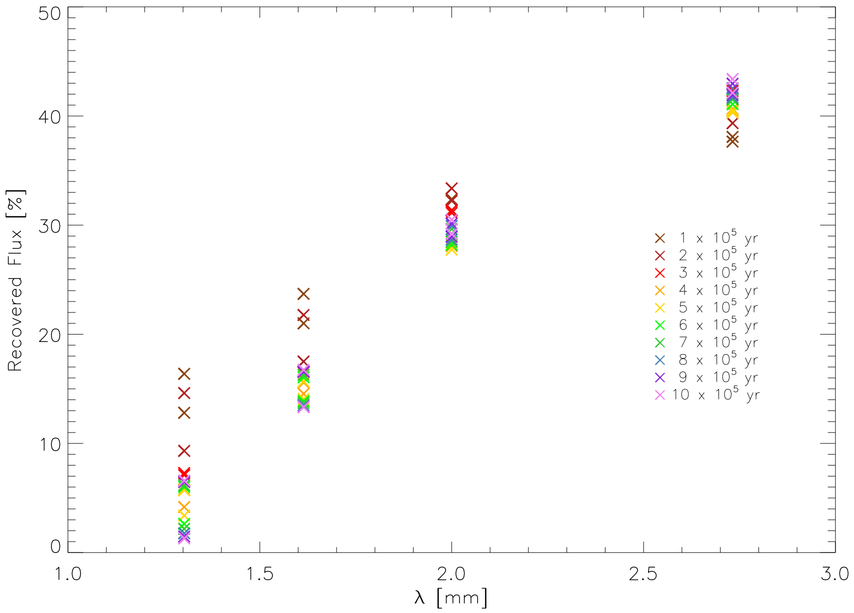

Figure 6.7.: Recovered flux in reconstructed images from ALMA observations at different wavelengths λ. Shown in different colours are images relating to disc at different times of their evolution.

are measured. Both these effects introduce considerably spatial uncertainty into the measurement; the first by smearing out the observed flux and the second one by the potential artifacts introduced in the image reconstruction algorithms.

The third drawback is that an interferometer does not measure absolute fluxes but only relative ones. The absolute flux of the model image is only recovered to a certain degree that depends on wavelength, array configuration, and the model. Figure 6.7 shows the recovered as function of the observing wavelength λ and the evolutionary stage of the model.

To determine the spectral slope α_{mm} an absolute flux calibration is needed, however. In the course of this Section, these absolute fluxes are known as a result of the radiative transfer calculations and hence can be used to calibrate the images reconstructed from the simulated ALMA observations. If the ALMA observations were to be conducted in reality, then supplementary single dish observations of the source in question are needed to provide these fluxes. The proper combination of interferometric and single dish data is nothing to be undertaken lightly because of the different apertures of both instruments (see also Section 4.2.2).

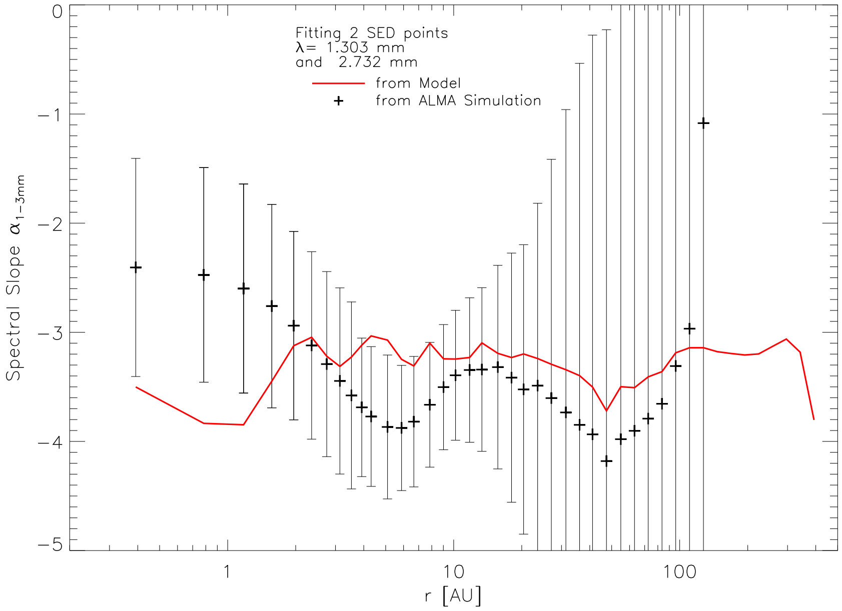

Figure 6.8.: Spectral slope as obtained from the RT model as well as from subsequent ALMA-simulation. The parameters of the model are $r_{\text{trap}} = 3\,\text{AU}$, $t = 7 \times 10^5\,\text{yr}$ and $v_{\text{frag}} = 5\ {}^{\text{m}}\!/_{\text{s}}$.

6.4.2. Results from observations with ALMA

As can be seen in Figure 6.5, the spectral slope is quite variable with radius and the sought-for features of α_{mm} are considerably small in both, spectral-slope-amplitude and radial position. In Figure 6.4, the radial profile as obtained from the ideal RT image (blue line) as well as obtained from the respective ALMA-observation (red line) with error bars is given. Further, the respective PSF is plotted. The FWHM of the PSF is naturally smaller at short wavelengths, however in the millimetre regime, it is always larger than 3 AU. Consequently, the effects of the different grain sizes in- and outside the pressure trap are smeared out to a high degree. At large radii, the error bars on the reconstructed ALMA image are considerably large. These errors are mainly due to the low absolute flux values in these regions. This uncertainty is also reflected in the ‘noisy’ behaviour of the PSF far away from its centre.

Figure 6.8 shows how the uncertainties that arise in the determination of the radial profile translate into uncertainties of the spectral slope. Ironically, at radii larger than $\approx 10\,\text{AU}$, the spectral slopes from the reconstructed ALMA images are not far off the ones in the ideal RT image. However, there the error bars are extremely large. At smaller radii, where the error bars are smaller and of acceptable size, the values for α_{mm} are farther off and even the shape of the curve is not the same anymore. This issue holds for all models. For some it is a little more pronounced, for some less.

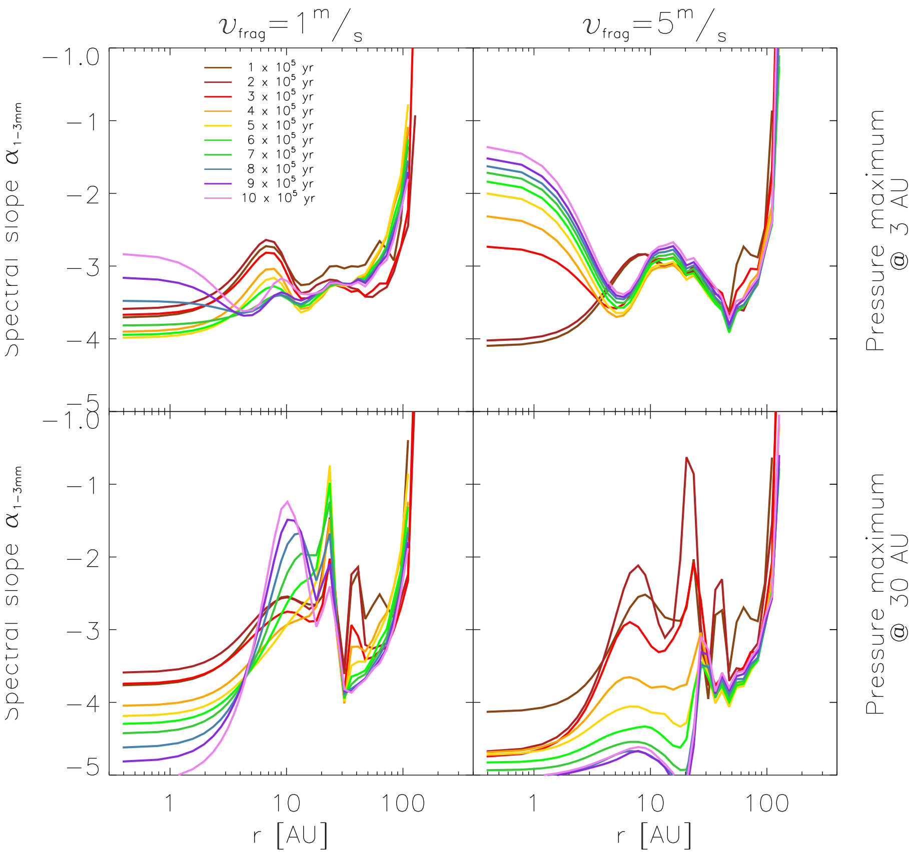

Figure 6.9.: Spectral slopes for different models at different times of their evolution (colour coded) as obtained from ALMA observations. The slopes result from 1.3mm and 2.7mm reconstructed images. See also Figure 6.5.

Signature of pressure maxima at 3 AU

Figure 6.9 gives the spectral slopes α_{mm} of all models as obtained from reconstructed ALMA observations. In this Figure, the consequence of the large errors at radii $r > 100\,\mathrm{AU}$ can be seen in the upward bent of all curves at large radii. It might come to some surprise that, despite the large PSFs used in the process, the signature of the pressure maxima seems not to be lost in general. The models with the pressure maximum at 3 AU feature a distinctive peak in the spectral slope. However, this peak is located at $r \approx 10\,\mathrm{AU}$ which is a little more than the respective PSF width at $\lambda = 2.7\,\mathrm{mm}$. Thus, although the possibility to locate the trapped dust grains exactly is lost, their influence is still seen in the ALMA observations. The clearing of disc regions $r < r_{\mathrm{trap}}$ that is seen as a function of time in Figure 6.5 cannot be inferred from the reconstructed ALMA images, however. The ability to resolve disc structures considerably smaller than the respective PSF is of course beyond any instrument's capability.

Signature of pressure maxima at 30 AU

The results for disc models with $r_{\text{trap}} = 30\,\text{AU}$ are even more difficult to interpret. In the lower row of Figure 6.9, a small variation in α_{mm} can be seen at r_{trap} that is more pronounced for younger models. Given the errors involved, this hardly can be seen as a tracer for dust trapping mechanism. The peak in $\alpha_{\text{mm}}(r)$ that is seen between 10 AU and 20 AU in the slopes derived from RT images is much more pronounced for $v_{\text{frag}} = 1\ {}^{\text{m}}\!/_{\text{s}}$, reaching values as extreme as $\alpha_{\text{mm}} \approx -1$. For $v_{\text{frag}} = 5\ {}^{\text{m}}\!/_{\text{s}}$ the 'peak' even becomes a minimum of α_{mm}. These slopes cannot be understood by the ideas that form the basis of the spectral index α_{mm} in Section 2.3.2 alone but only by taking into account the redistribution of fluxes by the PSF in the image and the uncertainties in the image reconstruction.

6.4.3. Results & Discussion

It has been demonstrated in this Chapter that dust trapping due to local pressure maxima in the disc yields tracers in spatially resolved millimetre SEDs. Models with $r_{\text{trap}} = 3\,\text{AU}$ and $v_{\text{frag}} = 1\ {}^{\text{m}}\!/_{\text{s}}$ leave a clear trace in the radially resolved spectral slope α_{mm} in ideal images for all stages of evolution considered. Using ALMA, this signature can be recovered, although these observations are at the edge of ALMAs spatial capabilities. This can be seen by the fact that for other values of r_{trap} and v_{frag}, the signature becomes less distinct.

One might be tempted to ask, if the the spectral slope can be determined without the need of image reconstruction directly in the (u, v)-plane of the actual interferometric data. However, it can be shown, that although this can be done for a very small class of models with high symmetry, in general such a procedure is equivalent to a discrete Fourier transform of the (u, v)-data and eventually deals with the same issue the image reconstruction does.The reason for this is that the spatial information required to constrain α_{mm} is not attributed to one (u, v) point or a small, finite set of them but rather is distributed among the entire (u, v) plane. The incomplete sampling of this plane gives rise to the same uncertainties that plague interferometric image reconstruction.

An important issue also is the uniqueness of the results. If the problem is posed the other way round, namely if a given observation allows to infer trapped dust grains by means of a local pressure maximum due to dead zones. The answer is of course no. For example, the dust grains could be trapped by gravitational instabilities leading to spiral structure (Cossins *et al.*, 2009) or by zonal flows (Johansen *et al.*, 2009). All these mechanisms result in a position depended composition of the dust population with respect to grain sizes. However, constraints on $\alpha_{\text{mm}}(r)$ do not necessarily constrain the actual mechanism that causes them. A investigation of effects on α_{mm} by dust dust grain growth and fragmentation without radial drift (thus assuming some generic dust trapping mechanism) is presented by Birnstiel *et al.* (2010b).

In the context of the current chapter, a non-detection in real observations of any radial dependence of α_{mm} would provide the strongest constraints for disc models. Although the radial structure of α_{mm} as discussed in this Chapter can hardly been seen as unique in general, it is also true that the dust trapping mechanism as presented does impose a radial structure on α_{mm}. The non-detection then in turn places constraints on the magnitude of the dust trapping that operates in the observed system, respectively.

7. Dust settling in IRAS 04302+2247

Τί δ’ εἰ καὶ ἠχὼ τὸ δεσμωτήριον ἐκ τοῦ καταντικρὺ ἔχοι;
ὁπότε τις τῶν παριόντων φθέγξαιτο, οἴει ἂν ἄλλο τι
αὐτοὺς ἡγεῖσθαι τὸ φθεγγόμενον ἢ τὴν παριοῦσαν σκιάν;
μὰ Δί’ οὐκ ἔγωγ’, ἔφη.

(Platon, Πολιτεία*)*

In this Chapter, new interferometric data on the ‘Butterfly Star’ is presented. The data allows a to extend the current model of the system. This extension allows the interpretation of the new data as the first evidence on radial dependent dust settling from millimetre observations of an edge-on seen disc.

7.1. The object

Nicknamed the “Butterfly Star”, IRAS 04302+2247 is a show-case like specimen of a class I T Tauri star (Lada & Wilking, 1984; Lucas & Roche, 1997). The circumstellar disc is located at a distance of 140pc in the Taurus-Auriga star-forming region and is seen in a edge-on orientation ($\theta = 90^\circ \pm 3^\circ$)(Padgett *et al.*, 1999). In the last decade, it was object of intense study. Valuable insight into its structure has been gained by ground-based near-infrared images and polarisation maps (Lucas & Roche, 1997), near-infrared images from the HST (Padgett *et al.*, 1999) as well as interferometric observations at 0.84mm (Wolf *et al.*, 2008b), 1.3mm, and 2.7mm (Wolf *et al.*, 2003). The Butterfly Star was the first for which a multi-wavelength model has been successfully constructed (Wolf *et al.*, 2003).

Although similar at first sight, the circumstellar disc in the Bok globule CB 26 (see Chapter 3) features two important differences. First, in order to correctly reproduce the spectral slope in the millimetre regime, a maximum dust grain size of $a_{\max} = 100\,\mu$m is required for IRAS 04302+2247 while this limit is $a_{\max} = 2.5\,\mu$m in the case of CB 26. And secondly, CB 26 shows an considerable inner dust free region of $r_{\rm in} = 45\,$AU, while this not the case for IRAS 043202+2247 (Wolf *et al.*, 2008b).

The subject of this Chapter are new observations of the disc in the Butterfly Star at 1.3mm and their possible interpretation. Although the model published by Wolf

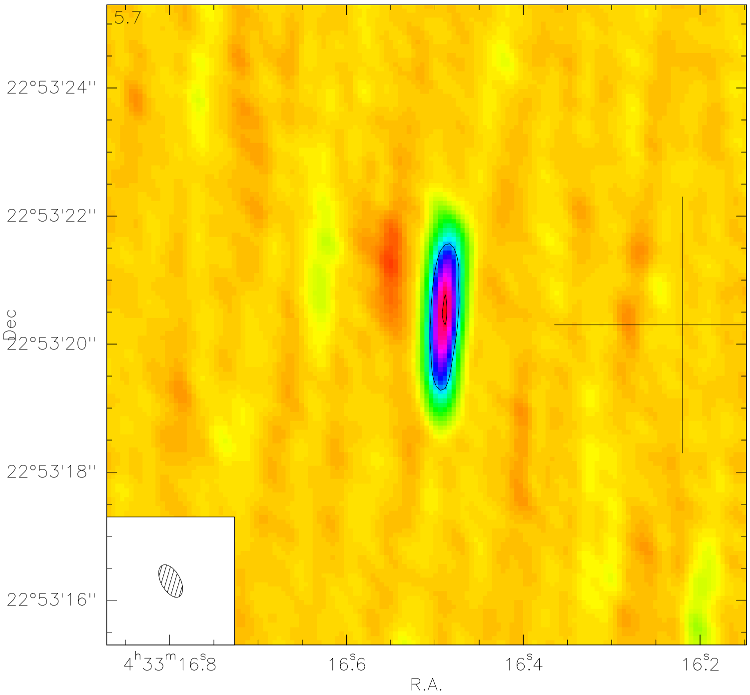

Figure 7.1.: Reconstructed image of the disc IRAS 04302+2237 at 220 GHz (1.3 mm). The size of the clean beam *(lower left corner)* is 0.56″ × 0.3″, PA 29°. The cross marks the phase reference centre.

et al. (2003) needs adjustment to account for the new data, an inner void is not supported by the data. Instead, the observations might be the first image of a young edge-on disc that undergoes radial dependent settling.

7.2. Observation

IRAS 04302+2247 was observed on February 3rd, 2010, at the Plateau de Bure Interferometer at 1.3 mm (220 GHz) using the largest available configuration with a baseline of about 760 m corresponding to 590 kλ. The object was observed for 7.5 h which yields a total on-source time of $\sim$ 5 h. Using all six antennas, a resolution of 0.56″ × 0.3″ with a PA of 29° was achieved. This corresponds to $\approx$ 7 resolution elements along the disc midplane. The data were reduced using the `GILDAS`[1] software package supplied by IRAM Pety (2005). Standard calibration settings were used in the pipeline processing for all data. The total flux of the source is $\approx$ 100 mJy. In Figure 7.1, the reconstructed image is shown.

The image is clearly centrally peaked and does not show any plateau or double-peak structure (see also Fig. 7.2). The latter two are seen in HH 30 and CB 26 and

---

[1] `http://www.iram.fr/IRAMFR/GILDAS/`

in both cases interpreted as the tracer of an inner void.

7.3. Analysis and Discussion

7.3.1. The primary model

In order to understand this new observation, the model given by Wolf *et al.* (2003) needs to be extended. The disc dust density distribution is given by Equations (2.2) and (2.3). The values of the model parameters are summarised in Table 7.1. The dust disc has a radius of 300 AU and extends inward to the dust sublimation radius at 0.07 AU where a dust temperature of 1500 K is reached. The model further consists of an envelope as published by Ulrich (1976) similar to the one seen in CB 26 (Chapter 3). This envelope that is responsible for the appearance of the system in the near-infrared. However, for $\lambda > 174\,\mu$m the disc starts to dominate the flux distribution and at $\lambda = 1.3$ mm the envelope contributes less then $\sim 3\%$ of the total flux. For the purpose of the present analysis, the envelope structure can safely be neglected. The same dust model used throughout this thesis (see Section 2.2) is also employed here as well as the 'average' T Tauri star (Gullbring *et al.*, 1998).

7.3.2. Comparison to observation

As it can be seen in Figure 7.2, the model described in the previous section is not able to account for the observed brightness distribution along the midplane. Especially around $r \approx 150$ AU the predicted flux of the model is much to low. Several extensions to the model to account for the missing flux in model have been explored.

The first possibility is to consider an inner void. Such a void should be large enough to shift the emission peak farther away from the star on the one hand side and on the other hand side small enough such that when the image is convolved with the beam of the observation a centrally peaked brightness distribution is preserved. In the paper of Wolf *et al.* (2008b), the possibility of an inner void has already been discussed. The image of the disc at 840 μm is double-peaked which can be caused by two different effects. First, it could be an effect of optical depth: At this wavelength the inner disc regions are obscured by the high densities there and thus do not contribute to the brightness distribution. Secondly it could be the footprint of an inner void: Coming from millimetre to sub-millimetre wavelengths, the spatial resolution increases and might allow to resolve the inner gap. However, it was shown by the authors that optical depths effects are sufficient to explain the observed brightness distribution at 840 μm while an inner void is not a sufficient explanation.

The present analysis supports the first possibility. Figure 7.2 gives the brightness profile at 1.3mm for a disc with an inner radius of $r_{\mathrm{in}} = 50$ AU. Although such a model fits the slope and magnitude of the profile well at large radii, a very pronounced

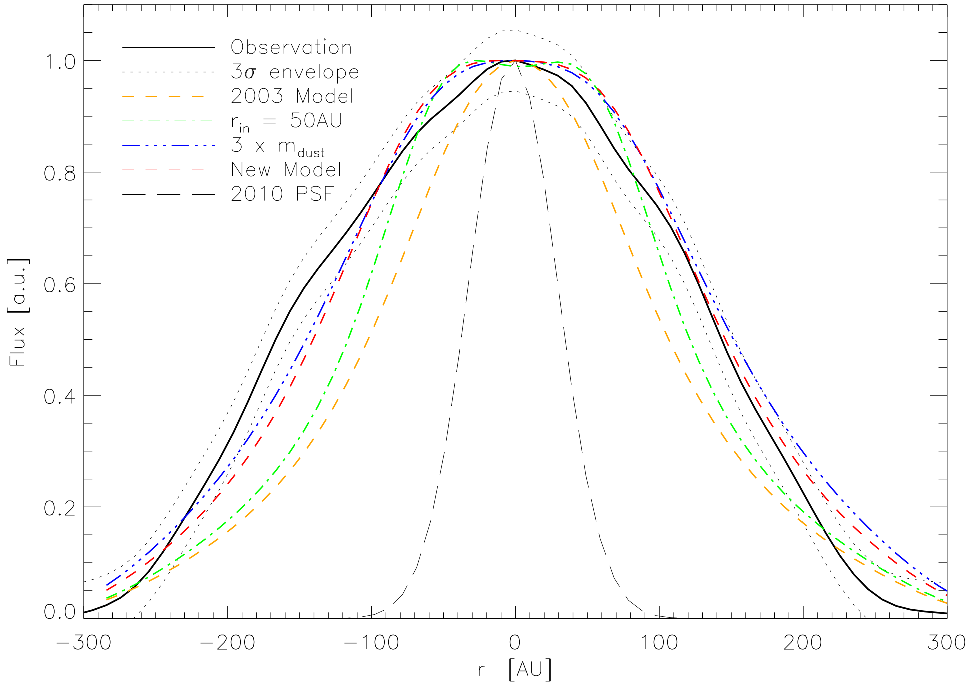

Figure 7.2.: Cut through the brightness distribution along the disc midplane of the observation and various models.

plateau structure should be observed in the central region, which is not the case.

A second possible extension of the initial model is to increase the disk dust mass. Following the reasoning of the previous paragraph, this results in an increased optical depth in the disc centre and consequently increases the contribution of outer disc parts to the image. Again, this obscuration cannot be so strong that it causes a double-peak structure. As Figure 7.2 shows this modification would indeed be able to reproduce a brightness distribution quite similar to observed one if the dust mass is increased by a factor of 3.1. However, such a model would also yield a total flux of 300 mJy, which is also wrong by almost the same factor.

7.3.3. Extension of the model

This Chapter argues for a third possibility to explain the appearance of the Butterfly Star at 1.3 mm: The extension of the local scale-height as given by Equation (2.3). This relation roots in the theory of viscous accretion (see Section 2.1) and describes the scale height of the gas disc in hydrostatic equilibrium. Very small dust grains can be described within the Epstein regime Cuzzi *et al.* (1993) and couple well to the gas such that their distribution is essentially identical to the gas distribution.

Parameter	Value
α	2.37
β	1.29
h_0	15 AU
m_{dust}	$7 \times 10^{-4}\,\mathrm{M}_\odot$
r_{in}	0.07 AU
r_{out}	300 AU
r_1	20 AU
β_1	2.0
h_1	0.42 AU
r_2	200 AU
β_2	1.1
h_2	6.4 AU

Table 7.1.: Overview of new model parameters. The ensemble on top refers to the original model, the bottom set to the extended model of this paper.

Large dust grains however increasingly decouple from the gas and sink to the disc midplane. Dullemond & Dominik (2004) have shown that the timescale t_{sett} for a dust grain – once grown via coagulation – to settle to its equilibrium height (given by the grain's diameter) is above all rather quick. The timescale is further radius dependent and spans ~ 5 orders of magnitude. In the setup discussed in the paper t_{sett} grows from ~ 1yr at $r = 0.1$ AU to 10^3yrs at $r = 300$ AU for $100\,\mu$m sized grains and 10^6yrs for 10 nm sized grains.

Given the presence of grains in all these size regimes in the Butterfly Star, the radial dependent scale height for the dust is parametrised as follows: The disc is divided into three domains at the radii $r_{1,2}$ with $r_{\mathrm{in}} \leq r_1 < r_2 \leq r_{\mathrm{out}}$. In the innermost region t_{sett} is very small hence all dust grains have settled close to the midplane. Consequently, the scale height is very small. In the outermost region, where t_{sett} is in the order of 10^5yrs, not all grains have yet settled and the scale height is similar to the gas scale height. The third is the transition region between the two cases above. In the outer domain, the scale height h_0 and the flaring parameter β (cf. Equation. 2.3) are left unaltered from the initial model because any significant change here would also be visible in the near-infrared images of the Butterfly Star (cf. Watson *et al.* (2007)). The values of h_0 and β are well constrained from the observations in Wolf *et al.* (2003). In the other two regions smaller values for h_0, namely h_1 and h_2, are chosen. To provide for a smooth transition of the values β_1 and β_2 are adjusted accordingly. For technical reasons, r_1, r_2, β_1, and β_2 are free parameters and h_1 and h_2 follow uniquely. In the second domain Equation (2.3) then reads

$$h(r_{\mathrm{cyl}}) = h_0 \left(\frac{r_2}{100\,\mathrm{AU}}\right)^{\beta-\beta_2} \left(\frac{r_{\mathrm{cyl}}}{100\,\mathrm{AU}}\right)^{\beta_2} . \tag{7.1}$$

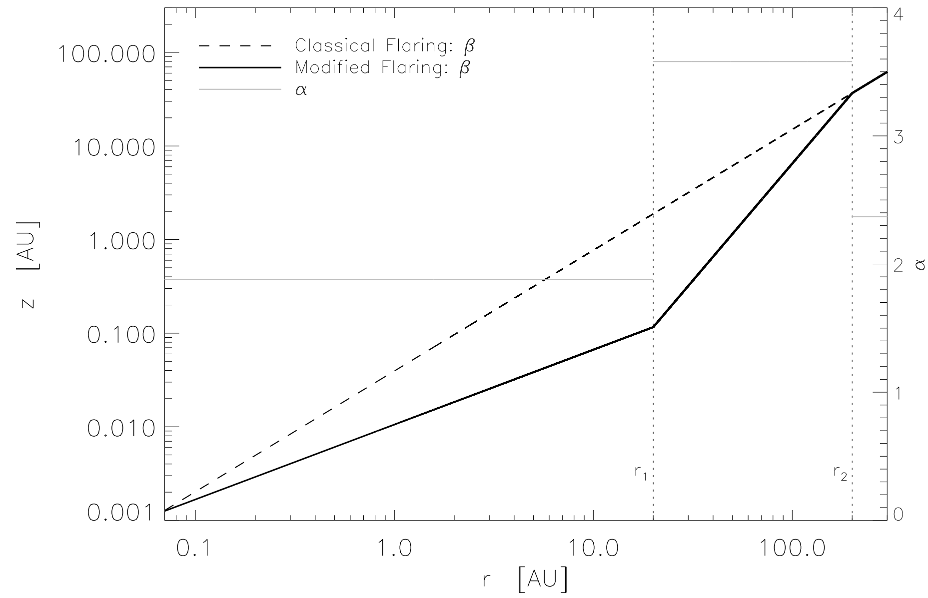

Figure 7.3.: The dust scale height of the model extension in all three disc domains. The dashed line refers to the original model by Wolf *et al.* (2003). Given is also the value chosen for α in order to preserve the power-law exponent of the surface density, cf. Equation (2.6).

In Figure 7.3, the overall $h(r_{\text{cyl}})$ that replaces Equation. (2.3) is shown. The surface density of the dust disc is given by integration in the z-direction an can be written as a power law as in Equation (2.6). The model extension shall not alter the power-law exponent $p_\Sigma = -1.08$ of the original model. To do so, α is chosen in each domain such that the changes introduced by β are counterbalanced. Figure 7.3 also gives the value for α in each domain.

7.4. Result

The result of the model extension can be seen as the red dashed line in Figure 7.2. It fits both, the width and the slope of the observed brightness distribution within 3σ of the observation. A very plausible way to interpret the new millimetre observation of the Butterfly Star is radial dependent sedimentation of large grains. The dust in the inner region is still present as an inner void would cause a different slope of the observed brightness distribution. But in relative terms, the dust can also not be present as high above the midplane as at large radii, as supposed by the old model, because then brightness distribution is too thin. The logical conclusion is that the large dust grains have settled towards at small radii but are still high afloat at large radii.

Compared with the earlier discussion about an inner void in IRAS 04302+2247 by Wolf *et al.* (2008b) this new observation is particularly useful as at 1.3 mm the thermal re-emission of the dust grains is now optically thin. This means that if there were an inner void comparable in size with the voids in HH 30 and CB 26 one should clearly see a similar double peak structure. In turn, this very much increases the certainty of our assessment of the absence of an inner void. Of course, as the settling time scale is a function of disc radius, the new observation now provide new constraints for dust evolution models of circumstellar disc. However, a detailed analysis with a multi-wavelength model of the object is subject of a future paper (Gräfe et al., in prep).

8. Concluding remarks

Παντάπασι δή, ἦν δ’ ἐγώ, οἱ τοιοῦτοι οὐκ ἂν ἄλλο τι
νομίζοιεν τὸ ἀληθὲς ἢ τὰς τῶν σκευαστῶν σκιάς.
πολλὴ ἀνάγκη, ἔφη.

(Platon, Πολιτεία*)*

8.1. Summary

In the present thesis, radiative transfer computations have been used to interpret new data observing dust grain growth and sedimentation in circumstellar discs and to identify and provide interpretations and predictions of their observable quantities. New light is shed on the ability to identify dust grain growth and settling via imaging and the possibility to identify a dust trapping mechanism using the new interferometer ALMA (Chapters 5 & 6). By fitting parametric models to new observations, unexpected features of celestial objects have been revealed, such as inner voids, possible discs around high-mass protostars, and radial dependent settling (Chapters 3, 4, & 7). In detail, the findings of this thesis are as follows:

In Chapter 3, a high quality data set for the circumstellar disc in the Bok globule CB 26 has been compiled for a large span of wavelengths. Images in the NIR and in the millimetre regime have been obtained as well as photometric data and spectra. Together with literature values, a detailed model has been constructed. This model allows the interpretation of the data set with one single set of parameters. Based on the chosen dust composition and the resulting opacity structure of the best-fit disc model, the millimetre SED indicates that the grains feature the same grain size distribution and almost the same upper limit to the grain size as the interstellar medium (Section 3.5.1). In order to account for the brightness distribution in the 1.3 mm image, an inner hole with a radius of 45 AU has been asserted (Section 3.5.2). The disc is massive with a total dust and gas mass of $0.3\,\mathrm{M}_{\odot}$ under the assumption of spherical grains and $\rho_{\mathrm{grain}} = 2.5\,\mathrm{g\,cm}^{-3}$, compared to a mass of the central T Tauri star of $0.5\,\mathrm{M}_{\odot}$, and therefore is possibly, but not inevitably, unstable (Section 3.5.3). The model very nicely reproduces the prominent chromaticity of the dark lane as seen in the near infrared images (Section 3.5.4).

In Chapter 4, the possibility to describe high mass protostellar object IRAS 18151-1208 with a scaled up version of the T Tauri model setup as used in Chapter 3 was investigated. It is possible to interpret the elongated structure in the millimetre image as disc of similar shape as the disc in CB 26 or the “Butterfly-Star”. Parameters such as mass, extent and central star scale accordingly by a factor of ~ 10 to ~ 15.

In Chapter 5 the effects of dust grain growth and sedimentation on images of circumstellar discs at various wavelengths and inclinations have been investigated. Employing a parametrised model, a discussion of the general effects of the depletion of upper disc layers by grain growth and dust sedimentation is achieved. This discussion is particularly interesting in the advent of telescopes providing high spatial resolution. Although the approach is based on certain simplifications, tracers have been identified that uniquely allow one to constrain the evolutionary stage of a disc. In particular, the findings have direct implications on future observations: The width of the dark lane in NIR images of edge-on discs is degenerate with respect to the degree of depletion of upper disc layers from large grains and observing wavelength. Although this wavelength and the degree of depletion do not exactly mirror each other’s impact on the width of the dark lane, a given lane width can be reproduced by adjusting both parameters (Section 5.2.1). High spatial resolution also needs to be accompanied by high sensitivity in the case of millimetre images. Only ALMA will provide the required resolution and sensitivity to identify grain sedimentation in millimetre images of discs seen edge-on. Settled discs show a relative surface brightness decrease of $\sim 10^{-4}$ from the midplane to 150 AU above the disc while non-settled discs show a decrease of only $\sim 10^{-2}$ (Section 5.2.2). A comparison of the FWHM of the brightness distribution in N and Q band images allows one to constrain the degree of dust sedimentation in a circumstellar disc if seen edge-on. Evolved discs in our parameter space show a ratio of the Q band FWHM to the N band FWHM of ~ 0.8 which depends only very weakly on other disc properties. Young discs however show a ratio that depends strongly on other disc parameters and scatters for various combinations of parameter values around the average FWHM ratio of ~ 1.0 (Section 5.2.3). The relative sedimentation height $\tilde{h}$ to which particles settle can be determined using face-on observations in the N and Q band. Due to the complex interaction between the spatial structure of the optical depth and the temperature distribution, discs with settling of large grains close to the midplane exhibit a gap in the observed radial brightness distribution at typically $\sim 100\,\mathrm{AU}$. However, the effect is only seen in discs considerably larger than $\sim 100\,\mathrm{AU}$ (Section 5.2.4). Ambiguities are discussed that prevent from being achieved the same results for images in other wavelength regimes (Section 5.3).

In Chapter 6, the focus is on the specific tracers of dust grains trapped by virtue of a local radial pressure maximum. In Section 6.3 the spatially resolved spectral slope α_{mm} is identified as a suitable footprint. The dependency α_{mm} as function a of r on the location of the pressure maximum r_{trap}, the critical fragmentation velocity v_{frag}

and the evolution on timescales of 10^5 yr is discussed. In Section 6.4 the observability of $\alpha_{\mathrm{mm}}(r)$ with ALMA is investigated. Problems arising from the size of the PSF, image reconstruction, and flux calibration are examined. Although the limitations are severe, the more realistic models with $r_{\mathrm{trap}} = 3\,\mathrm{AU}$ are shown to retain remnants of the original tracer.

In Chapter 7, new data for IRAS 04302+2247 are presented. In order to account for these, an extension to the existing model is suggested that describes radial dependent settling of dust grains.

8.2. Outlook

The results of this thesis inspire further investigations. For example, future observations with high spatial resolution, especially in the sub-millimetre regime, are required to confirm the interpretation of a low optical depth along the line of site at 1.3 mm in the model for CB 26. These observations should also yield better constraints on the vertical structure of the disc in CB 26 than was possible in this work with the envelope/disc distinction. The example of the 'Butterfly Star' points here in a very promising direction. Of course, with the new data for IRAS 04302+2247, a new, complete model is needed that not only explains the 1.3mm image but also is consistent with other data available for the object.

Although the results on the high-mass disc candidate IRAS 18151 should not be over interpreted, an interesting line of thought is given for massive star formation that should be pursued further in order to establish a similar disc paradigm as it exists for low mass T Tauri stars. The general markers of dust grain growth and sedimentation as presented in Chapter 5 also form a solid basis for further research. As a next step, a disc parametrisation should be chosen that incorporates radially dependent sedimentation. This would also serve as a complement to the heuristic model of Chapter 7. Naturally, modelling of images of an individual object will provide a better insight in its particular evolutionary stage. Nevertheless, the knowledge gained in the current framework forms a non-comprehensive basis for further analysis of dust grain growth and sedimentation effects on images. The results show that high resolution imaging is capable of confidently distinguishing between different scenarios. The results of Chapter 6 are far from discouraging. On the contrary, they show that the delicate difficulties that arise in the detection and interpretation of spatially resolved spectral slopes show that this is not the end of the journey.

However, all these questions are beyond the scope of this thesis. With the advent of ALMA and the ELTs on the horizon, new exciting observations are about to come and it would be very surprising if nothing unexpected would be found in these data. Despite all efforts in predicting the observational consequences of current models concerning the onset of planet formation via dust grain growth, nature has frequently (almost reliably) proven to puzzle not only scientists with unexpected observations.

A. Configuration of the ALMA-Observatory

The Atacama Large Millimeter Array is currently constructed in the Chilean desert. It is a joint effort of the ESO, the NRAO and the NAOJ. The array consists of 50 antennae, each with 12m in diameter. Despite its name, the shortest wavelength accessible with this interferometer will be $330\,\mu$m. The longest wavelength will be 2.7mm, with possible extensions in the future. The first science runs are scheduled for autumn 2011. Possible configurations of the array include compact setups with baselines of ≈ 125m and extended setups with baselines as long as ≈ 16km. Possible spatial resolutions range from $0.005''$ to $5''$, depending on observation wavelength and setup. Amongst other science targets, ALMA is ideally suited to investigate the nature of circumstellar discs.

In this Chapter, the setup chosen in order to reconstruct $\alpha_{\rm mm}$ in Section 6.4 is presented. On the on hand, the setup has to provide the spatial resolution to probe the size of the region of the trapped dust particles. As the observation shall be carried out at 1.3mm and 2.7mm to determine $\alpha_{\rm mm}$, the spatial resolution calls for a very extended array configuration. Figure A.1 (*left*) gives the spatial resolution of ALMA for a disc located at 140pc for different observing wavelengths and array configurations. On the other hand, the sensitivity has to be high enough to observe the radial profile of the disc. The sensitivity of the array is highest in its most compact configuration for an object that is directly overhead. More extended configurations are less sensitive as by relocating the array's antennae further away each other less detection area in relation to the configuration's diameter is available. Also, the relative detection area decreases for objects not in the zenith as only the individual antennae can be tilted accordingly but not the plane of the whole array. Figure A.1 (*right*) depicts this issue. In Figure A.2, the locations of the array antennae are in configurations #25, #26, and #27 are given.

To simulate ALMA observations various tools are at hand. One ALMA simulator is provided by IRAM as part of the data analysis software GILDAS. It can be obtained

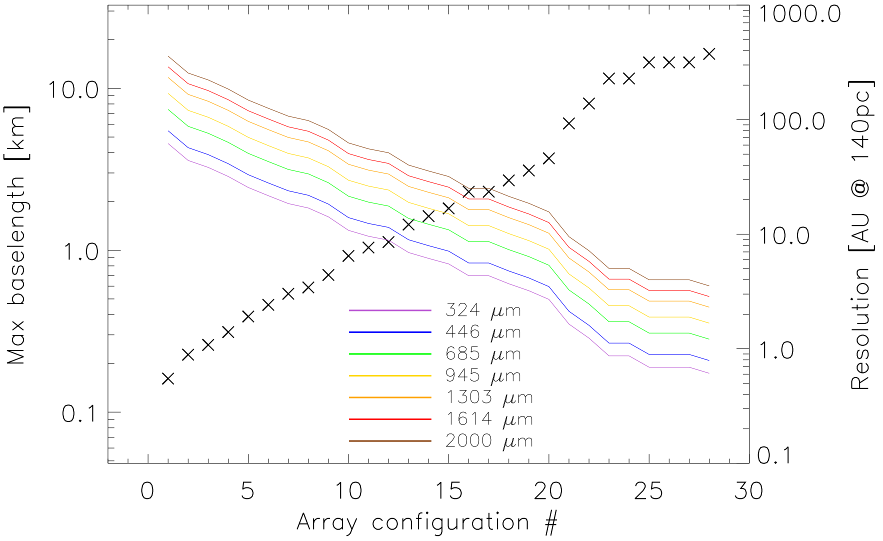

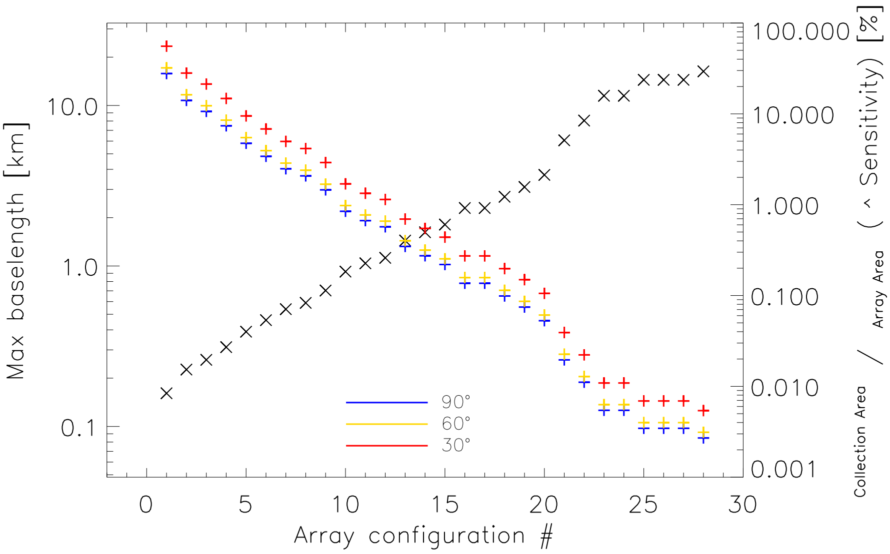

Figure A.1.: *Top:* Maximum resolution and baseline of various ALMA array configurations. The crosses correspond to the left axis indicating the baseline, while the coloured lines correspond to the right axis.
Bottom: Maximum baseline of various ALMA array configurations and their respective sensitivity.

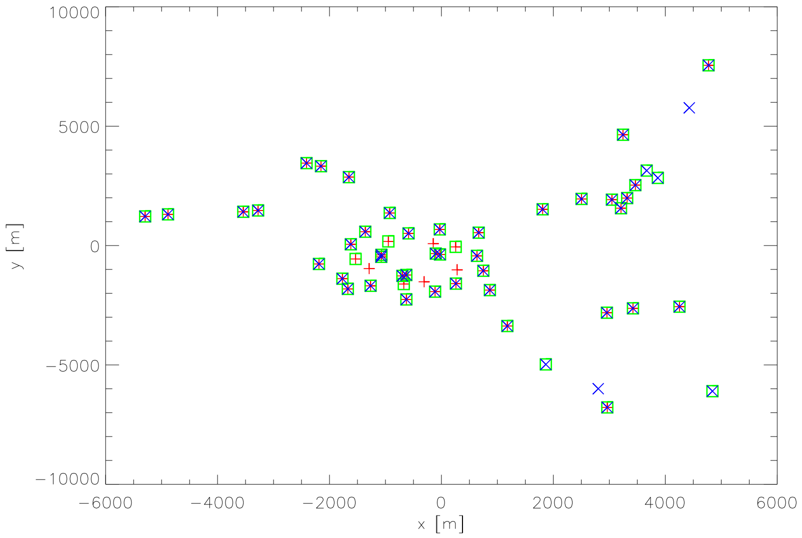

Figure A.2.: Location of the ALMA antennae in configurations #25 (blue), #26 (green), and #27 (red). The maximum baseline is always the same (see Figure also A.1).

from the IRAM website[1]. Another software package is brought forth by the NRAO. This ALMA simulator is part of the CASA software package which can be found at the NRAO website[2].

The work flow for both simulators is essentially the same. An object is provided to the software as an image, which is computed in this thesis by the RT code `MC3D`. The simulators allow to specify observing time, array set-up, location of the object on the sky, the noise level, and the image reconstruction algorithm. As a result, the (u, v) coverage is given, the visibilities as well as the reconstructed images, an estimate of the errors and the PSF. In this work, both software packages have been tested, and eventually the CASA ALMA simulator was used to get the results of Section 6.4.

As no specific science target is to be observed, the choice of location of the object is not constrained an can be chosen freely. Thermal noise of the atmosphere and the instruments is included in all simulations, assuming a ground temperature of 269K For the image reconstruction the Hogbom algorithm with natural weighting is chosen. The pixel size of all RT model images is $0.0028''$. A detailed description how to use the CASA ALMA simulator can be found in the *CASA-Cookbook*[3].

In order to balance all factors, namely resolution/configuration, observing time, and sensitivity, the standard deviation that is to be expected from each combination

---

[1] `http://www.iram.fr/IRAMFR/GILDAS/`

[2] `http://casa.nrao.edu/casa_obtaining.shtml`

[3] `http://casa.nrao.edu/Doc/Cookbook/book/casa_cookbook.pdf`

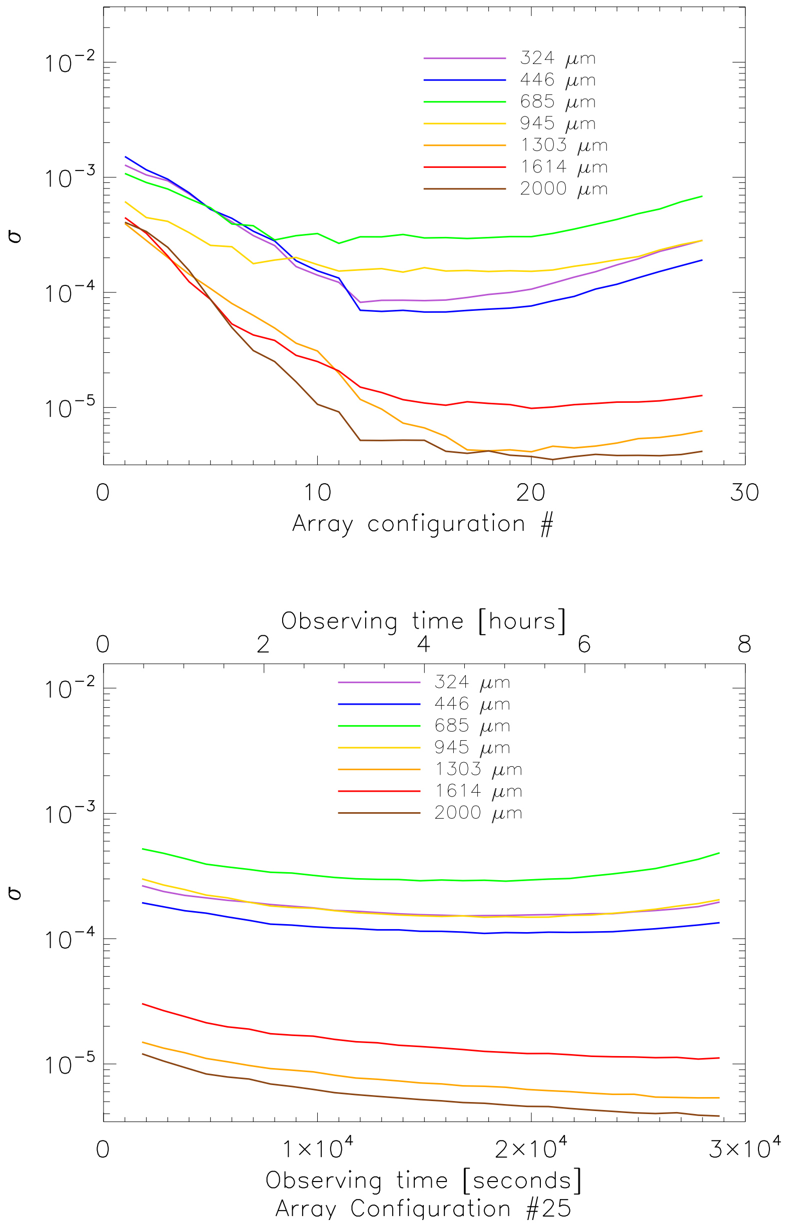

Figure A.3.: Quality of of ALMA observations given as value for standard deviation σ as function of array configuration (*top*) and observing time (*bottom*) for different wavelengths.

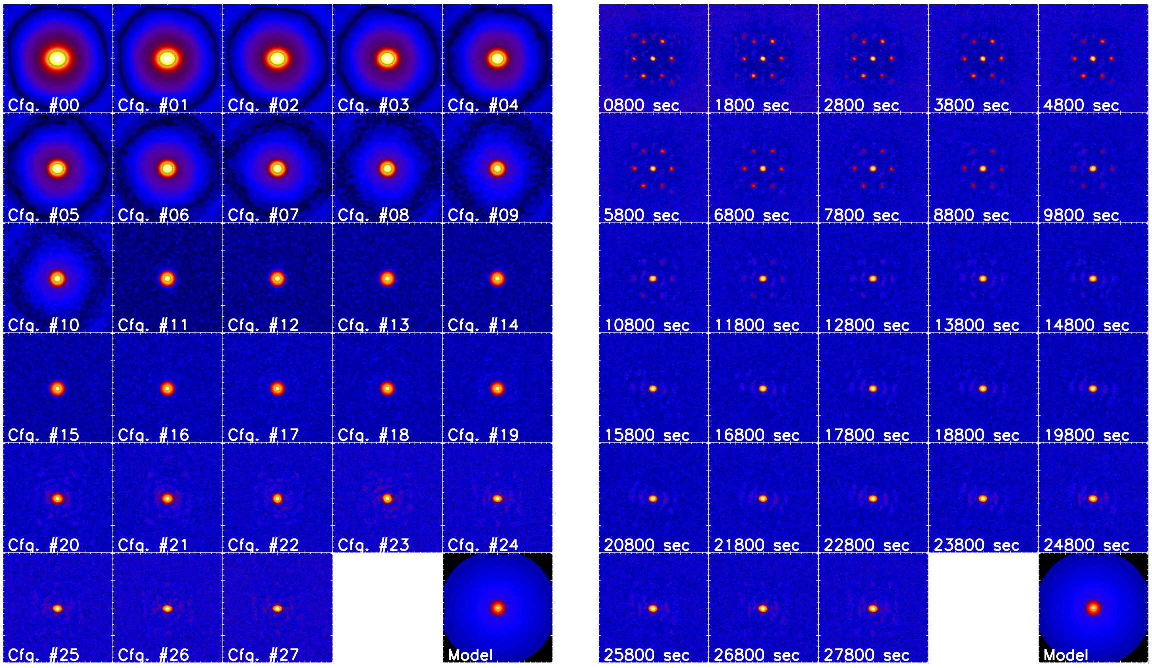

Figure A.4.: Reconstructed ALMA images of a model as described in Chapter 6 with $r_{\mathrm{trap}} = 3\,\mathrm{AU}$ and $v_{\mathrm{frag}} = 1\ ^{\mathrm{m}}/_{\mathrm{s}}$ at $t = 10^5\,\mathrm{yr}$ for different configurations (*left*) and observing times (*right*) at $\lambda = 330\,\mu\mathrm{m}$.

have been estimated. This estimate is accomplished by subtracting the reconstructed image from the initial RT model image and attributing deviation from zero in the outer part of the the resulting residual to random noise. Assuming this noise features a Gaussian distribution, σ can readily be computed.

Figure A.3 shows the standard deviation σ obtained in this way for all possible array configurations (*left*) and observing times (*right*). The observing times range from short 'exposures' of half an hour to an entire night's run of almost eight hours. Obviously, the most severe limitations come from the array configuration. Configuration number #20 with a maximum baseline of 4km show the smallest errors. For configurations featuring larger baselines, σ increases, especially for short wavelengths. As for the observing time, σ decreases for longer observations in the millimetre wavelength regime and for small λ, σ exhibits a minimum around 4 hour runs. Representatively for a model as described in Chapter 6 with $r_{\mathrm{trap}} = 3\,\mathrm{AU}$ and $v_{\mathrm{frag}} = 1\ ^{\mathrm{m}}/_{\mathrm{s}}$ at $t = 10^5\,\mathrm{yr}$, in Figures A.4 and A.5 the reconstructed ALMA image from different configurations and observing times are shown.

The required observations to obtain α_{mm} are to be carried out at $\lambda = 1.3\,\mathrm{mm}$ and $\lambda = 2.7\,\mathrm{mm}$, respectively. From Figure A.3 (*right*) it is clear, that as a consequence the longest possible observing time shall be chosen, namely almost eight hours. The array configuration chosen is setup #25 with a baseline of 11km. Although setup #28

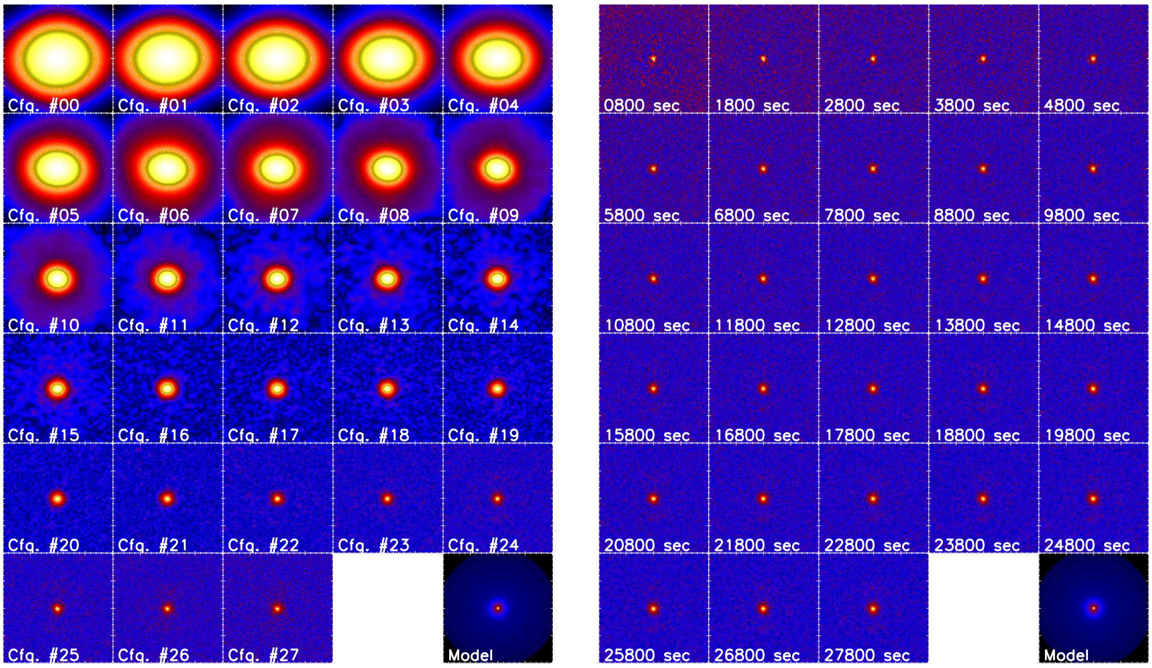

Figure A.5.: Reconstructed ALMA images of a model as described in Chapter 6 with $r_{\text{trap}} = 3\,\text{AU}$ and $v_{\text{frag}} = 1\ {}^{\text{m}}\!/_{\text{s}}$ at $t = 10^5\,\text{yr}$ for different configurations (*left*) and observing times (*right*) at $\lambda = 2\,\text{mm}$.

offers a large baseline, then gain in spatial resolution is more then counterbalanced by the loss in sensitivity and larger errors. Configurations #26 and #27 feature the same maximum baseline as #25. However, due to their different positioning of antennae at shorter baselines these configurations also feature a larger overall σ than #25.

B. Allegory of the cave

The headings of each Chapter are taken from the parable of the cave which is the opening of book seven in Plato's *Republic* written about 370 BC (Platon, 1991). The book is written in the style of a dialogue between the philosopher and Platon's teacher Socrates and some friends. The discussion features the definition and purpose of justice, the way a righteous city is to be run and the qualities of the decent man. Plato presents through the mouth of Socrates his theory of forms (or 'ideas') and his epistemology. The latter is given as an allegory, namely that of the cave. In the dialogue with his older brother Glaucon, Socrates starts:

Chapter 1 "Now consider," I said, "our nature in respect to knowledge and ignorance with the following situation. Think of people in a subterranean cave with an exit to daylight on its entire width. Understand them to be tied-up on legs and neck since their childhood such that they remain on their very spot, looking just in one direction and unable to turn their heads."

Chapter 2 Light is given to them by a fire burning behind them, far above in the distance. And in between the fire and the tied-up people there is a path along which you picture a low wall has been built, just as puppeteers have shields in front of them above which they play the marionettes."
"I picture that," he said.

Chapter 3 "Imagine now people carrying effigies of all sorts of things along the wall, sculptures of humans and animals, made of stone and wood in a plenitude of fashion. Naturally, some of these carriers speak and some do not."
"A strange image you speak of," he said, "and strange prisoners, too!"

Chapter 4 "They are like us," I said. First: Do you think that these people ever saw something else of themselves or of each other besides the shadows created by the fire on the other side of the cave?
"How could they," he said, "if they were forced to have their heads never moved in their life?"

Chapter 5 "And would not the same be true about the things carried past them?"
"Indeed!"

Chapter 6 "And if they could now speak to each other, don't you think they would assume that by naming the things they saw they would name the objects?"
"Necessarily!"

Chapter 7 "And if the cave had an echo from the opposite side and if any of the carriers spoke, do you think that they identified anything else as speaking than the shadow?"
"By Zeus, I do not", he said.

Chapter 8 "Under no circumstances," I continued, "could such people perceive anything else as reality as the shadows of the effigies."
"Quite predestined," he said.

The parable continues with the experience and the fate of a prisoner that is set free. First, he is shown the fire, the carriers, and the shadow casting effigies. Since his eyes are accommodated to the dark shadows, he has difficulties at first to identify anything in the brighter light. He then is even led outside the cave and realises that the sun is the ultimate source of everything, the ultimate 'idea'. Going back into the cave, the freed prisoner tells his cave-mates about his insights. Yet, he is not believed as his eyes again need time to accommodate to the cave's darkness rendering him confused.

List of Figures

List of Tables

List of Abbreviations

AAS	American Astrophysical Society
abs	Absorption
ACS	Advanced Camera for Surveys, HST
ALMA	Atacama Large Millimeter Array
ASJ	Astronomical Society of Japan
ASP	Astronomical Society of the Pacific
AU	Astronomical Unit
CAHA	Centro Astronmico Hispano-Alemán
CASA	Common Astronomy Software Applications
CB	Catalogue of Clemens & Barvainis (1988)
CSO	Caltech Submillimeter Observatory
CTTS	Classical T Tauri Star
BC	Before Christ
E-ELT	European Extremely Large Telescope
ESO	European Southern Observatory
ext	Extinction
FIR	Far Infrared
FWHM	Full Width at Half Maximum
GILDAS	Grenoble Image and Line Data Analysis
GMT	Giant Magellan Telescope
HD	The Henry Draper Catalogue
HERA	Heterodyne Receiver Array, IRAM
HH	Herbig Haro Object
HST	Hubble Space Telescope
IAU	International Astronomical Union
IRAC	Infrared Array Camera, SST
IRAM	Institut de Radioastronomie Millimétrique
IRAS	Infrared Astronomical Satellite
IRS	Infrared Spectrograph, SST
ISM	Interstellar medium
JCMT	James Clerk Maxwell Telescope
KI	Keck Interferometer
MATISSE	Multi Aperture Mid-Infrared Spectroscopic Experiment
MIPS	Multiband Imaging Photometer for Spitzer, SST

MRI	Magneto-Rotational Instability
MRO	Magdalena Ridge Observatory
NAOJ	National Astronomical Observatory of Japan
NIC	NICMOS Camera, HST
NICMOS	Near Infrared Camera and Multi-Object Spectrometer, HST
NIR	Near Infrared
NRAO	National Radio Astronomy Observatory
OVRO	Owen Valley Radio Observatory
PA	Position Angle
PSC	Point Source Catalogue compiled by IRAS
PSF	Point Spread Function
PdBI	Plateau de Bure Interferometer, IRAM
RAS	Royal Astronomical Society
RGB	Red-Green-Blue colour model
RT	Radiative Transfer
sct	Scattering
SCUBA	Submillimetre Common-User Bolometer Array, JCMT
SED	Spectral Energy Distribution
SHARC-II	Submillimeter High Angular Resolution Camera II, CSO
SINFONI	Spectrograph for Integral Field Observations in the Near Infrared
SMA	Sub-Millimeter Array
SPIE	Society for Optics and Photonics
SST	Spitzer Space Telescope
TMT	Thirty Meter Telescope
VLT	Very Large Telescope
VLTI	Very Large Telescope Interferometer
VISIR	VLT Imager and Spectrometer for mid Infrared
YSO	Young Stellar Object

List of Symbols

α	Density exponent
α_{mm}	Spectral slope at millimetre wavelengths
α_{ν}	Viscosity parameter
a	Dust grain radius
A_{V}	Visual extinction
β	Flaring exponent
β_{mm}	Spectral slope of the opacity at millimetre wavelengths
B_{ν}	Specific radiative black body intensity
c	Speed of light in vacuum ($3 \times 10^{8}\ {}^{\mathrm{m}}\!/_{\mathrm{s}}$)
c_{S}	Sound speed
$C_{(\mathrm{abs,ext,sct})}$	Cross section of absorption, extinction and scattering
d	Telescope diameter
D	Distance between object and observer
ϵ	Depletion parameter
$\epsilon_{\parallel}$, $\epsilon_{\perp}$	Dielectric constant with parallel and perpendicular orientation
F_{d}	Drag force on dust grains
γ	Envelope power-law exponent
G	Gravitational constant ($6.67 \times 10^{-11}\,\mathrm{m^{3}\,kg^{-1}\,s^{-2}}$)
h	Scale height
$\hbar$	Reduced Planck's constant ($1.05 \times 10^{-34}\,\mathrm{Js}$)
$\tilde{h}$	Scale height relation
h_{0}	Scale height at 100 AU
I_{ν}	Specific intensity
$\hat{I}_{\lambda}$	Visibility at specific wavelength
j_{ν}	Specific emissivity
κ_{ν}	Specific opacity
$\varkappa$	Keplerian angular frequency
k_{B}	Boltzmann's constant ($1.38 \times 10^{-23}\,\mathrm{J/K}$)
λ	Wavelength
L	Luminosity
$\mathrm{L}_{\odot}$	Solar luminosity ($3.84 \times 10^{26}\,\mathrm{W}$)
m	Mass
$\dot{M}$	Accretion rate
$\mathrm{M}_{\odot}$	Solar Mass ($2 \times 10^{30}\,\mathrm{kg}$)

ν	Frequency
$\tilde{\nu}$	Viscosity
n	Number of dust grains
Ω	Solid angle
ϕ	Scattering phase function
φ	Angular resolution
p	Gas pressure
p_{Σ}	Surface density exponent
Q	Toomre parameter
$Q_{(\mathrm{abs,ext,sct})}$	Efficiency factors for absorption, extinction and scattering
ρ	Mass density
$\tilde{\rho}$, ρ_0	Density scaling constants
r	Spherical radial coordinate
$\vec{r}$	Three-dimensional space point
r_{cf}	Centrifugal radius
r_{in}	Inner disc radius
r_{out}	Outer disc radius
r_{cyl}	Cylindrical radial coordinate
$\mathrm{R}_{\odot}$	Solar radius ($6.96 \times 10^{8}\,\mathrm{m}$)
R_{*}	Stellar radius
R_{100}	Normalising constant (100 AU)
σ	Standard deviation
Σ	Surface density
S_{ν}, S_{λ}	Specific electromagnetic flux
τ_{ν}, τ_{λ}	Optical depth
θ	Disc inclination
t	Time
t_{sett}	Settling timescale
T	Temperature
T_{eff}	Effective surface temperature
u	First coordinate in 2D Fourier space
$\vec{U}$	Point in the 2D Fourier space
v	Second coordinate in 2D Fourier space
v_{frag}	Critical fragmentation speed
v_{rel}	Relative velocity between gas and dust
x	First generic spatial coordinate
$\tilde{x}$	Size parameter for Mie theory
$\vec{X}$	Interferometric baseline
y	Second generic spatial coordinate
ζ	Gas-to-dust ratio
z	Height above the disc midplane

Bibliography

Adams, F. C., Lada, C. J., & Shu, F. H. 1987. Spectral evolution of young stellar objects. *ApJ*, **312**(Jan.), 788–806.

Alonso-Albi, T., Fuente, A., Bachiller, R., Neri, R., Planesas, P., & Testi, L. 2008. The Dusty Disk around VV Serpens. *ApJ*, **680**(June), 1289–1294.

Backman, D. E., & Paresce, F. 1993. Main-sequence stars with circumstellar solid material - The VEGA phenomenon. *Pages 1253–1304 of:* E. H. Levy & J. I. Lunine (ed), *Protostars and Planets III.*

Balbus, S. A., & Hawley, J. F. 1991. A powerful local shear instability in weakly magnetized disks. I - Linear analysis. II - Nonlinear evolution. *ApJ*, **376**(July), 214–233.

Beckwith, S., Staude, J., Quetz, A., & Natta, A. (eds). 1996. *Disks and Outflows Around Young Stars.* Lecture Notes in Physics, Berlin Springer Verlag, vol. 465.

Beckwith, S. V. W., & Sargent, A. I. 1991. Particle emissivity in circumstellar disks. *ApJ*, **381**(Nov.), 250–258.

Beckwith, S. V. W., Sargent, A. I., Chini, R. S., & Guesten, R. 1990. A survey for circumstellar disks around young stellar objects. *AJ*, **99**(Mar.), 924–945.

Beuther, H., Schilke, P., Sridharan, T. K., Menten, K. M., Walmsley, C. M., & Wyrowski, F. 2002. Massive molecular outflows. *A&A*, **383**(Mar.), 892–904.

Birnstiel, T., Dullemond, C. P., & Brauer, F. 2009. Dust retention in protoplanetary disks. *A&A*, **503**(Aug.), L5–L8.

Birnstiel, T., Dullemond, C. P., & Brauer, F. 2010a. Gas- and dust evolution in protoplanetary disks. *A&A*, **513**(Apr.), A79+.

Birnstiel, T., Ricci, L., Trotta, F., Dullemond, C. P., Natta, A., Testi, L., Dominik, C., Henning, T., Ormel, C. W., & Zsom, A. 2010b. Testing the theory of grain growth and fragmentation by millimeter observations of protoplanetary disks. *A&A*, **516**(June), L14+.

Bjorkman, J. E., & Wood, K. 2001. Radiative Equilibrium and Temperature Correction in Monte Carlo Radiation Transfer. *ApJ*, **554**(June), 615–623.

Blum, J., Schräpler, R., Davidsson, B. J. R., & Trigo-Rodríguez, J. M. 2006. The Physics of Protoplanetesimal Dust Agglomerates. I. Mechanical Properties and Relations to Primitive Bodies in the Solar System. *ApJ*, **652**(Dec.), 1768–1781.

Bohren, C. F., & Huffman, D. R. 1998. *Absorption and Scattering of Light by Small Particles.*

Boss, A. P., & Yorke, H. W. 1996. Protoplanetary Disks, Mid-Infrared Dips, and Disk Gaps. *ApJ*, **469**(Sept.), 366–+.

Brauer, F., Dullemond, C. P., Johansen, A., Henning, T., Klahr, H., & Natta, A. 2007. Survival of the mm-cm size grain population observed in protoplanetary disks. *A&A*, **469**(July), 1169–1182.

Brauer, F., Dullemond, C. P., & Henning, T. 2008a. Coagulation, fragmentation and radial motion of solid particles in protoplanetary disks. *A&A*, **480**(Mar.), 859–877.

Brauer, F., Henning, T., & Dullemond, C. P. 2008b. Planetesimal formation near the snow line in MRI-driven turbulent protoplanetary disks. *A&A*, **487**(Aug.), L1–L4.

Brown, J. M., Blake, G. A., Dullemond, C. P., Merín, B., Augereau, J. C., Boogert, A. C. A., Evans, II, N. J., Geers, V. C., Lahuis, F., Kessler-Silacci, J. E., Pontoppidan, K. M., & van Dishoeck, E. F. 2007. Cold Disks: Spitzer Spectroscopy of Disks around Young Stars with Large Gaps. *ApJ*, **664**(Aug.), L107–L110.

Brown, J. M., Blake, G. A., Qi, C., Dullemond, C. P., Wilner, D. J., & Williams, J. P. 2009. Evidence for Dust Clearing Through Resolved Submillimeter Imaging. *ApJ*, **704**(Oct.), 496–502.

Campbell, M. F., Sridharan, T. K., Beuther, H., Lacy, J. H., Hora, J. L., Zhu, Q., Kassis, M., Saito, M., De Buizer, J. M., Fung, S. H., & Johnson, L. C. 2008. Mid-Infrared Photometry and Spectra of Three High-Mass Protostellar Candidates at IRAS 18151-1208 and IRAS 20343+4129. *ApJ*, **673**(Feb.), 954–967.

Cardelli, J. A., Clayton, G. C., & Mathis, J. S. 1989. The relationship between infrared, optical, and ultraviolet extinction. *ApJ*, **345**(Oct.), 245–256.

Cashwell, E. d., & Everett, C. J. 1959. *A practical manual on the Monte Carlo Method for random walk problems.* Pergamon.

Cesaroni, R., Galli, D., Lodato, G., Walmsley, C. M., & Zhang, Q. 2007. Disks Around Young O-B (Proto)Stars: Observations and Theory. *Protostars and Planets V*, 197–212.

Chiang, E. I., & Goldreich, P. 1997. Spectral Energy Distributions of T Tauri Stars with Passive Circumstellar Disks. *ApJ*, **490**(Nov.), 368–+.

Clemens, D. P., & Barvainis, R. 1988. A catalog of small, optically selected molecular clouds - Optical, infrared, and millimeter properties. *ApJS*, **68**(Oct.), 257–286.

Cohen, M., & Witteborn, F. C. 1985. Spectrophotometry at 10 microns of T Tauri stars. *ApJ*, **294**(July), 345–356.

Cossins, P., Lodato, G., & Clarke, C. J. 2009. Characterizing the gravitational instability in cooling accretion discs. *MNRAS*, **393**(Mar.), 1157–1173.

Cuzzi, J. N., Dobrovolskis, A. R., & Champney, J. M. 1993. Particle-gas dynamics in the midplane of a protoplanetary nebula. *Icarus*, **106**(Nov.), 102–+.

D'Alessio, P., Calvet, N., Hartmann, L., Lizano, S., & Cantó, J. 1999a. Accretion Disks around Young Objects. II. Tests of Well-mixed Models with ISM Dust. *ApJ*, **527**(Dec.), 893–909.

D'Alessio, P., Cantó, J., Hartmann, L., Calvet, N., & Lizano, S. 1999b. On the Thermal Stability of Irradiation-dominated Pre-Main-Sequence Disks. *ApJ*, **511**(Feb.), 896–903.

D'Alessio, P., Calvet, N., Hartmann, L., Franco-Hernández, R., & Servín, H. 2006. Effects of Dust Growth and Settling in T Tauri Disks. *ApJ*, **638**(Feb.), 314–335.

Dominik, C., & Tielens, A. G. G. M. 1997. The Physics of Dust Coagulation and the Structure of Dust Aggregates in Space. *ApJ*, **480**(May), 647–+.

Draine, B. T. 2006. On the Submillimeter Opacity of Protoplanetary Disks. *ApJ*, **636**(Jan.), 1114–1120.

Draine, B. T., & Lee, H. M. 1984. Optical properties of interstellar graphite and silicate grains. *ApJ*, **285**(Oct.), 89–108.

Draine, B. T., & Lee, H. M. 1987. Optical Properties of Interstellar Graphite and Silicate Grains: Erratum. *ApJ*, **318**(July), 485–+.

Draine, B. T., & Malhotra, S. 1993. On graphite and the 2175 A extinction profile. *ApJ*, **414**(Sept.), 632–645.

Draine, B. T., & Tan, J. C. 2003. The Scattered X-Ray Halo around Nova Cygni 1992: Testing a Model for Interstellar Dust. *ApJ*, **594**(Sept.), 347–362.

Duchêne, G., McCabe, C., Ghez, A. M., & Macintosh, B. A. 2004. A Multiwavelength Scattered Light Analysis of the Dust Grain Population in the GG Tauri Circumbinary Ring. *ApJ*, **606**(May), 969–982.

Duchêne, G., McCabe, C., Pinte, C., Stapelfeldt, K. R., Ménard, F., Duvert, G., Ghez, A. M., Maness, H. L., Bouy, H., Barrado y Navascués, D., Morales-Calderón, M., Wolf, S., Padgett, D. L., Brooke, T. Y., & Noriega-Crespo, A. 2010. Panchromatic Observations and Modeling of the HV Tau C Edge-on Disk. *ApJ*, **712**(Mar.), 112–129.

Dullemond, C. P., & Dominik, C. 2004. The effect of dust settling on the appearance of protoplanetary disks. *A&A*, **421**(July), 1075–1086.

Dullemond, C. P., & Dominik, C. 2005. Dust coagulation in protoplanetary disks: A rapid depletion of small grains. *A&A*, **434**(May), 971–986.

Duschl, W. J., Strittmatter, P. A., & Biermann, P. L. 2000. A note on hydrodynamic viscosity and selfgravitation in accretion disks. *A&A*, **357**(May), 1123–1132.

Dzyurkevich, N., Flock, M., Turner, N. J., Klahr, H., & Henning, T. 2010. Trapping solids at the inner edge of the dead zone: 3-D global MHD simulations. *A&A*, **515**(June), A70+.

Eisenhauer, F., Abuter, R., Bickert, K., Biancat-Marchet, F., Bonnet, H., Brynnel, J., Conzelmann, R. D., Delabre, B., Donaldson, R., Farinato, J., Fedrigo, E., Genzel, R., Hubin, N. N., Iserlohe, C., Kasper, M. E., Kissler-Patig, M., Monnet, G. J., Roehrle, C., Schreiber, J., Stroebele, S., Tecza, M., Thatte, N. A., & Weisz, H. 2003 (Mar.). SINFONI - Integral field spectroscopy at 50 milli-arcsecond resolution with the ESO VLT. *Pages 1548–1561 of:* M. Iye & A. F. M. Moorwood (ed), *Society of Photo-Optical Instrumentation Engineers (SPIE) Conference Series*. Society of Photo-Optical Instrumentation Engineers (SPIE) Conference Series, vol. 4841.

Eisner, J. A., Hillenbrand, L. A., Carpenter, J. M., & Wolf, S. 2005. Constraining the Evolutionary Stage of Class I Protostars: Multiwavelength Observations and Modeling. *ApJ*, **635**(Dec.), 396–421.

Fallscheer, C., Beuther, H., Sauter, J., Wolf, S., & Zhang, Q. 2011. A High-mass Dusty Disk Candidate: The Case of IRAS 18151-1208. *ApJ*, **729**(Mar.), 66–+.

Gammie, C. F. 2001. Nonlinear Outcome of Gravitational Instability in Cooling, Gaseous Disks. *ApJ*, **553**(May), 174–183.

Garaud, P., & Lin, D. N. C. 2004. On the Evolution and Stability of a Protoplanetary Disk Dust Layer. *ApJ*, **608**(June), 1050–1075.

Glauser, A. M., Ménard, F., Pinte, C., Duchêne, G., Güdel, M., Monin, J.-L., & Padgett, D. L. 2008. Multiwavelength studies of the gas and dust disc of IRAS 04158+2805. *A&A*, **485**(July), 531–540.

Guilloteau, S., Dutrey, A., & Simon, M. 1999. GG Tauri: the ring world. *A&A*, **348**(Aug.), 570–578.

Guilloteau, S., Dutrey, A., Pety, J., & Gueth, F. 2008. Resolving the circumbinary dust disk surrounding HH 30. *A&A*, **478**(Feb.), L31–L34.

Gullbring, E., Hartmann, L., Briceno, C., & Calvet, N. 1998. Disk Accretion Rates for T Tauri Stars. *ApJ*, **492**(Jan.), 323–+.

Güttler, C., Krause, M., Geretshauser, R. J., Speith, R., & Blum, J. 2009. The Physics of Protoplanetesimal Dust Agglomerates. IV. Toward a Dynamical Collision Model. *ApJ*, **701**(Aug.), 130–141.

Haisch, Jr., K. E., Lada, E. A., & Lada, C. J. 2001. Disk Frequencies and Lifetimes in Young Clusters. *ApJ*, **553**(June), L153–L156.

Haniff, C. 2007. An introduction to the theory of interferometry. *New A Rev.*, **51**(Oct.), 565–575.

Ho, P. T. P., Moran, J. M., & Lo, K. Y. 2004. The Submillimeter Array. *ApJ*, **616**(Nov.), L1–L6.

Hughes, A. M., Wilner, D. J., Kamp, I., & Hogerheijde, M. R. 2008. A Resolved Molecular Gas Disk around the Nearby A Star 49 Ceti. *ApJ*, **681**(July), 626–635.

Johansen, A., Oishi, J. S., Mac Low, M.-M., Klahr, H., Henning, T., & Youdin, A. 2007. Rapid planetesimal formation in turbulent circumstellar disks. *Nature*, **448**(Aug.), 1022–1025.

Johansen, A., Youdin, A., & Klahr, H. 2009. Zonal Flows and Long-lived Axisymmetric Pressure Bumps in Magnetorotational Turbulence. *ApJ*, **697**(June), 1269–1289.

Kamp, I., & Dullemond, C. P. 2004. The Gas Temperature in the Surface Layers of Protoplanetary Disks. *ApJ*, **615**(Nov.), 991–999.

Kemper, F., Vriend, W. J., & Tielens, A. G. G. M. 2004. The Absence of Crystalline Silicates in the Diffuse Interstellar Medium. *ApJ*, **609**(July), 826–837.

Kenyon, S. J., & Hartmann, L. 1987. Spectral energy distributions of T Tauri stars - Disk flaring and limits on accretion. *ApJ*, **323**(Dec.), 714–733.

Kenyon, S. J., Whitney, B. A., Gomez, M., & Hartmann, L. 1993. The embedded young stars in the Taurus-Auriga molecular cloud. II - Models for scattered light images. *ApJ*, **414**(Sept.), 773–792.

Kessler-Silacci, J. E., Dullemond, C. P., Augereau, J.-C., Merín, B., Geers, V. C., van Dishoeck, E. F., Evans, II, N. J., Blake, G. A., & Brown, J. 2007. Probing Protoplanetary Disks with Silicate Emission: Where Is the Silicate Emission Zone? *ApJ*, **659**(Apr.), 680–684.

Klahr, H., & Brandner, W. 2006. *Planet Formation.*

Klahr, H. H., & Henning, T. 1997. Particle-Trapping Eddies in Protoplanetary Accretion Disks. *Icarus*, **128**(July), 213–229.

Klahr, H. H., & Lin, D. N. C. 2001. Dust Distribution in Gas Disks: A Model for the Ring around HR 4796A. *ApJ*, **554**(June), 1095–1109.

Kokubo, E., & Ida, S. 2002. Formation of Protoplanet Systems and Diversity of Planetary Systems. *ApJ*, **581**(Dec.), 666–680.

Kretke, K. A., & Lin, D. N. C. 2007. Grain Retention and Formation of Planetesimals near the Snow Line in MRI-driven Turbulent Protoplanetary Disks. *ApJ*, **664**(July), L55–L58.

Krumholz, M. R., Klein, R. I., McKee, C. F., Offner, S. S. R., & Cunningham, A. J. 2009. The Formation of Massive Star Systems by Accretion. *Science*, **323**(Feb.), 754–.

Lada, C. J., & Wilking, B. A. 1984. The nature of the embedded population in the Rho Ophiuchi dark cloud - Mid-infrared observations. *ApJ*, **287**(Dec.), 610–621.

Langkowski, D., Teiser, J., & Blum, J. 2008. The Physics of Protoplanetesimal Dust Agglomerates. II. Low-Velocity Collision Properties. *ApJ*, **675**(Mar.), 764–776.

Launhardt, R., & Henning, T. 1997. Millimetre dust emission from northern BOK globules. *A&A*, **326**(Oct.), 329–346.

Launhardt, R., & Sargent, A. I. 2001. A Young Protoplanetary Disk in the Bok Globule CB 26? *ApJ*, **562**(Dec.), L173–L175.

Launhardt, R., Pavlyuchenkov, Y., Gueth, F., Chen, X., Dutery, A., Guilloteau, S., Henning, T., Pietu, V., Schreyer, K., & Semenov, D. 2008. Young T Tauri star in CB 26 molecular outflows (Launhardt+, 2009). *VizieR Online Data Catalog*, **349**(Nov.), 40147–+.

Launhardt, R., Pavlyuchenkov, Y., Gueth, F., Chen, X., Dutrey, A., Guilloteau, S., Henning, T., Piétu, V., Schreyer, K., & Semenov, D. 2009. Rotating molecular outflows: the young T Tauri star in CB 26. *A&A*, **494**(Jan.), 147–156.

Lissauer, J. J. 1993. Planet formation. *ARA&A*, **31**, 129–174.

Lucas, P. W., & Roche, P. F. 1997. Butterfly star in Taurus: structures of young stellar objects. *MNRAS*, **286**(Apr.), 895–919.

Lucy, L. B. 1999. Computing radiative equilibria with Monte Carlo techniques. *A&A*, **344**(Apr.), 282–288.

Lynden-Bell, D., & Pringle, J. E. 1974. The evolution of viscous discs and the origin of the nebular variables. *MNRAS*, **168**(Sept.), 603–637.

Marseille, M., Bontemps, S., Herpin, F., van der Tak, F. F. S., & Purcell, C. R. 2008. Evolution of massive protostars: the IRAS 18151-1208 region. *A&A*, **488**(Sept.), 579–595.

Mathis, J. S., Rumpl, W., & Nordsieck, K. H. 1977. The size distribution of interstellar grains. *ApJ*, **217**(Oct.), 425–433.

McCabe, C., Duchêne, G., & Ghez, A. M. 2003. The First Detection of Spatially Resolved Mid-Infrared Scattered Light from a Protoplanetary Disk. *ApJ*, **588**(May), L113–L116.

Meeus, G., Juhász, A., Henning, T., Bouwman, J., Chen, C., Lawson, W., Apai, D., Pascucci, I., & Sicilia-Aguilar, A. 2009. MBM 12: young protoplanetary discs at high galactic latitude. *A&A*, **497**(Apr.), 379–392.

Mie, G. 1908. Beitrge zur Optik trber Medien, speziell kolloidaler Metallsungen. *Annalen der Physik*, **330**(Jan.), 377–445.

Neuhäuser, R., Krämer, S., Mugrauer, M., Köhler, R., Schmidt, T. O. B., Ammler-von Eiff, M., Alves, J., Fiedler, S., & Vogt, N. 2009. Edge-on disk around the T Tauri star [MR81] Hα 17 NE in Corona Australis. *A&A*, **496**(Mar.), 777–786.

Okuzumi, S., Tanaka, H., Takeuchi, T., & Sakagami, M.-a. 2011a. Electrostatic Barrier Against Dust Growth in Protoplanetary Disks. I. Classifying the Evolution of Size Distribution. *ApJ*, **731**(Apr.), 95–+.

Okuzumi, S., Tanaka, H., Takeuchi, T., & Sakagami, M.-a. 2011b. Electrostatic Barrier Against Dust Growth in Protoplanetary Disks. II. Measuring the Size of the "Frozen" Zone. *ApJ*, **731**(Apr.), 96–+.

Ormel, C. W., Paszun, D., Dominik, C., & Tielens, A. G. G. M. 2009. Dust coagulation and fragmentation in molecular clouds. I. How collisions between dust aggregates alter the dust size distribution. *A&A*, **502**(Aug.), 845–869.

Ossenkopf, V. 1993. Dust coagulation in dense molecular clouds: The formation of fluffy aggregates. *A&A*, **280**(Dec.), 617–646.

Ossenkopf, V., & Henning, T. 1994. Dust opacities for protostellar cores. *A&A*, **291**(Nov.), 943–959.

Padgett, D. L., Brandner, W., Stapelfeldt, K. R., Strom, S. E., Terebey, S., & Koerner, D. 1999. HUBBLE SPACE TELESCOPE/NICMOS Imaging of Disks and Envelopes around Very Young Stars. *AJ*, **117**(Mar.), 1490–1504.

Padmanabhan, P. 2000. *Theoretical astrophysics. Vol.1: Astrophysical processes.*

Pety, J. 2005 (Dec.). Successes of and Challenges to GILDAS, a State-of-the-Art Radioastronomy Toolkit. *Pages 721–+ of:* F. Casoli, T. Contini, J. M. Hameury, & L. Pagani (ed), *SF2A-2005: Semaine de l'Astrophysique Francaise.*

Pety, J., Gueth, F., Guilloteau, S., & Dutrey, A. 2006. Plateau de Bure interferometer observations of the disk and outflow of HH 30. *A&A*, **458**(Nov.), 841–854.

Pinte, C., Fouchet, L., Ménard, F., Gonzalez, J.-F., & Duchêne, G. 2007. On the stratified dust distribution of the GG Tauri circumbinary ring. *A&A*, **469**(July), 963–971.

Pinte, C., Padgett, D. L., Ménard, F., Stapelfeldt, K. R., Schneider, G., Olofsson, J., Panić, O., Augereau, J. C., Duchêne, G., Krist, J., Pontoppidan, K., Perrin, M. D., Grady, C. A., Kessler-Silacci, J., van Dishoeck, E. F., Lommen, D., Silverstone, M., Hines, D. C., Wolf, S., Blake, G. A., Henning, T., & Stecklum, B. 2008. Probing dust grain evolution in IM Lupi's circumstellar disc. Multi-wavelength observations and modelling of the dust disc. *A&A*, **489**(Oct.), 633–650.

Platon. 1991. *Πολιτεία, Der Staat.* 1st, edn. Insel Taschenbuch.

Przygodda, F., van Boekel, R., Àbrahàm, P., Melnikov, S. Y., Waters, L. B. F. M., & Leinert, C. 2003. Evidence for grain growth in T Tauri disks. *A&A*, **412**(Dec.), L43–L46.

Robitaille, T. P., Whitney, B. A., Indebetouw, R., & Wood, K. 2007. Interpreting Spectral Energy Distributions from Young Stellar Objects. II. Fitting Observed SEDs Using a Large Grid of Precomputed Models. *ApJS*, **169**(Apr.), 328–352.

Sauter, J., & Wolf, S. 2011. Observing dust settling and coagulation in circumstellar discs. Selected constraints from high resolution imaging. *A&A*, **527**(Mar.), A27+.

Sauter, J., Wolf, S., Launhardt, R., Padgett, D. L., Stapelfeldt, K. R., Pinte, C., Duchêne, G., Ménard, F., McCabe, C.-E., Pontoppidan, K., Dunham, M., Bourke, T. L., & Chen, J.-H. 2009. The circumstellar disc in the Bok globule CB 26. Multi-wavelength observations and modelling of the dust disc and envelope. *A&A*, **505**(Oct.), 1167–1182.

Schegerer, A., Wolf, S., Voshchinnikov, N. V., Przygodda, F., & Kessler-Silacci, J. E. 2006. Analysis of the dust evolution in the circumstellar disks of T Tauri stars. *A&A*, **456**(Sept.), 535–548.

Schegerer, A. A., Wolf, S., Hummel, C. A., Quanz, S. P., & Richichi, A. 2009. Tracing the potential planet-forming regions around seven pre-main-sequence stars. *A&A*, **502**(July), 367–383.

Shakura, N. I., & Sunyaev, R. A. 1973. Black holes in binary systems. Observational appearance. *A&A*, **24**, 337–355.

Shu, F. H. 1991. The Formation of Low Mass Stars: Theory. *Pages 365–+ of:* C. J. Lada & N. D. Kylafis (ed), *NATO ASIC Proc. 342: The Physics of Star Formation and Early Stellar Evolution.*

Sicilia-Aguilar, A., Bouwman, J., Juhász, A., Henning, T., Roccatagliata, V., Lawson, W. A., Acke, B., Feigelson, E. D., Tielens, A. G. G. M., Decin, L., & Meeus, G. 2009. The Long-Lived Disks in the η Chamaeleontis Cluster. *ApJ*, **701**(Aug.), 1188–1203.

Simon, M., Dutrey, A., & Guilloteau, S. 2000. Dynamical Masses of T Tauri Stars and Calibration of Pre-Main-Sequence Evolution. *ApJ*, **545**(Dec.), 1034–1043.

Sridharan, T. K., Beuther, H., Schilke, P., Menten, K. M., & Wyrowski, F. 2002. High-Mass Protostellar Candidates. I. The Sample and Initial Results. *ApJ*, **566**(Feb.), 931–944.

Stapelfeldt, K. R., Krist, J. E., Menard, F., Bouvier, J., Padgett, D. L., & Burrows, C. J. 1998. An Edge-On Circumstellar Disk in the Young Binary System HK Tauri. *ApJ*, **502**(July), L65+.

Stapelfeldt, K. R., Ménard, F., Watson, A. M., Krist, J. E., Dougados, C., Padgett, D. L., & Brandner, W. 2003. Hubble Space Telescope WFPC2 Imaging of the Disk and Jet of HV Tauri C. *ApJ*, **589**(May), 410–418.

Stecklum, B., Launhardt, R., Fischer, O., Henden, A., Leinert, C., & Meusinger, H. 2004. High-Resolution Near-Infrared Observations of the Circumstellar Disk System in the Bok Globule CB 26. *ApJ*, **617**(Dec.), 418–424.

Strom, K. M., Strom, S. E., Edwards, S., Cabrit, S., & Skrutskie, M. F. 1989. Circumstellar material associated with solar-type pre-main-sequence stars - A possible constraint on the timescale for planet building. *AJ*, **97**(May), 1451–1470.

Thamm, E., Steinacker, J., & Henning, T. 1994. Ambiguities of parametrized dust disk models for young stellar objects. *A&A*, **287**(July), 493–502.

Toomre, A. 1964. On the gravitational stability of a disk of stars. *ApJ*, **139**(May), 1217–1238.

Ulrich, R. K. 1976. An infall model for the T Tauri phenomenon. *ApJ*, **210**(Dec.), 377–391.

Voshchinnikov, N. V. 2002. In the Kitchen of Dust Modeling. *Pages 1–+ of:* G. Videen & M. Kocifaj (ed), *Optics of Cosmic Dust.*

Voshchinnikov, N. V., Videen, G., & Henning, T. 2007. Effective medium theories for irregular fluffy structures: aggregation of small particles. *Appl. Opt.*, **46**(July), 4065–4072.

Wada, K., Tanaka, H., Suyama, T., Kimura, H., & Yamamoto, T. 2007. Numerical Simulation of Dust Aggregate Collisions. I. Compression and Disruption of Two-Dimensional Aggregates. *ApJ*, **661**(May), 320–333.

Wada, K., Tanaka, H., Suyama, T., Kimura, H., & Yamamoto, T. 2008. Numerical Simulation of Dust Aggregate Collisions. II. Compression and Disruption of Three-Dimensional Aggregates in Head-on Collisions. *ApJ*, **677**(Apr.), 1296–1308.

Watson, A. M., & Stapelfeldt, K. R. 2004. The Visible and Near-Infrared Dust Opacity Law in the HH 30 Circumstellar Disk. *ApJ*, **602**(Feb.), 860–874.

Watson, A. M., Stapelfeldt, K. R., Wood, K., & Ménard, F. 2007. Multiwavelength Imaging of Young Stellar Object Disks: Toward an Understanding of Disk Structure and Dust Evolution. *Protostars and Planets V*, 523–538.

Weidenschilling, S. J., & Cuzzi, J. N. 1993. Formation of planetesimals in the solar nebula. *Pages 1031–1060 of:* E. H. Levy & J. I. Lunine (ed), *Protostars and Planets III.*

Weidenschilling, S. J., & Ruzmaikina, T. V. 1994. Coagulation of grains in static and collapsing protostellar clouds. *ApJ*, **430**(Aug.), 713–726.

Weidling, R., Güttler, C., Blum, J., & Brauer, F. 2009. The Physics of Protoplanetesimal Dust Agglomerates. III. Compaction in Multiple Collisions. *ApJ*, **696**(May), 2036–2043.

Weingartner, J. C., & Draine, B. T. 2001. Dust Grain-Size Distributions and Extinction in the Milky Way, Large Magellanic Cloud, and Small Magellanic Cloud. *ApJ*, **548**(Feb.), 296–309.

Weizsäcker, C. F. V. 1948. Die Rotation kosmischer Gasmassen. *Zeitschrift Naturforschung Teil A*, **3**, 524–+.

Whitney, B. A., Wood, K., Bjorkman, J. E., & Wolff, M. J. 2003. Two-dimensional Radiative Transfer in Protostellar Envelopes. I. Effects of Geometry on Class I Sources. *ApJ*, **591**(July), 1049–1063.

Wilking, B. A., Lebofsky, M. J., Kemp, J. C., Martin, P. G., & Rieke, G. H. 1980. The wavelength dependence of interstellar linear polarization. *ApJ*, **235**(Feb.), 905–910.

Williams, J. P., & Cieza, L. A. 2011. Protoplanetary Disks and Their Evolution. *ArXiv e-prints*, Mar.

Witt, A. N., Smith, R. K., & Dwek, E. 2001. X-Ray Halos and Large Grains in the Diffuse Interstellar Medium. *ApJ*, **550**(Apr.), L201–L205.

Wolf, S. 2003a. Efficient Radiative Transfer in Dust Grain Mixtures. *ApJ*, **582**(Jan.), 859–868.

Wolf, S. 2003b. MC3D-3D continuum radiative transfer, Version 2. *Computer Physics Communications*, **150**(Feb.), 99–115.

Wolf, S., Henning, T., & Stecklum, B. 1999. Multidimensional self-consistent radiative transfer simulations based on the Monte-Carlo method. *A&A*, **349**(Sept.), 839–850.

Wolf, S., Padgett, D. L., & Stapelfeldt, K. R. 2003. The Circumstellar Disk of the Butterfly Star in Taurus. *ApJ*, **588**(May), 373–386.

Wolf, S., Schegerer, A., Beuther, H., Padgett, D. L., & Stapelfeldt, K. R. 2008a. Submillimeter Structure of the Disk of the Butterfly Star. *ApJ*, **674**(Feb.), L101–L104.

Wolf, S., Schegerer, A., Beuther, H., Padgett, D. L., & Stapelfeldt, K. R. 2008b. Submillimeter Structure of the Disk of the Butterfly Star. *ApJ*, **674**(Feb.), L101–L104.

Wood, K., Wolff, M. J., Bjorkman, J. E., & Whitney, B. 2002. The Spectral Energy Distribution of HH 30 IRS: Constraining the Circumstellar Dust Size Distribution. *ApJ*, **564**(Jan.), 887–895.

Youdin, A. N., & Shu, F. H. 2002. Planetesimal Formation by Gravitational Instability. *ApJ*, **580**(Nov.), 494–505.

Zsom, A., Ormel, C. W., Güttler, C., Blum, J., & Dullemond, C. P. 2010. The outcome of protoplanetary dust growth: pebbles, boulders, or planetesimals? II. Introducing the bouncing barrier. *A&A*, **513**(Apr.), A57+.

Acknowledgements

To complete this thesis, I had the support and help of a large number of great people. I would especially like to thank …

… *Sebastian Wolf* for supervising this thesis, for widening my horizon in many aspects, for his patience and equanimity, and for positively teaching me how to swim in cold water.

… *Kees Dullemond* for co-supervising this thesis, for positively questioning my scientific reasoning, for spending a holiday on the blackboard, and for teaching me that also modesty is not always a virtue.

… *Cassie Fallscheer* for the productive work on IRAS 18151-1208, for language editing even though she wouldn't allow me to use 'shingly', and for teaching me that sometimes the most important thing about mathematics is a slide.

… *Til Birnstiel* for providing and discussing his dust trapping models, for letting me hitch-hike up and down to the Königstuhl and for teaching me all sorts of tricks on a Mac.

… *Henrik Beuther and Ralf Launhardt* for their all-time readiness to answer my mostly interferometry related questions, not seldom in connection with a ride up or down the mountain.

… *the members of the GEODE-Team* for their intensive and constructive discussion of the CB 26 model.

… *Anne Dutrey & Stephane Guilloteau* for their support in dealing with proposals, IRAM, and the Butterfly star.

… *Arjan Bik & Tobias Illenseer*, my office mates in Heidelberg and Kiel, for their cheerful attitude, their willingness to share their astronomical, post-doctoral wisdom with me, and for teaching me that there is always time for a (scientific) discussion and coffee.

... *my colleagues at the MPIA & ITAP*, for their nurturing of the friendly, welcoming, and accommodating environment in both Institutes.

... *the people in the MPIA & ITAP IT and administrative departments* for the tremendously fast and helpful attitude towards my computational and bureaucratical needs and whims.

This thesis was made possible by funding through the DFG Forschergruppe 759 “The Formation of Planets: The Critical First Growth Phase” and by a MPIA stipend.

The final words of this thesis do not belong to science but to my family. It is them who I owe the utmost thanks for their deep love and warmth, for their evidently inexhaustible support towards me, despite some hardships in the course of this thesis.

Thank you.

Erklärung

Hiermit erkläre ich, daß

1. die Arbeit, abgesehen von Beratung durch den Betreuer Prof. Dr. S. Wolf, in Inhalt und Form die eigene Arbeit ist,
2. die Arbeit keiner anderen Stelle im Rahmen eines Prüfungsverfahrens vorgelegen hat oder vorliegt,
3. Teile der Arbeit veröffentlicht worden sind: Sauter *et al.* (2009); Sauter & Wolf (2011); Fallscheer *et al.* (2011) und
4. die Arbeit unter Einhaltung der Regeln guter wissenschaftlicher Praxis der Deutschen Forschungsgemeinschaft entstanden ist.

[Jürgen Sauter]